From upper limits to detection: Continuous gravitational waves in the advanced detector era

Erin Patricia Macdonald

B.A., Physics with Astrophysics

B.A., Mathematics

Submitted in fulfilment of the requirements for the Degree of Doctor of Philosophy

Institute for Gravitational Research

School of Physics and Astronomy

College of Science and Engineering

University of Glasgow

July 2012

For The Burger

Abstract

This thesis concerns continuous gravitational wave signals from non-axisymmetric neutron stars and ground-based interferometric detectors. These detectors are currently being upgraded and this thesis explores relevant issues and methods to prepare for the advanced detector era. A study into sensitivity dependence on the addition of a southern hemisphere detector for a targeted continuous wave search is first presented. Next, we study the effect of close and/or high velocity neutron stars on the ability of a blind, all-sky search to make a detection. Initial results from a narrow-band search for signals from the Crab Pulsar and a blind hardware injected signal are then presented. Finally, we describe the development and initial implementation of a large-scale mock data challenge designed to test current continuous wave algorithms to explore various issues before we enter the advanced detector era.

Declaration

I, Erin Patricia Macdonald, confirm that the work presented in this thesis is my own. Where information has been derived from other sources, I confirm that this has been indicated in the thesis.

Chapters 1 and 2 discuss the background of gravitational waves with derivation of equations and a summary of the history. The appropriate citations are given where relevant in the discussion.

Chapter 3 presents work which is my own with the background information appropriately cited. The parameter space discussed in Section 3.1 were the results of discussions with Matthew Pitkin and Graham Woan. The simulation code utilised a Markov Chain Monte Carlo written by Matthew Pitkin. The simulation code was written by myself in Matlab and reviewed by Matthew Pitkin. The plots and analysis are entirely my own.

The work presented in Chapter 4 is entirely my own and uses the technical computing software Mathematica. It is the result of review and discussions with my supervisor, Graham Woan. I also used data from the Australia Telescope National Facility for an understanding of known pulsar populations.

Chapter 5 presents results from a "narrow-band" search for gravitational waves. Section 5.1 and 5.2 are a review of the statistics and the search and is properly referenced. Section 5.3 is entirely my own work and the results from Section 5.4 were achieved with the assistance of Joseph Betzweiser as he was teaching me the

search code.

The code and the plots given in Chapter 6 were developed by me through discussion with the entire Continuous Wave working group in the LIGO/Virgo Scientific Collaboration. Reinhard Prix assisted me with debugging the injection code and Carsten Aulbert helped me with code management and submission on the Atlas Computing Cluster.

Chapter 7 presents initial results from the mock data challenge. I developed the requirements for the challenge and the data in Section 7.1.1 was processed by Vladimir Dergachev using his PowerFlux analysis code. The data from Section 7.1.2 was processed by Colin Gill using the Bayesian time-domain search. The analysis of results and the discussion is mine.

The conclusion in Chapter 8 is my own analysis of the work and results in this thesis. Again, where necessary work has been properly cited.

Erin P. Macdonald

July 2012

Acknowledgements

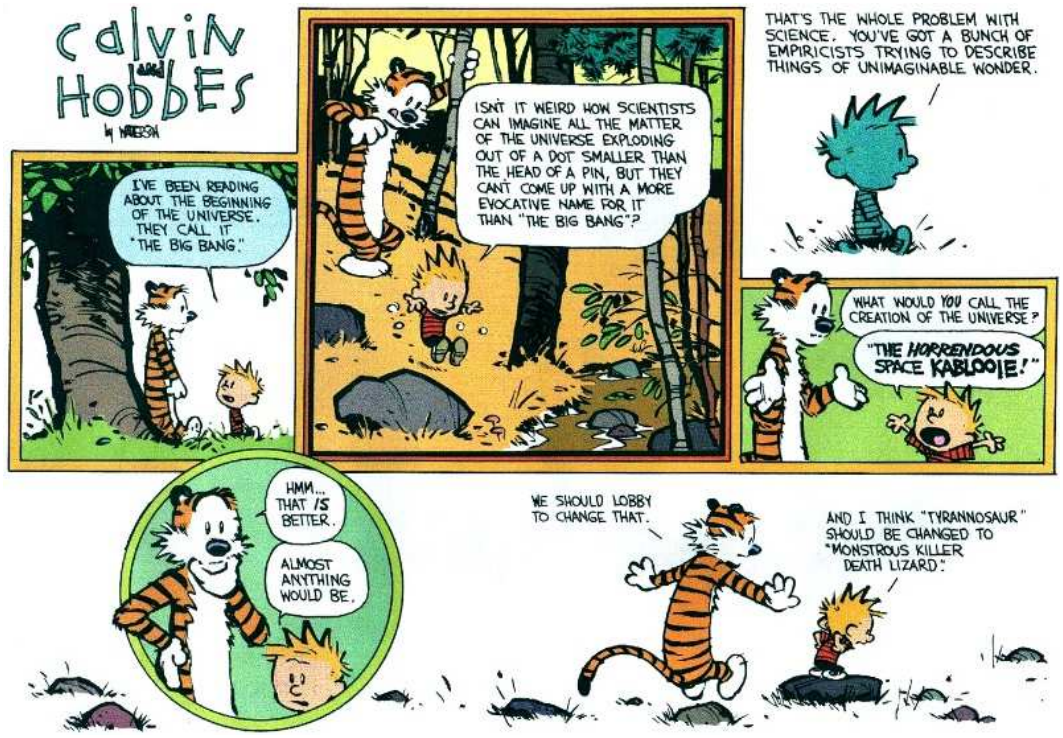

There are many people who deserve acknowledgment and thanks for helping me through my PhD. I would not have been successful in this PhD without the guidance and support of my supervisor, Graham Woan who supported me every step of the way. I would like to give a really special acknowledgment to Matthew Pitkin, my friend, office-mate and travel buddy. I appreciate the fact that he was always there for me when I had even the most basic questions.

I also must acknowledge the help of Reinhard Prix who taught me how to properly code, converted me to the usage of C and who didn't laugh too hard when I called

him panicked that I had broken all the computers. Additionally, Carsten Aulbert was unfailingly available any time day or night to help me run and manage my codes and seemed not to mind having to guide me step-by-step through the world of Condor and computing clusters. I could not have done all of this without either of their help. A special thanks to Jim Hough and Sheila Rowan for providing me with continuing support and making my life in Scotland much easier.

Additionally, there are many people in my personal life I would like to thank for their support and good times.

First, and most especially, to my husband, The Burger (David) for always making me laugh when I need it most, for always making me feel loved for who I am and for supporting me in the best and worst of times.

To Nicola Beveridge for all the afternoons in Tennents and Kember and Jones, for mutual support when we would ditch the gym in favour of wine, for the fangirl discussions ranging from the West Wing to Star Trek: Voyager and especially for giving my phone number to The Burger.

To Morag Casey and Marina Battaglia, for all the "girl's nights", the coffee breaks, chats, rants, gossip and support, but NOT for that 5k. To Marina especially for going through homesickness with me and finding the cure in the bottom of a bottle of wine, Mr India's takeaway and a night with McCoy and Spock.

To Deno Stelter, for being one of my best friends no matter what the distance and I cannot wait to geek out with him and his fantastic new wife, Tahlia DeMaio, at many more Dragon*Cons. So say we all.

To the staff at Curlers Rest, for all the chats, laughs, pints and bottles of Long Shadow Shiraz.

To my mum, Anne, for constant, daily, entertaining emails about new television shows and political gossip.

To my dad, Bruce, for his undying enthusiasm, scientific discussions, support and for inspiring me to go for this degree. Sorry about the tattoos, Dad.

To my brother, James, for the instant messenger chats when I need to procrastinate.

To Drew Gaede, for being a sister and for understanding me.

To Flogging Molly, for teaching me that all my strife in moving overseas alone was not unique and for holding my hand when I needed it the most.

To Eluveitie, Nightwish and Korpiklaani for providing the soundtrack to my thesis-writing days.

Finally, to Captain Kathryn Janeway. I cannot describe the level of inspiration she provided me right when I was on the verge of giving up.

May the Force be with you,

Live Long and Prosper,

So say we all.

Contents

List of Figures

List of Tables

1

Gravitational waves: theory, astrophysical sources and detectors

This thesis presents a detailed analysis of techniques for gravitational wave signal detection from isolated, non-axisymmetric neutron stars and describes new tools and strategies relevant to their future development. The gravitational wave community is preparing to enter the "Advanced Detector" era where detector networks will be sufficiently sensitive that a direct gravitational wave detection is likely. These detections could come from a variety of astrophysical sources, for which the various groups in the gravitational wave community have been developing detection techniques. There are many search algorithms already in place for the LIGO and Virgo Scientific Collaboration,[1] and in the coming years these need to be comprehensively tested in preparation for the advanced detector data. One of the analysis groups is the continuous wave (CW) working group, which focuses on long-duration signals from neutron stars. The CW group has developed various search methods, from targeted searches to all-sky "blind" searches. This group has already placed upper limits

[1] `http://www.ligo.org/`

on gravitational wave amplitudes from known sources such as the Crab Pulsar [10] and recently the Vela Pulsar [2] using data from the previous generation of gravitational wave detectors. The group has also successfully recovered hardware-injected signals.

This thesis presents the development of a large-scale mock data set for the purpose of testing various CW algorithm's performance. An initial "mock data challenge" is presented along with initial results from two established CW searches.

In addition, data from the recent LIGO science run (S6) is analysed using a directed narrow-band algorithm to search for the Crab pulsar as well as a hardware injected CW signal. This thesis also investigates the effect that proper motion and parallax has on the all-sky searches, specifically Einstein@Home. [2] These investigations are all important to consider for CW searches in the Advanced Detector era where detections are likely. We want to ensure that we have optimised our techniques and understand possible pitfalls as carefully as possible before this era. This thesis discusses various considerations and presents methods for signal analysis.

1.1 Gravitational wave theory

Gravitational waves are a direct implication of Albert Einstein's Theory of General Relativity [36]. In loose terms, general relativity describes the Universe as a 4-dimensional space-time manifold, where the presence of mass causes a curvature. The more massive an object, the more extreme the curvature, and the motion of massive objects in the Universe causes a "ripple" in this space-time manifold. This ripple is a wave sending information about the motion, which travels at the speed of light [36]. Einstein's discovery that gravitational force and fields moved at the speed of light was revolutionary as it contradicted previous understanding that gravita-

[2] `http://einstein.phys.uwm.edu/`

tional force was felt instantaneously.[3]

Gravitational radiation can be described as fluctuations in a Minkowski (flat) space-time metric. An interval in such a metric obeys

$$\mathrm{d}s^2 = \eta_{\mu\nu}\ \mathrm{d}x^\mu\ \mathrm{d}x^\nu \tag{1.1}$$

where $\mathrm{d}s$ is the interval in space-time and $\mathrm{d}x^i$ are the corresponding differential changes in space-time coordinates: time, t, and three spatial dimensions, x, y and z. The coefficient $\eta_{\mu\nu}$ which represents the Minkowski metric is defined as

$$\eta_{\mu\nu} = \begin{pmatrix} -c^2 & 0 & 0 & 0 \\ 0 & 1 & 0 & 0 \\ 0 & 0 & 1 & 0 \\ 0 & 0 & 0 & 1 \end{pmatrix} \tag{1.2}$$

where c is the speed of light [60].

For a weak gravitational field, including weak gravitational wave fluctuations, perturbations may be added to the Minkowski metric to make

$$g_{\mu\nu} = \eta_{\mu\nu} + h_{\mu\nu}; \quad |h_{\mu\nu}| << 1 \tag{1.3}$$

where $g_{\mu\nu}$ describes the full gravitational field and $h_{\mu\nu}$ is a small perturbation on that field.

The fundamental equations of general relativity are the Einstein field equations, given as

$$R_{\mu\nu} - \frac{1}{2} g_{\mu\nu} R = \frac{8\pi G}{c^4} T_{\mu\nu}, \tag{1.4}$$

where $R_{\mu\nu}$ is called the *Ricci tensor* with its trace R, referred to as the *Ricci scalar*

[3]There was good evidence that gravity indeed propagated instantaneously, for example Laplace, 1809 [53].

and $T_{\mu\nu}$ is the *Energy-momentum tensor*. If the condition $|h_{\mu\nu}| \ll 1$ from Equation 1.3 is satisfied, then it is possible to linearize the Einstein field equations with respect to the small perturbation $h_{\mu\nu}$.

To initially solve for $h_{\mu\nu}$ as gravitational waves, it is simplest to study solutions in a vacuum and harmonic coordinates as considered in Misner, Thorne and Wheeler [61]. For a vacuum, the energy-momentum tensor disappears, $T_{\mu\nu} = 0$ and the solution for harmonic coordinates reduces to

$$\Box \bar{h}_{\mu\nu} = 0. \tag{1.5}$$

The d'Alembertian operator, $\Box$, in Minkowski space-time is defined as

$$\Box \equiv \eta^{\mu\nu}\partial_\mu\partial_\nu = -\frac{1}{c^2}\partial_t^2 + \partial_x^2 + \partial_y^2 + \partial_z^2 \tag{1.6}$$

and the new quantity, $\bar{h}_{\mu\nu}$ is

$$\bar{h}_{\mu\nu} \equiv h_{\mu\nu} - \frac{1}{2}\eta_{\mu\nu}h \tag{1.7}$$

where h is the trace of $h_{\mu\nu}$.

The time-dependent solutions of these equations are interpreted as *weak* gravitational waves propagating through a flat space-time region. The simplest solution for this is a *monochromatic plane wave* of the form

$$\bar{h}_{\mu\nu}(x^\alpha) = A_{\mu\nu}\cos(k_\alpha x^\alpha - \alpha_{(\mu)(\nu)}). \tag{1.8}$$

Here, $A_{\mu\nu}$ and $\alpha_{(\mu)(\nu)}$ are the constant amplitude and constant initial phase, respectively, of the $\mu\nu$ components of the wave and k_α are real constants. For the initial phase, the indices μ and ν are bracketed to indicate there is no summation over

these indices. The Equations 1.8 are solutions of Equation 1.5 if and only if

$$\eta^{\alpha\beta}k_\alpha k_\beta = 0 \tag{1.9}$$

so we must define $k^\alpha \equiv \eta^{\alpha\beta}k_\beta$ and k^α are the components of a null 4-vector with respect to the Minkowski metric. Then the contraction of $k_\alpha x^\alpha$ can be written as

$$k_\alpha x^\alpha = -c\,k^0\,t + \mathbf{k}\cdot\mathbf{x} \tag{1.10}$$

where two 3-vectors, $\mathbf{k}$ and $\mathbf{x}$ have been introduced. with components (k^1, k^2, k^3) and (x^1, x^2, x^3) respectively. If the quantity ω is introduced as $\omega \equiv c\,k^0$, then (1.8) becomes

$$\bar{h}_{\mu\nu}(t, \mathbf{x}) = A_{\mu\nu}\cos(\omega t - \mathbf{k}\cdot\mathbf{x} + \alpha_{(\mu)(\nu)}). \tag{1.11}$$

Without loss of generality, it can be assumed that $\omega \geq 0$ and ω can be thought of as the angular frequency of the wave. The frequency, f, can also be used with the relation

$$\omega = 2\pi f. \tag{1.12}$$

The vector $\mathbf{k}$ is the wave vector and defines both the direction in which the wave is travelling and the wavelength, λ by the relation

$$\lambda|\mathbf{k}| = 2\pi. \tag{1.13}$$

Equation 1.9 can then be written in terms of ω and $\mathbf{k}$ and take the form

$$\omega = c|\mathbf{k}| \tag{1.14}$$

which is the *dispersion relation* for perturbutive gravitational waves. This implies that the phase and group velocity of the waves are equal to c, the speed of light. This result shows that in a flat vacuum, gravitational waves travel at the speed of

light.

To further reduce the gravitational wave equations a transformation may be performed into the *transverse traceless* (TT) coordinate system [47]. Introducing a time-like unit vector U^μ where $g_{\mu\nu}U^\mu U^\nu = -1$ a gauge transformation may be performed such that

$$\bar{h}'_{\mu\nu}U'^{\nu} = 0, \tag{1.15a}$$

$$\eta^{\mu\nu}\bar{h}'_{\mu\nu} = 0, \tag{1.15b}$$

$$\bar{h}'_{\mu\nu}k'^{\nu} = 0, \tag{1.15c}$$

where Equations 1.15 define the TT coordinate system. It is also important to note that as a consequence of Equation 1.15b,

$$\bar{h}'_{\mu\nu} = h'_{\mu\nu}. \tag{1.16}$$

Equations 1.15 give eight independent constraints on $\bar{h}'_{\mu\nu}$, so any plane monochromatic wave has two independent degrees of freedom, which are referred to as the gravitational wave's polarisations.

These polarisations may be better described if further coordinate changes are performed with global Lorentz transformations. By starting with the components $U^\mu = (1, 0, 0, 0)$ then by Equation 1.15a

$$\bar{h}_{\mu 0} = 0. \tag{1.17}$$

If one assumes the wave propagates in i.e., the $+z$ direction then $\mathbf{k} = (0, 0, \omega/c)$, $k^\mu = (\omega/c, 0, 0, \omega/c)$. Combining this with Equations 1.15c and 1.17 gives

$$\bar{h}_{\mu 3} = 0. \tag{1.18}$$

Finally, Equation 1.15b combines with Equations 1.17 and 1.18 to give the final constraints on $\bar{h}_{\mu\nu}$,

$$\bar{h}_{11} + \bar{h}_{22} = 0, \tag{1.19}$$

with the following notation commonly used:

$$h_+ \equiv \bar{h}_{11} = -\bar{h}_{22}, \quad h_\times \equiv \bar{h}_{12} = \bar{h}_{21}. \tag{1.20}$$

The h_+ and $h_\times$ polarisations are frequently referred to as the "plus" and "cross" polarisations, respectively, of the wave.

Equations 1.17 - 1.19 allow us to rewrite the plane-wave solution 1.11 in matrix form:

$$h^{TT}_{\mu\nu}(t, \mathbf{x}) = \begin{pmatrix} 0 & 0 & 0 & 0 \\ 0 & h_+(t, \mathbf{x}) & h_\times(t, \mathbf{x}) & 0 \\ 0 & h_\times(t, \mathbf{x}) & -h_+(t, \mathbf{x}) & 0 \\ 0 & 0 & 0 & 0 \end{pmatrix}, \tag{1.21}$$

where the polarisations h_+ and $h_\times$ of the plane wave with angular frequency ω travelling in the $+z$ direction are given by

$$h_+(t, \mathbf{x}) = A_+ \cos\left[w\left(t - \frac{z}{c}\right) + \alpha_+\right], \tag{1.22}$$

$$h_\times(t, \mathbf{x}) = A_\times \cos\left[w\left(t - \frac{z}{c}\right) + \alpha_\times\right] \tag{1.23}$$

where A_+ and $A_\times$ are the corresponding amplitudes of the two polarisations [61].

The polarization tensors e^+ and $e^\times$ are introduced as

$$e^+_{xx} = -e^+_{yy} = 1, \quad e^\times_{xy} = e^\times_{yx} = 1, \quad \text{all other components zero}, \tag{1.24}$$

then the full gravitational wave field may be constructed from the plus and cross

polarisations given the equation

$$h^{TT}_{\mu\nu}(t, \mathbf{x}) = h_{+}(t, \mathbf{x})e^{+}_{\mu\nu} + h_{\times}(t, \mathbf{x})e^{\times}_{\mu\nu}. \tag{1.25}$$

When the gravitational wave is detected (from methods discussed in Section 1.2), the amplitude of the signal contains the polarisations and the effects from detector orientation with respect to the source of the gravitational wave signal. According to [49],

$$h(t) = F_{+}(t)h_{+}(t) + F_{\times}(t)h_{\times}(t), \tag{1.26}$$

where F_{+} and $F_{\times}$ are the beam pattern functions which are periodic functions of time, with a period of one sidereal day (the rotation of the Earth) [47]. This will be explained further for the purpose of continuous waves analysis in Section 2.4.

1.2 Gravitational wave detectors and current limitations

Joseph Weber attempted the first direct detection of gravitational waves in the 1960s using resonating aluminum bars, referred to as "Weber bars" [82] and [83]. These bars resonate at approximately 1600 Hz, a frequency where the radiation from collapsing stars was expected to peak. Though there were coincident detections of Weber's bars, these were not also seen in similar experiments around the world. Another reason to disregard Weber's supposed detections is that Weber's bar detector was sensitive to strains of order 10^{-16}, insufficient to detect the theoretically predicted signals. Bar detectors are still being used, with cooling techniques developed to reduce the noise, but these efforts are subsiding [65].

Currently, the use of ground-based laser interferometers dominates the field, and in 2003 they surpassed the peak sensitivity of the bar detectors [65]. These interfer-

ometers are sensitive to a wide band of frequencies, so they can be used to detect gravitational waves from various sources, as discussed in Section 1.3. The arm configuration of interferometers is also ideal for detection due to the quadrupolar nature of gravitational waves.

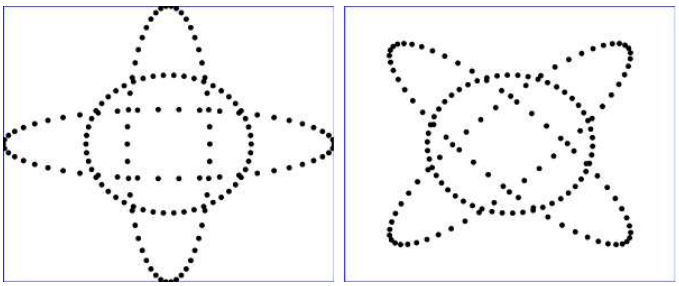

Figure 1.1 – A ring of particles reacting to plus and cross polarisations (left and right, respectively) of gravitational waves. Image courtesy of Sathyaprakash and Schutz, 2009 [74].

The LIGO Scientific Collaboration currently is operating three interferometric detectors: two in Hanford, WA and one in Livingston, LA. The Livingston detector and one of the Hanford detectors have arm lengths of 4 km and are referred to as L1 and H1, respectively. The Hanford detector is shown in Figure 1.2. The other Hanford detector has arm lengths of 2 km and is referred to as H2 [40]. Other detectors are the GEO600 detector in Germany, Virgo in Italy and TAMA300 in Japan. This thesis will mostly refer to data from the LIGO detectors.

An interferometric detector operates by sending a laser beam through a beamsplitter and onto two test masses which are suspended with pendulum systems at the ends of (ideally orthogonal) arms. The light is reflected from the mirrors on the test masses back to recombine at a photo-diode as seen in Figure 1.3.

The quadrupolar nature of the gravitational wave will cause the arm lengths to compress and stretch, resulting in a change of intensity of light at the photo-diode [65]. If a suitably oriented gravitational wave is incident upon this interferometer then the arm lengths will change with respect to each other and the combined laser beam will show an interference pattern making these detectors ideal for detecting

Figure 1.2 – Aerial view of the Hanford interferometer. Photo credit: LIGO Laboratory.

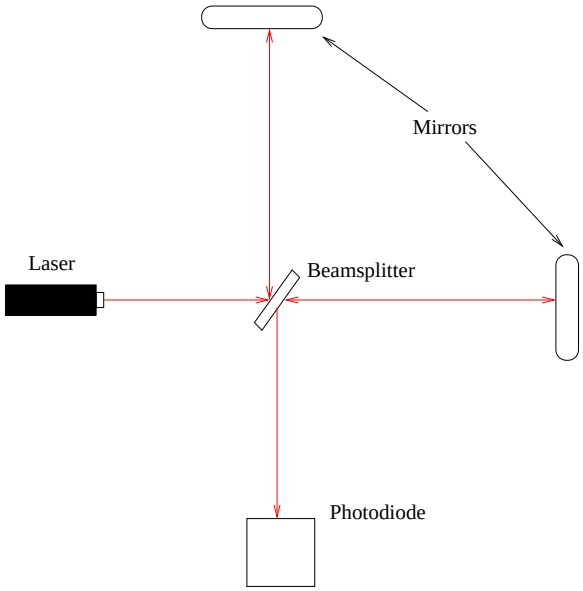

Figure 1.3 – Simple schematic of a Michelson interferometer used for gravitational wave detection.

the quadrupolar nature of gravitational waves. The detection of these waves comes from the change in arm length ΔL due to the gravitational wave amplitude, h,

$$h = \frac{2\Delta L}{L}, \tag{1.27}$$

where L is the arm length of the interferometers. The challenge of gravitational wave detections is that even for the most violent astrophysical events, the amplitude is extremely small, approximately 10^{-21} or less [74].

The frequencies at which the current, operating LIGO detectors are sensitive range from about 10 Hz to about 6 kHz and the initial runs achieved a strain noise floor of nearly $2 \times 10^{-23}\,\mathrm{Hz}^{-1/2}$. The advanced detectors will push this floor down another factor of 10-15 [66]. The sensitivities for the initial runs of the LIGO detectors is seen in Figure 1.4.

The sensitivity of the detectors is limited by various sources of noise which combine across the frequency spectrum. Detectors currently in operation have been able to overcome these various sources of noise to allow unprecedented sensitivity. Seismic noise originates from motion on the surface of the Earth and fluctuations below ground. Seismic noise primarily affects the low-frequency band, below about 50 Hz due to the fact that vibration isolation systems fall towards the lower frequencies. Thermal noise is due to Brownian motion in the optics and suspensions and dominates (due to losses in the suspensions) from 50 to 150 Hz. Shot noise in a free laser beam is frequency independent, but storage time effects in the arm cavities cause the shot noise background to measured strain to rise as f above a cavity pole at 90 Hz, dominating the background strain spectrum above 150 Hz [67]. These sources of noise all contribute to the total noise curve shape as seen in Figure 1.4.

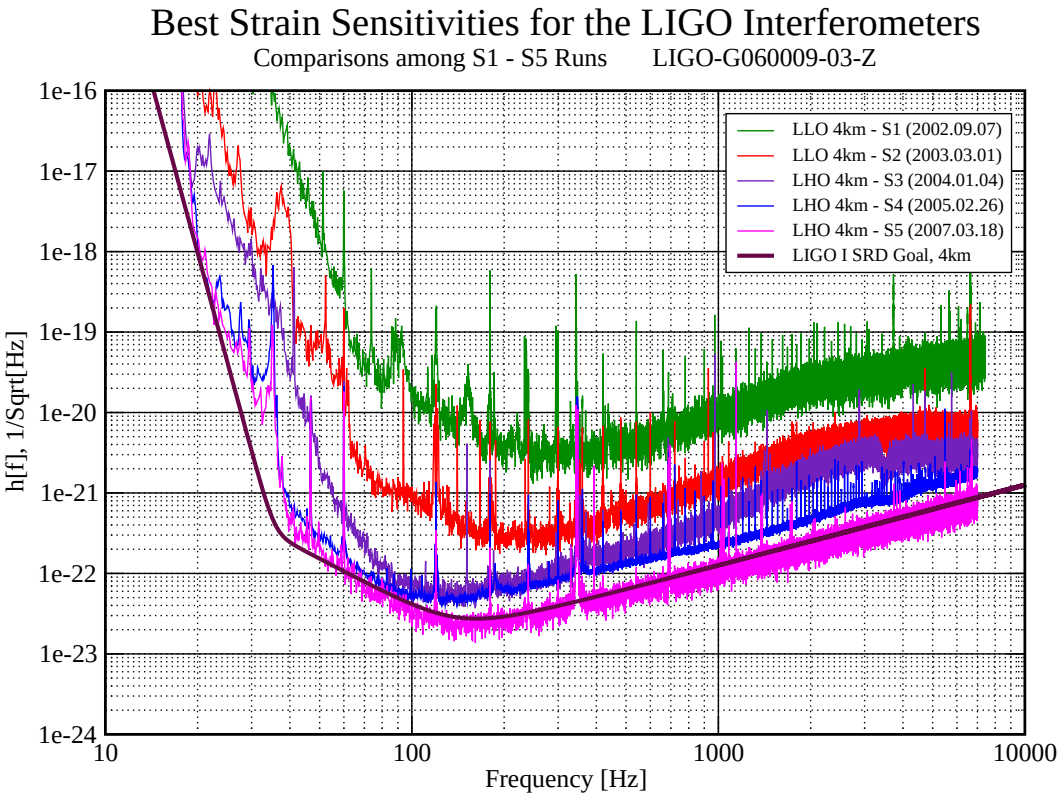

Figure 1.4 – Sensitivity curves for the initial 5 science runs (S1-S5) of the 4 km Hanford detector (LHO) and the Livingston detector (LLO). The black line shows the sensitivity goal for the initial runs which is calculated from the noise sources mentioned in this section. The final science run (S5) was able to eliminate other technical noise and achieve the goal sensitivity curve. Image courtesy of the LIGO Laboratory [63].

1.2.1 Low-frequency limitations from seismic noise

Seismic noise, which is due to the motion of the Earth, acts with an effect of approximately $10^{-7}\ f^{-2}$ m/Hz$^{1/2}$ (for a reasonably quiet location) in the six degrees of freedom (three displacement and three rotation motions) [67]. For our detectors, the test masses should be disturbed less than 3×10^{-20} m/Hz$^{1/2}$. This means that, say around 30 Hz, the seismic noise must be reduced in the horizontal direction more than 10^9. The horizontal and vertical seismic noise are coupled to one another due to the curvature of the Earth and thus must be isolated in both directions to fully reduce the effects. The methods used in the interferometers to reduce seismic noise includes suspension systems with springs which effectively isolates the mirrors in all six dimensions [23], [51], [32].

For Advanced LIGO, the plan is to incorporate an external stage of hydraulic isolation, two in-vacuum stages of active isolation as well as the mass suspension [40], [15]. Active damping of the pendulum modes is required as motion will occur at the excitement of pendulum frequencies [67].

1.2.2 Thermal effects on the noise floor

Thermal noise is the next most significant source of noise for the gravitational wave interferometer detectors at the low frequency end of the operating range. From [75] it can be shown that for any simple harmonic oscillator such as a test mass on a spring or pendulum, the spectral density of the thermal motion of the mass is

$$x^2(\omega) = \frac{4k_B T\omega_0^2\phi(\omega)}{\omega m[(\omega_0^2-\omega^2)^2+\omega_0^4\phi^2(\omega)]}, \tag{1.28}$$

where k_B is Boltzmann's constant, T is the temperature, m is the mass and $\phi(\omega)$ is the loss angle of the oscillator which has an angular resonant frequency ω_0. For a mass on a spring, the loss angle (factor) comes from the material properties of the spring. However, for a pendulum most of the energy is stored in the lossless gravitational field which means the loss factor is lower than the loss factor of the material used for the wires or fibres suspending the pendulum [67]. Following [75], it can be shown that a pendulum of mass m suspended on four fibres of length l, the loss factor of the pendulum is related to the loss factor of the material by

$$\phi_{\text{pend}}(\omega) = \phi_{\text{mat}}(\omega)\frac{4\sqrt{TEI}}{mgl}, \tag{1.29}$$

where I is the moment of the cross-section of the fibre and T is the tension in the wire whose material has a Young's modulus E [67].

Most material's loss factors are independent of the frequencies of interest in gravitational wave detectors. By assuming the resonant mode of the test mass is a harmonic

oscillator, the internal thermal noise may be estimated [67]. It is important to keep the thermal noise effects as low as possible. This is achieved by making sure the mass's mechanical loss factors and the resonant frequencies are as as low as possible. The shape of the the masses and the size of the masses are important to keep internal resonances and possible losses maximally reduced.

1.2.3 Newtonian noise from surface density gradients

Newtonian noise arises from fluctuations in the gravitational field around the Earth. This could be due to a number of factors, such as density fluctuations (in time) of the Earth's surface [67]. To completely eliminate this effect on detectors, the detectors must be in space, as some future proposed missions will be. There are two main solutions to reduce this effect for ground-based detectors.

The first solution is to monitor local density gradients by placing seismometers in the area around the detector. The motion can be observed and their calculated effects can be subtracted from the detector output after the fact [67]. The second solution is to build the detectors in a very quiet location or underground as most of the gravitational field effects comes from surface density fluctuations. This is currently being proposed for the LCGT detector in Japan [62], as well as the Einstein Telescope [72].

1.2.4 Quantum effects at high and low frequencies

Shot noise at high frequency

Shot noise dominates above 300 Hz in the gravitational wave detector. The shot noise is determined by the optical configuration of the interferometer and the method by which the position of the test masses are measured [57]. The shot noise causes changes in the estimation of the position of the fringes due to the uncertainty of the

number of photons arriving at the photo-diode. The sensitivity can be given as a rough scale for the noise, assuming a standard interferometric detector [45]

$$\text{detectable strain } (\text{Hz})^{-1/2} = \frac{1}{L}\left[\frac{\lambda hc}{\pi^2 P}\right]^{1/2} \tag{1.30}$$

where L is the arm length of the detector, laser power given as P, λ represents the wavelength of the laser and h and c are the Planck's constant and the speed-of-light, respectively and it is assumed that the photodetectors have a unity quantum efficiency. This equation shows that longer arm lengths and/or if the power of the laser is increased, the detectable strain is improved.

Radiation pressure noise at low frequencies

Radiation pressure arises from fluctuations in laser power and affects the test masses as the power fluctuates. The photons are scattered independently and there is a statistical uncertainty as to their division in the beam-splitter [35]. This means there is a Poisson distribution of N photons with a $\sqrt{N}$ fluctuation of force from radiation pressure [67]. Where the shot noise is due to a fluctuation in the number of photons at the photodiode, radiation pressure is due to the uncertainty in the amplitude component of the laser field [67]. For a simple Michelson interferometer, the changing motion of mass m due to radiation pressure at angular frequency ω far above the pendulum resonance is given by

$$\delta x^2(\omega) = \left(\frac{4Ph}{m^2\omega^4 c\lambda}\right), \tag{1.31}$$

where h is Planck's constant, c is the speed-of-light and λ is the wavelength of the laser [35].

This noise source is relevant at lower frequencies for Advanced LIGO, at about 10 to 50 Hz [40]. If the masses of the mirrors are greater, they will be more stable and

resistant to moving due to radiation pressure [67]. Another solution is to decrease the power of the laser, but that will have an effect on higher frequencies and decrease the shot noise improvement, which is affected inversely to the laser power.

Once these frequency ranges are made available in Advanced LIGO, longer measurements of neutron stars can be achieved. Additionally, the lower frequencies will allow earlier observations of coalescence from massive objects (around the $100\,M_{\odot}$ range) [40].

1.3 Astrophysical candidates for initial gravitational wave detection

Gravitational waves are caused by accelerating masses, similar to how accelerating charges result in electromagnetic radiation. There are four main types of gravitational wave radiation that current ground-based detectors are suited to detect: burst, coalescence, stochastic and continuous wave radiation [74]. Burst and coalescence are short-duration events whereas continuous wave and stochastic signals are long-term. Burst signals are transient events for which we do not have a prior signal model. Supernovae, for example, may produce detectable burst signals. Coalescing binaries are commonly studied by relativists and used to generate signal models, which can be exploited in matched template searches. Algorithms that do not assume a signal model designed to detect bursts may also be sensitive to coalescing binaries. Continuous wave (CW) sources produce long term quasi-monochromatic signals expected from rotating neutron stars. Stochastic gravitational wave signals comprise an ensemble of discrete, unresolved sources and possibly may also contain continuous, incoherent background signals which are remnant from the Big Bang.

1.3.1 Short duration gravitational wave events

Burst sources

Bursts are defined as transient, non-repeating signals for which there is not a known template. A core-collapse supernova, for example, may offer a chance to observe a transient gravitational wave signal. As there is little knowledge of the collapse process, it is difficult to calculate an accurate waveform. A burst amplitude of the gravitational wave pulse from a supernova can be estimated as [47]

$$h_0 \sim 1.4 \times 10^{-21} \left(\frac{\Delta E_{\mathrm{GW}}}{10^{-2}\,\mathrm{M}_{\odot}c^2}\right)^{1/2} \left(\frac{1\,\mathrm{ms}}{\tau}\right)^{1/2} \left(\frac{1\ \mathrm{kHz}}{\Delta f_{\mathrm{GW}}}\right) \left(\frac{15\ \mathrm{Mpc}}{r}\right), \qquad (1.32)$$

where ΔE_{GW} is the total energy carried away from the explosion, r is the distance to the source and τ is the duration of the burst. The frequency bandwidth, Δf_{GW}, could range from 100 Hz and 10 kHz. Initial LIGO detectors would be capable of detecting these events, but those that are detectable have a low rate of occurrence.

Coalescence of binary compact objects

The steady inspiral of stars in a compact system due to gravitational radiation results in compact binary coalescence (CBC). This can result in a variety of gravitational wave signals due to the different stages that take place during coalescence. These three stages are the inspiral, the merge then the ring-down. These compact binary systems can be Neutron Star/Neutron Star (NS/NS), Neutron Star/Black Hole (NS/BH) or Black Hole/Black Hole (BH/BH) [74]. Currently there are a few NS/NS systems known, including the famous PSR B1913+16 referred to in Weisberg and Taylor, 1913 [84] with the result shown in Figure 1.5. Standard NS/NS systems are thought to be the remnants of a binary star system that survives the double supernova process or captured neutron stars in dense populations such as globular clusters. These systems have orbits that decay over the time period of a

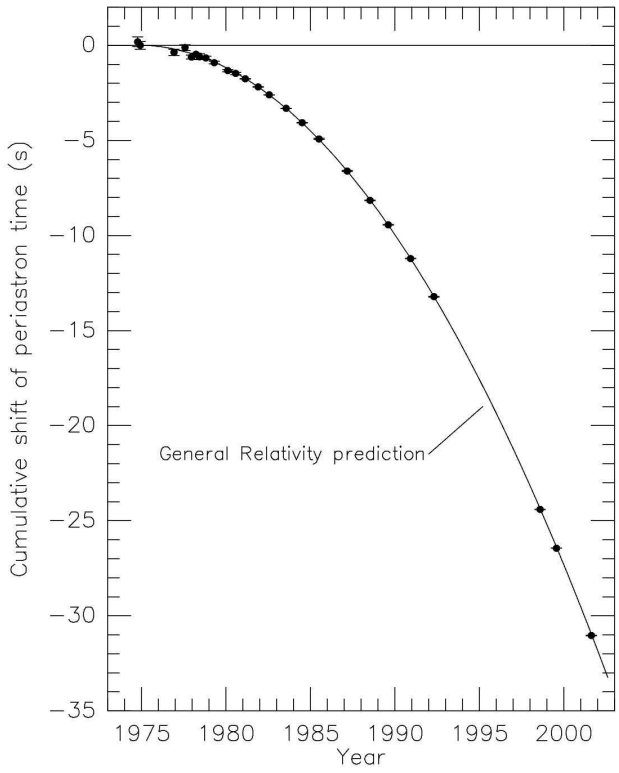

Figure 1.5 – The inspiral of binary system PSR B1913+16 due to gravitational radiation. The points are the observed data and the line is the decay predicted by general relativity [84].

few million years, so there is a significant population of these systems present at any one time.

The gravitational waves from these systems emitted during the inspiral phase carries energy away from the system and the orbital period decreases. The subsequent merging stage results in a gravitational wave 'chirp' when the masses collide. The ring-down stage is considered the settling period of the rotation of the system to a more symmetric object and this emits a short period of relaxing gravitational waves. To give an estimation of mergers, we assume there are 10^5 galaxies within 100 Mpc and quote our rate in events per year. Rates for NS/NS coalescence is derived from direct observations of these systems and is approximately 0.1–50 yr^{-1}. For NS/BH inspirals, the rate is estimated to be 0.01–10 yr^{-1} [47]. The BH/BH systems must be estimated from two sources: one *not* contained in dense star clusters and one for

binaries in such clusters. These rates are 0.01–1 yr^{-1} and 0.1–1 yr^{-1}, respectively [47]. Current results from [22] states that BH/BH binaries may be slightly more likely for gravitational wave detection than previously considered making them the best candidates for detection due to further analysis of black hole populations. Analysis of these gravitational waves would provide a more comprehensive understanding of the distribution and processes of these systems.

1.3.2 Long duration gravitational wave events

Stochastic sources

The stochastic gravitational wave background can be broken up into two main possible sources. The first comprises an ensemble of a large number of weak, discrete gravitational signals. These could be local white dwarf or neutron star binary systems or from powerful extra-galactic black hole binary systems which would emit much stronger signals. The second stochastic gravitational wave signal source is from the early moments of the Universe, similar to the Cosmic Microwave Background (CMB). The CMB results from when the Universe, about 300 000 years after the Big Bang, became transparent to photons during the recombination phase, resulting in a large electromagnetic flux that is still present today. This stochastic gravitational wave is a flux of gravitons left over from when the Universe became optically thin to gravitons, just before Big Bang Nucleosynthesis (BBN) occurred. This would show up as a flat spectrum. This would offer observations of the earliest possible moments in our Universe, providing a insight to the processes that occurred before BBN [11]. These signals are difficult to detect by ground-based interferometers, but identification will be interesting in later-generation detectors to both study early-time cosmology of the Universe and to classify the background of local sources.

Non-axisymmetric neutron stars

Continuous gravitational waves from non-axisymmetric neutron stars are understood to be long-lasting, quasi-monochromatic gravitational waves [69]. These signals are fundamentally different in terms of extraction to the short duration events. For continuous gravitational waves, they are present over longer time-scales so the signal-to-noise ratio (SNR) can potentially increase by simply increasing the observation time. The main source of these signals are young, rapidly spinning neutron stars. As continuous gravitational waves are the main focus of this thesis, I will go into more detail on this source and the relevant equations in Chapter 2.

Neutron stars were first proposed by Baade and Zwicky in 1934 to be the product of a normal star from a supernova [18]. When a massive star goes through gravitational collapse and the gravitational potential energy is released, the outer layers of the star are blown away and the core collapse results in a neutron star. Because of the Pauli exclusion principle, the neutrons are not able to degenerate to the same place and quantum state. The mass of the neutron star is between 1.35 and 2 $M_{\odot}$ due to the Chandrasekhar limit [25]. Though the mass is comparable to our Sun, the typical radius of a neutron star is on the order of 10 km.

Neutron stars are born with a high rotation speed, thought to be due to the conservation of angular momentum in this process. This speed decreases as the neutron star ages and neutron stars typically have a rotation period between 1.4 ms and 12 s according to the ATNF database [58]. Neutron stars also have the possibility of spinning up, due to accretion or glitches. Glitches in the star may occur due to an angular momentum transfer between the solid outer crust and the interior of the star, with the behaviour pointing to a possible superfluid interior [21].

The first pulsar was discovered in 1967 by Bell and Hewish [41] and since then, there have been almost 2000 observations of pulsars throughout the electromagnetic spectrum, all logged at the ATNF database [58]. Some notable neutron stars relevant

to continuous wave searches include the Crab Pulsar (PSR B0531+21) which is a young pulsar, a remnant of supernova SN1054 [39] whose signals are searched for using the Narrow-band search in Chapter 5, Scorpius X-1, an accreting neutron star in the X-ray spectrum[76] and the Vela Pulsar, which emits in radio, optical, X-ray and gamma-ray radiation and is located in the Vela constellation and is associated with the Vela Supernova Remnant [54]. It rotates with $\sim 100\,\mathrm{ms}$ periods and has been known to glitch. A gravitational wave search was performed on one of the recent glitches [3].

1.4 The future of interferometric gravitational wave detection

Currently, the initial gravitational wave detectors LIGO and Virgo are being upgraded to the so-called "second generation" of detectors. These detectors include Advanced LIGO, Advanced Virgo and GEO-HF. This is the first step in developing more advanced and sensitive gravitational wave detectors. Additional plans include the Einstein Telescope, the "third generation" telescope as well as space-based telescopes and new additions to the world-wide network of gravitational wave detectors.

1.4.1 Second generation ground-based detectors

Since the initial LIGO detectors reached their sensitivity level [14] as seen in Figure 1.4, the Advanced LIGO network is currently being installed and constructed to improve current sensitivity by an estimated factor of 10 [40]. These detectors will have improved hardware systems, from the optics to the suspension systems. The current plan for the second Hanford detector is to move the location to India and have a 4 km baseline.

The sensitivity of Advanced LIGO will be significantly improved over Initial LIGO. First, the sensitivity will be an order of magnitude better, with a strain noise down to $\sim 3 \times 10^{-24}\,\mathrm{Hz}^{-1/2}$. The bandwidth will also be widened down to 10 Hz, making available previously undetectable signals in the range of 10-40 Hz [40].

A factor of 10 improvement in sensitivity results in a factor of 1000 improvement in the volume of space from which signals can be detected. Detailed analysis of these improved event rates is given in Mandel *et al.*, 2008 [59]. Due to this greater sensitivity, Advanced LIGO will be more involved in multi-messenger astronomy, adding detections in gravitational waves to neutrino and electromagnetic detection methods in astronomy. More details of the plans for Advanced LIGO can be found in Harry, *et al.* [40].

1.4.2 Improving ground-based detector methods: The Einstein Telescope

Future enhancements to Advanced LIGO will result in the "third-generation" detector, the Einstein Telescope. The advanced detectors are improving readily available technology whereas the third generation detectors will utilise new techniques to improve sensitivity. The goal of this third generation detector is to further improve sensitivity by a factor of 10 over the advanced detectors as well as expand the frequency band [71]. This will allow more detailed measurements of astrophysical phenomena than would be possible with the advanced detectors.

To achieve this improved sensitivity, the relevant technologies must be improved beyond current techniques. For example, installing the Einstein Telescope below ground, significantly reduces the seismic noise and gravitational gradient of the detectors. Additionally, the Einstein Telescope will utilise cryogenics to reduce the thermal noise component of the sensitivity curve [71].

Further solutions to improve the detector systems is to implement multiple interferometers to optimise both high and low frequencies. To include these multiple interferometers, the traditional L-shape can be replaced with a triangle shaped detector with arm lengths of 10 km [71].

1.4.3 Space-based detectors: exploring astrophysics at low frequencies

In addition to the ground-based gravitational wave interferometers, different frequency bandwidths can be explored with different methods. By developing space-based detectors signals at low frequencies can be detected which would not be possible due to seismic noise on the ground. As of May 2012, the space-based observatory, the New Gravitational wave Observatory (NGO) was not selected for the next round of funding by the European Space Administration (ESA). With hopes that it will be funded in the next round, it will aim to be operable in the next decade. This detector relies on the framework established by LISA and the LISA Pathfinder, previous projects jointly supported by NASA and ESA. LISA was abandoned due to funding issues and redeveloped as the NGO [78].

A bandwidth of 0.1 mHz to 1 Hz is the aim for NGO and would allow detections from many astrophysical sources, such as massive black hole mergers and possible remnant signatures from the Big Bang. This bandwidth is determined from optimising the science that can be done, accounting for limitations from the travel distance between the mirrors and accounting for radiation pressure. The detector will utilise 2 interferometer arms with 3 spacecraft in a triangular formation with arm lengths of 10^6 km [78].

As further detector techniques are improved, the data analysis community must ensure that they can keep up with the challenges. Formal data challenges are developed to address possible issues that might arise with the improved detectors. This

allows the data analysis community to keep up with the detector developments, maximising the available time once they are online which will allow an early detection. The Mock LISA Data Challenge (MLDC) exists for just such a purpose as the space-based detectors are developed [4] [16]. The MLDC helps because techniques are created for data and signals never searched for previously.

1.5 Motivation and structure for thesis

Given these future plans for gravitational wave detectors, the community will move from placing upper limits on signals to making actual detections. Due to this fact, a strategy needs to be developed in order to maximise the possibility of a confirmed detection. This thesis introduces various important considerations as well as a hierarchical strategy for the detection of continuous gravitational waves utilising multiple existing search algorithms. Details of continuous gravitational waves are given in Chapter 2 including detailed mathematics, current search algorithms, recent results from the initial detector runs and current detection criteria.

In the advanced detector era, It is important to consider the effect that increased sensitivity will have on various searches. Adding more detectors to the network is one way to improve sensitivity. Chapter 3 discusses the effect of sensitivity on continuous gravitational wave detections from neutron stars due to additional detectors.

The hierarchical method for searches involves a sequence of searches already existing in the continuous wave group, but currently operating independently, each refining the estimates and improving the likelihood. The first step is a blind, all-sky search which has no expected parameters. These searches produce a list of candidates with a coarse parameter estimate. These candidates are passed on to a narrow-band, multi-template search to improve the parameter estimation. The highest likelihood

[4] `http://astrogravs.nasa.gov/docs/mldc/`

template is passed on to a Bayesian search which targets the specific parameters to establish posterior distributions on the gravitational wave parameters.

After discussing the possible sensitivity improvement due to additional detectors, this thesis addresses each step of the hierarchical detection method and potential issues. In Chapter 4, the effects of neutron star motions and distances on the blind, all-sky search, Einstein@Home are explored.

The next chapter, Chapter 5 introduces the Narrow-band Search, an algorithm which evaluates likelihood statistics at multiple templates from the resolution of candidates passed on from the all-sky searches. This chapter presents two results from the narrow-band search, one a stand-alone search for signals from the Crab Pulsar in the most recent science run of LIGO. The second result is a detection of a hardware injected signal in the same science run.

Finally, Chapters 6 and 7 present the development of a signal challenge for the continuous wave group and initial results, to prepare for the era of likely detections. Chapter 6 presents the methodology and approach to the development of this challenge, from generating the data to the parameters of the artificial signals which are included. Following, in Chapter 7, initial results from a blind all-sky search as well as stand-alone verification of signals using the final, targeted search.

2

Searching for continuous gravitational waves

This chapter will describe how continuous gravitational waves could be generated and the current status of continuous gravitational wave searches. First, these equations for continuous waves includes details which will affect how searches are developed. These searches will then be described along with their recent results. We will then discuss the current detection criteria for the continuous wave group and consider how they may be tested and improved.

2.1 Mechanisms for continuous gravitational waves from neutron stars

There are three understood mechanisms under which a continuous gravitational wave will be created. The first is a non-axisymmetric distortion of the neutron star itself. This can be described in terms of the neutron star's equatorial ellipticity defined as,

$$\epsilon \equiv \frac{I_{\mathrm{xx}} - I_{\mathrm{yy}}}{I_{\mathrm{zz}}}, \tag{2.1}$$

where I_{ii} correspond to the three principal moments of inertia [49]. This can also be thought of as a persistent 'bulge' on the neutron star. This deformation could persist from elastic stresses in the crust or by magnetic fields [69].

The amplitude of such a signal can be described as

$$h_0 = \frac{16\pi^2 G}{c^4}\frac{I\nu^2}{r}\epsilon, \tag{2.2}$$

for a neutron star at distance r with a spinning frequency ν and a moment of inertia I with respect to the rotation axis [49]. To simplify this equation, we can replace the physical constants and get (from [49])

$$h_0 = 4.23 \times 10^{-25} d_0 \left(\frac{\nu}{100\ \mathrm{Hz}}\right)^2, \tag{2.3}$$

where

$$d_0 \equiv \left(\frac{\epsilon}{10^{-5}}\right)\left(\frac{I}{10^{45}\mathrm{g\ cm}^2}\right)\left(\frac{1\mathrm{kpc}}{r}\right). \tag{2.4}$$

The values given for d_0 are astrophysically understandable so we can estimate a likely h_0 and sensitivity which we need to reach for an optimally oriented source with respect to the detector. The most unlikely value given is that of the equatorial ellipticity, ϵ because current estimations and calculations of known neutron star ellipticities have an approximate upper limit of 10^{-6}. The maximal deformation supported by the neutron star's crust rigidity is estimated as

$$\epsilon_{\mathrm{max}} \approx 5 \times 10^{-7}\left(\frac{\sigma}{10^{-2}}\right), \tag{2.5}$$

where σ is the breaking strain of the solid crust [80]. The coefficient is particularly small mainly because the shear modulus of the inner crust is small compared to the pressure [69].

It is important to think about the possible deformations which are likely to exist

in real neutron stars. One possibility is that after a glitch, where stresses in the crust built up to the point of breaking, it could take a significant period of time in comparison to the lifetime of a glitch, and long enough for our continuous wave algorithms to detect it for the mass distribution to return to being axisymmetric. Another possibility is accreting binary neutron stars. The accretion process could create a 'hot spot' on the surface due to the magnetic fields. This 'hot spot' could result in a buildup of the ellipticity. Furthermore, extremely strong magnetic fields could produce high magnetic tension which could produce a non-axisymmetric deformation.

A second mechanism for gravitational wave emission from neutron stars is non-axisymmetric instabilities from birth or during phases of accretion for rapidly rotating neutron stars. For example, a neutron star with a sufficiently high rotation rate could have a dynamic instability due to hydrodynamics and gravitational forces [69].

The third main mechanism for gravitational wave emission is free precession, or the movement of a neutron star which has a misaligned rotation axis with respect to the symmetry axis (with a wobble angle, θ_{w}) [69]. A large θ_{w} could result in a gravitational wave amplitude of

$$h_0 \sim 10^{-27} \left(\frac{\theta_{\mathrm{w}}}{0.1 \text{ rad}}\right) \left(\frac{1 \text{ kpc}}{r}\right) \left(\frac{\nu}{500 \text{ Hz}}\right)^2 \tag{2.6}$$

This would give gravitational wave emission at $f = \nu + \nu_{\mathrm{prec}}$ where ν_{prec} is the precession frequency as well as the twice the spinning frequency, $f = 2\nu$ [69]. It is possible for free precession to last for $\sim 10^5$ years [27] so while it may not be a high amplitude, it is an interesting candidate for next-generation detectors (like Advanced LIGO).

Important parameters used in gravitational wave searches from neutron stars are

referred to as Doppler parameters, $\boldsymbol{\delta}_i$, and gravitational wave amplitude parameters, $\mathcal{A}_i$. These are shown in Table 2.1 and Table 2.2, respectively.

ν	Spin frequency
f_{gw}	Frequency of the gravitational wave (typically 2ν)
$\dot{f}_{\mathrm{gw}}$, $\ddot{f}_{\mathrm{gw}}$, ...	Frequency derivatives
α	Right ascension
δ	Declination

Table 2.1 – Doppler parameters, $\boldsymbol{\delta}_i$, of neutron stars for the purpose of gravitational wave observation.

h_0	Amplitude of the gravitational wave signal
ι	Inclination of the spin axis
ϕ_0	Initial phase of the signal
Ψ	Polarisation angle
A_+	Plus-polarisation amplitude
$A_\times$	Cross-polarisation amplitude

Table 2.2 – Gravitational wave parameters, $\mathcal{A}_i$, of signals from neutron stars. The parameters Ψ and ι are shown in Figure 2.1 and the definitions for A_+ and $A_\times$ are given in Equations 2.7.

While the parameters h_0 and $\cos\iota$ are used, sometimes the parameters A_+ and $A_\times$ are used. These are defined as

$$A_+ = \frac{1}{2}h_0(1+\cos^2\iota), \tag{2.7a}$$

$$A_\times = h_0\cos\iota. \tag{2.7b}$$

which describe the polarisation amplitudes in the plus and cross directions [69].

2.2 Loudest expected signal from neutron stars

It is expected, based on current models, that there are $\sim 10^9$ neutron stars in our galaxy and approximately 10^5 are active [69]. As mentioned in Section 1.3.2, approximately 2000 known neutron stars have been observed. This low number

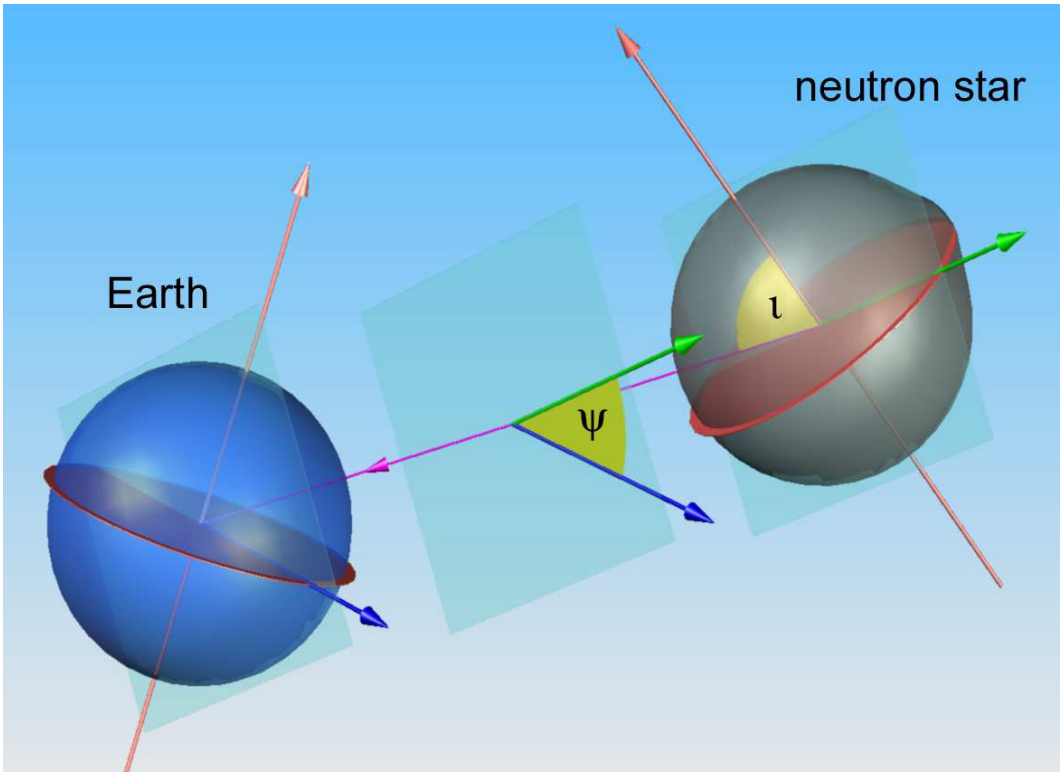

Figure 2.1 – Diagram depicting the angular parameters Ψ and ι of a neutron star for continuous gravitational waves. Image courtesy of John T. Whelan.

(compared to the expectation) is mostly due to the fact that the majority of neutron stars are not pulsars which can be detected and partially has to do with selection effects due to the neutron star orientation with respect to Earth.

There is an argument that a statistical upper limit can be made on the expected gravitational waves of neutron stars, practically independent of the individual physics. This argument was first made by Blandford and further investigated by Knispel and Allen, 2008 [52]. If one assumes an isotropic distribution and constant birthrate of neutron stars that primarily radiate gravitational waves, there is a 50% chance that the strongest signal between 50 Hz and 2 kHz has an amplitude of at least [69]

$$h_0 \sim 4 \times 10^{-24}. \tag{2.8}$$

This number is consistent with the non-detections in initial LIGO runs given the fact that the sensitivity of the initial LIGO detectors was above this value. Advanced

LIGO is expected to have higher sensitivity which will allow for regular detections of this amplitude.

2.3 Calculating the gravitational wave upper limit from neutron stars

In the previous section, statistical arguments were given for a likely continuous wave signal in the LIGO band. If we have a pulsar with known parameters such as a measured spin, ν and spin-down, $\dot{\nu}$ and a distance r which is emitting gravitational waves at a frequency $f = 2\nu$ due to a non-axisymmetric deformation ϵ, we can derive a robust upper limit on h_0. The gravitational wave luminosity of such a pulsar can be written as [69]

$$L_{\mathrm{GW}} = \frac{1}{10}\frac{G\pi^6}{c^5}\nu^6 I_{zz}^2 \epsilon^2. \tag{2.9}$$

We can assume that the gravitational wave emission is purely due to the rotational energy, E_{rot}, then we can state,

$$L_{\mathrm{GW}} \leq -\dot{E}_{\mathrm{rot}} = -2\pi^2(2I_{zz}\nu\dot{\nu} + \nu^2\dot{I}_{zz}), \tag{2.10}$$

and if the moment of inertia is constant, $\dot{I}_{zz} = 0$ the we can describe an upper limit on the deformation $\epsilon < \epsilon_{\mathrm{sd}}$ as

$$\epsilon_{\mathrm{sd}} = \sqrt{\frac{5c^5}{2(4\pi)^4 G I_{zz}}\frac{|\dot{\nu}|}{\nu^5}}. \tag{2.11}$$

This can be substituted into 2.2 to give an upper limit of

$$h_0 \leq h_{\mathrm{sd}} = \frac{1}{d}\sqrt{\frac{5GI_{zz}}{2c^3}\frac{|\dot{\nu}|}{\nu}}. \tag{2.12}$$

The spindown upper limit, h_{sd} is calculated for all known neutron stars in the ATNF database[1][58] using the canonical moment of inertia as $I_{zz} = 10^{38}\,\mathrm{kg\ m^2}$. These values are plotted against the sensitivity curves for the sixth science run (S6) with the Hanford and Livingston 4 km arm detectors in Figure 2.2.

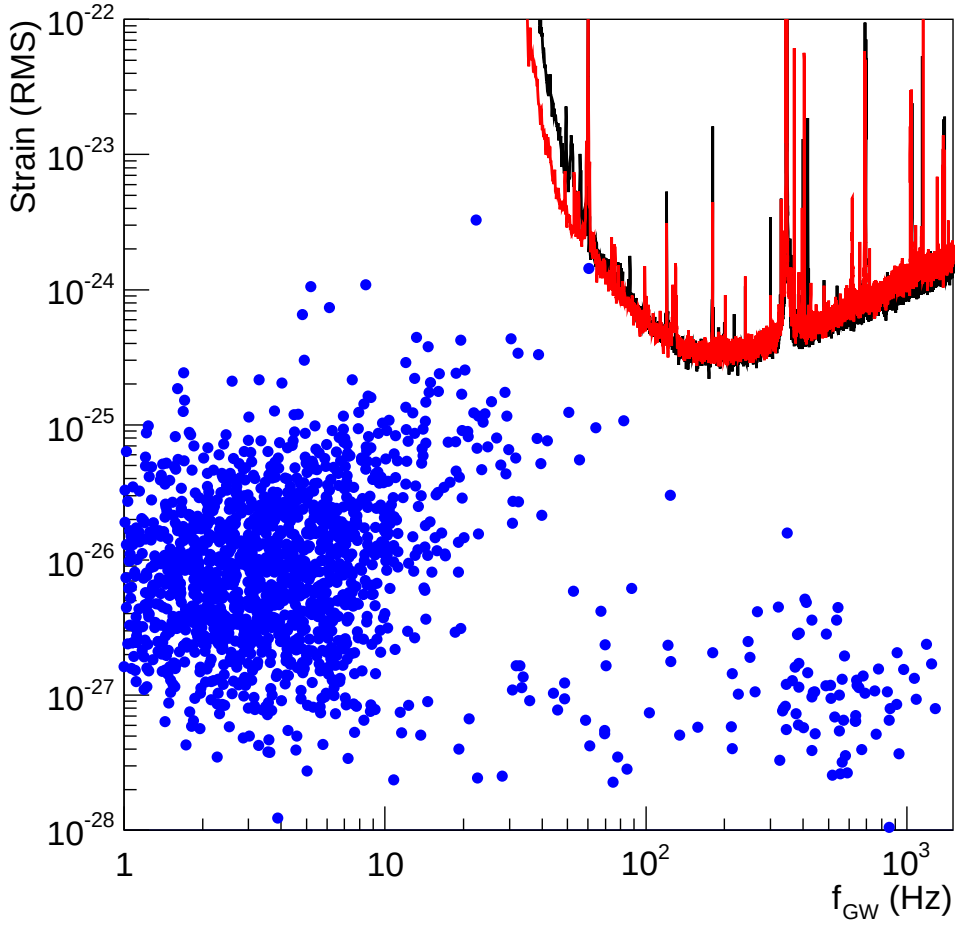

Figure 2.2 – The spindown upper limits calculated for known pulsars in the ATNF database using Equation (2.12) against the S6 sensitivity curves for the Hanford and Livingston 4 km detectors.

[1] `http://www.atnf.csiro.au/people/pulsar/psrcat/`

2.4 Approaches to continuous wave data analysis

As mentioned in Section 1.1, the equation for the amplitude of the signal on Earth can be given by [49]

$$h(t) = F_+(t)h_+(t) + F_\times(t)h_\times(t). \tag{2.13}$$

To do proper data analysis of these signals, the beam-pattern functions F_+ and $F_\times$ can be time-dependent functions of the position of the source (RA and DEC) and the polarization angle, Ψ [49]. Following the mathematics in [49], we get the following equations:

$$F_+(t) = \sin\zeta[a(t)\cos 2\psi + b(t)\sin 2\psi], \tag{2.14}$$

$$F_\times(t) = \sin\zeta[b(t)\cos 2\psi - a(t)\sin 2\psi], \tag{2.15}$$

where ζ is the angle between the two arms (ideally $\pi/2$) and

$$\begin{aligned} a(t) =& \frac{1}{16}\sin 2\gamma(3-\cos 2\lambda)(3-\cos 2\delta)\cos[2(\alpha-\phi_r-\Omega_r t)] - \frac{1}{4}\cos 2\gamma\sin\lambda(3-\cos 2\delta) \\ & \sin[2(\alpha-\phi_r-\Omega_r t)] + \frac{1}{4}\sin 2\gamma\sin 2\lambda\sin 2\delta\cos[\alpha-\phi_r-\Omega_r t] - \frac{1}{2}\cos 2\gamma\cos\lambda \\ & \sin 2\delta\sin[\alpha-\phi_r-\Omega_r t] + \frac{3}{4}\sin 2\gamma\cos^2\lambda\cos^2\delta, \end{aligned} \tag{2.16}$$

$$
\begin{aligned}
b(t) = &\cos 2\gamma \sin\lambda \sin\delta \cos[2(\alpha - \phi_r - \Omega_r g)] + \frac{1}{4}\sin 2\gamma(3 - \cos 2\lambda) \\
&\sin\delta \sin[2(\alpha - \phi_r - \Omega_r t)] + \cos 2\gamma \cos\lambda \cos\delta \cos[\alpha - \phi_r - \Omega_r t] + \frac{1}{2}\sin 2\gamma \sin 2\lambda \\
&\cos\delta \sin[\alpha - \phi_r - \Omega_r t)]. \qquad (2.17)
\end{aligned}
$$

where λ is the latitude of the detector site on the Earth, Ω_r is the rotational angular velocity of the Earth and ϕ_r is a deterministic phase which defines the position of the Earth in its diurnal motion at $t = 0$. Equations 2.14 - 2.17 allow us to compute the beam pattern at any instant of t. By following Appendix A of Jaranowski, Królak and Schutz 1998 [49], the phase model of the gravitational wave signal is

$$
\Psi(t) = \Phi_0 + 2\pi \sum_{k=0}^{s} f_0^{(k)} \frac{t^{k+1}}{(k+1)!} + \frac{2\pi}{c}\mathbf{n}_0 \cdot \mathbf{r}_{\mathrm{d}}(t) \sum_{k=0}^{s} f_0^{(k)} \frac{t^k}{k!}, \qquad (2.18)
$$

where $f_0^{(k)}$ is the kth time derivative of the frequency measured at $t = 0$ at the Solar System Barycentre (SSB), $\mathbf{n}_0$ is the unit vector pointing to the star in the SSB frame and $\mathbf{r}_{\mathrm{d}}$ is the position vector of the detector in the SSB reference frame.

The SSB reference frame states that the x axis is parallel to the x axis of the celestial sphere coordinate system and the z axis is perpendicular to the ecliptic. This means that the vector $\mathbf{n}_0$ has the components

$$
\mathbf{n}_0 = \begin{pmatrix} 1 & 0 & 0 \\ 0 & \cos\varepsilon & \sin\varepsilon \\ 0 & -\sin\varepsilon & \cos\varepsilon \end{pmatrix} \begin{pmatrix} \cos\alpha\ \cos\delta \\ \sin\alpha\ \cos\delta \\ \sin\delta \end{pmatrix} \qquad (2.19)
$$

where ε is the angle between the ecliptic and the Earth's equator and α and δ are the position coordinates (RA and DEC, respectively) of the star. The vector $\mathbf{r}_{\mathrm{d}}$ has

the components

$$\mathbf{r}_{\mathrm{d}} = R_{ES} \begin{pmatrix} \cos(\phi_0 + \Omega_0 t) \\ \sin(\phi_0 + \Omega_0 t) \\ 0 \end{pmatrix} + R_E \begin{pmatrix} 1 & 0 & 0 \\ 0 & \cos\varepsilon & \sin\varepsilon \\ 0 & -\sin\varepsilon & \cos\varepsilon \end{pmatrix} \begin{pmatrix} \cos\lambda\ \cos(\phi_r + \Omega_r t) \\ \cos\lambda\ \sin(\phi_r + \Omega_r t) \\ \sin\lambda \end{pmatrix}, \tag{2.20}$$

where R_{ES} is the distance from the Earth to the SSB (mean value of 1 AU), R_E is the mean radius of the Earth, Ω_0 is the mean orbital angular velocity of the Earth and ϕ_0 is a deterministic phase (that is, a phase which will produce the same output no matter what starting condition given) which defines the position of the Earth in its orbital motion at $t = 0$. The eccentricity of Earth's orbit and the motion around the Earth-Moon barycenter is neglected [49].

Finally, in [49], a two-component model of the gravitational wave signal is defined as

$$h(t) = h_1(t) + h_2(t), \tag{2.21}$$

where

$$\begin{aligned} h_1(t) &= F_+(t)h_{1+}(t) + F_\times(t)h_{1\times}(t), \\ h_2(t) &= F_+(t)h_{2+}(t) + F_\times(t)h_{2\times}(t), \end{aligned} \tag{2.22}$$

and

$$\begin{aligned} h_{1+}(t) &= \frac{1}{8}h_0\ \sin 2\theta_{\mathrm{w}}\ \sin 2\iota\ \cos\Psi(t), \\ h_{2+}(t) &= \frac{1}{2}h_0\ \sin^2\theta_{\mathrm{w}}(1+\cos^2\iota)\ \cos 2\Psi(t), \end{aligned} \tag{2.23}$$

$$\begin{aligned} h_{1\times} &= \frac{1}{4}h_0\ \sin 2\theta_{\mathrm{w}}\ \sin\iota\ \sin\Psi(t), \\ h_{2\times} &= h_0\ \sin^2\theta_{\mathrm{w}}\ \cos\iota\ \sin 2\Psi(t), \end{aligned} \tag{2.24}$$

where θ_{w} as described in Section 2.1 is the wobble angle of the star. The equations

defining $h(t)$ given above define the quadrupolar gravitational wave signal which is emitted by a free precessing axisymmetric star [49].

2.5 Current continuous gravitational wave search algorithms

The continuous wave (CW) working group, as part of the LIGO/Virgo Scientific Collaboration, have developed many methods for searching for continuous gravitational waves from non-axisymmetric neutron stars. These varied searches use either time-domain or frequency-domain data and range from targeted searches to blind, all-sky searches. Targeted searches focus on a specific set of parameters, based on current knowledge of a known neutron star and assumes a spindown directly related to the electromagnetic spindown rate. Directed searches begin with a set of parameters, but allow some variance due to alternative theories of gravitational radiation, or uncertainty in following up candidates from all-sky searches.

2.5.1 Blind all-sky searches

By using blind, all-sky searches we can detect gravitational waves from previously unknown sources. Given the large amount of neutron stars in the Galaxy which have yet to be detected, this is a necessary method for detection. However, these all-sky searches require multiple templates and a large amount of computational time. Two all-sky searches in the CW group are Einstein@Home and PowerFlux. To do a blind, all-sky search requires advanced techniques to cope with the large volume of data as well as the many possible parameters and unknowns over which to search.

Einstein@Home copes with these issues by utilising a volunteer computing network

to achieve a more sensitive search. This allows the use of a longer coherent integration time with a large parameter space. Einstein@Home is also used to detect previously unknown pulsars using radio data from surveys based at Arecibo and Parkes Telescopes.[2] Recent results from Einstein@Home are given from the S5 run in [12]. Further details about the Einstein@Home search is given in Chapter 4 where the effect of neutron star motion on the parameter space is explored.

Another all-sky search is PowerFlux developed by Vladimir Dergachev. PowerFlux is a semi-coherent search method which is capable of performing multiple spindown searches. Candidates from PowerFlux are passed on to the Narrow-band directed search to followup the proposed parameter space. The recent all-sky search for periodic signals in S5 data is given in [4]. Further details of the PowerFlux search is given in Chapter 7 where PowerFlux is used to initially analyse the software injections described in this thesis.

2.5.2 Multi-template narrow-band parameter search

The directed searches in the CW group use more refined parameters to focus on a possible candidate either from a known neutron star or can be used to study a candidate from the all-sky searches. This search still uses multiple templates to allow the parameters of the search to vary either due to the uncertainty in the candidate as well as allowing for the possibility of variance in the physics of the source. This search is referred to as the "narrow-band" search and is further detailed in Chapter 5 with results from the recent science run of LIGO.

The directed searches use the $\mathcal{F}$-statistic first derived by Jaranowski, Królak and Schutz ([49]) and is the optimal statistic for the detection of continuous gravitational waves. The single-detector, single-source calculations from [49] are updated by Cutler and Schutz [28] to include multiple detectors and multiple sources.

[2] `http://einstein.phys.uwm.edu/`

This directed search searches over a frequency $f_{\rm gw} = 2f_{\rm spin}(1+\delta)$ where δ is a small number to allow for possible astrophysical variances. This can occur if the gravitational waves are produced by a component of the neutron star spinning separately from the electromagnetic component. These two components are linked by a torque which enforces the co-rotation on a timescale $\tau_{\rm coupling}$. In this case, $\tau_{\rm coupling}$ is related to δ as $\delta \sim \tau_{\rm coupling}/\tau_{\text{spin-down}}$ where $\tau_{\text{spin-down}}$ is related to the characteristic age of the pulsar [10]. This can also occur with free precession of a nearly biaxial star which would result in $\delta \sim \alpha(I_{\rm zz} - I_{\rm xx})/I_{\rm xx}$ where α is dependent on the geometry of the star [10].

The small variance δ in this search can also be applied when following up blind search candidates. These searches will produce an uncertainty in the estimated parameters, which can be used in the search to refine the parameters.

This directed search method has been used in conjunction with the targeted search mentioned in the next section to place an upper limit on the spindown from the Crab pulsar [10]. It has also been used to recently place an upper limit on the spindown from the supernova remnant Cassiopeia A in the S5 data [87].

In addition to being used with the targeted search, this method is a useful one because it can operate alone on a known pulsar (as done in Chapter 5) or as an independent follow-up analysis of viable candidates from all-sky searches.

2.5.3 Targeted MCMC search

The main targeted search in the CW group was developed at the University of Glasgow and uses time-domain raw data and Bayesian methodology to produce posterior distributions for the gravitational wave parameters. While this search relies on a large data set, the targeted search focuses on a small frequency band, complex heterodyning, filtering and resampling to reduce the size of the data by a

factor of $\sim 10^6$ [34].

First, a slowly evolving complex heterodyne is performed to unwind the phase evolution of the source. This leaves a residual timing signature from the motion of the source. Since this motion is over a long time scale with respect to the frequency of the source, the data can be resampled down to a bandwidth of 1/60 Hz centred on the expected frequency [34]. Prior to averaging this data for analysis, the next step is to apply a low-pass anti-aliasing filter to the heterodyned data. Finally, the filtered data is resampled to the post-filtering Nyquist rate and averaged over a minute to form the data segments used in analysis [34].

In practise, this modification of the data is done in two steps. The first step with a fixed heterodyne frequency and a filter which reduces the sample rate to 4 Hz. The second has a variable heterodyne frequency is used to remove the Doppler effects due to motion of the Earth. This is particularly useful because the calculation of Doppler effects then only has to happen 4 times a second as opposed to 16384 times a second, the original sample rate. Once these calculations are made, the data is further resampled and binned down to 1/60 Hz [34].

Bayes' Theorem and marginalisation

With resulting binned data sets, B_k, Bayesian formalism is applied to calculate the posterior probability of the gravitational wave parameters. This formalism is shown as

$$p(\mathbf{a}|\{B_k\}, I) = \frac{p(\mathbf{a}|I)p(\{B_k\}|\mathbf{a}, I)}{p(\{B_k\}|I)} \tag{2.25}$$

where $\mathbf{a}$ is the inferred set of parameters from the binned data B_k and I is the model of the signal with likelihood $p(\{B_k\}|\mathbf{a}, I)$. The prior distributions for the parameters are given as $p(\mathbf{a})$ and the least informative priors are typically used [34].

The main parameter of interest is the amplitude, h_0 with a marginal probability

distribution function of

$$p(h_0|\{B_k\}) \propto \int\int\int p(\{B_k\}|\mathbf{a})p(\mathbf{a})d\phi_0 d\Psi d\cos\iota, \tag{2.26}$$

with numerical integration over the full range of the parameters [34].

Determining upper limits

Typically, results are quoted as the 95% bounding upper limit of the amplitude h_0 from the cumulative probability distribution. This is calculated as the value h_{95} which satisfies

$$0.95 = \int_{h_0=0}^{h_{95}} p(h_0|\{B_k\})dh_0. \tag{2.27}$$

The likelihood function of these parameters is then calculated with a posterior probability [34]. Further details of this type of search are given in Chapter 7 when it is used for the mock data challenge.

Determining a likely set of parameters

The benefit of this targeted search is that it provides posterior probabilities for the four gravitational-wave parameters described in Section 2.4. Since it is a Bayesian-based search, however, it needs starting estimates for parameters for a single-template. This means that it will only detect signals from previously known sources, or candidates from previous multi-template searches. By using this search in the final step of detections from previously unknown sources, we can optimise its suitability.

The targeted search has been used to place upper limits on known pulsars in the fourth and fifth science runs (S4 and S5 respectively) [8] [13] and most notably the Crab [10] and Vela [3] pulsars.

2.5.4 Hierarchical method for detection

Given the previously described methods above, a natural method for signal analysis can be developed to refine the parameters of a possible detection and combine these algorithms to optimise the process.

The first step in this method is to run the blind, all-sky searches which produce a list of candidates with a rough estimate of signal parameters. These candidates can be passed on to the directed, narrow-band search which can explore the multiple possible templates from the blind search. This search will find the highest likelihood template and then pass it on to a targeted search which can give probability posterior distributions for the parameters. This method is illustrated in Figure 2.3.

2.6 Previous results and upper limit analysis in initial detector runs

To date, no direct detections of continuous gravitational waves have been made, but there have been significant results from the past LIGO, Virgo and GEO600 science runs. Though the sensitivity of these runs have not been sufficient to make a detection, these results test the capabilities of the searches and the time-frame in which they are able to run. Some significant upper limits and results are presented here, ranging from the targeted to the all-sky searches.

2.6.1 Upper limit on the Crab Pulsar from S5 data

One of the more significant results from the recent LIGO science runs placed an upper limit on the Crab Pulsar, PSR B0531+21, gravitational wave emission [10]. This work was primarily conducted by Matthew Pitkin running the targeted search and Joseph Betzweiser running the directed search. This investigation combined

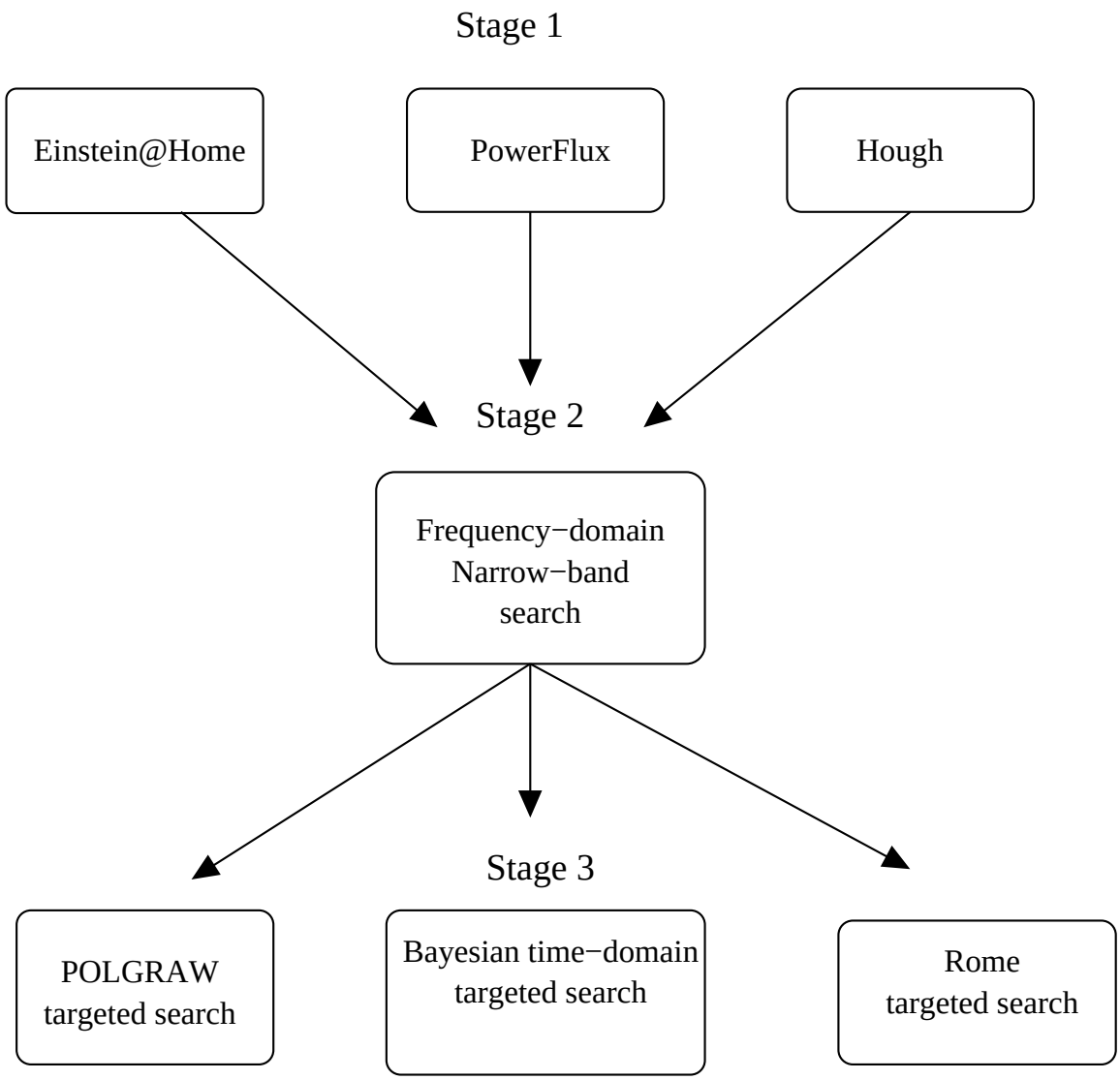

Figure 2.3 – Hierarchical method for continuous gravitational wave detections from previously unknown sources. Step one shows the existing blind, all-sky searches. The possible candidates from these searches can be passed on to the Narrow-band search which can explore the multiple templates around the candidates to establish a likelihoods. A sufficiently strong likelihood template can be passed on to the current targeted searches.

both the time-domain Bayesian targeted search as well as the directed, frequency-domain search for a comprehensive search and estimate of the upper limit $h_0^{95\%}$.

The single-template, time domain search resulted in $h_0^{95\%} = 3.4 \times 10^{-25}$ with uniform priors on the other parameters. With Ψ and $\cos\iota$ being constrained, this value is brought down by a factor of 1.3 to $h_0^{95\%} = 2.7 \times 10^{-25}$. Using the moment of inertia to be $10^{38}\,\mathrm{kg\ m^2}$, and a distance of $r = 2\,\mathrm{kpc}$, the ellipticity of the neutron star is $\epsilon = 1.8 \times 10^{-4}$. Using the uniform priors result, this value for $h_0^{95\%}$ constrains the luminosity of the Crab pulsar due to gravitational radiation to less than 6% of the observed spin-down luminosity, beating previous indirect upper limits [10].

Using the multi-template, frequency domain search resulted in a 95% confidence value for h_0 as $h_0^{95\%} = 1.7 \times 10^{-24}$ and an ellipticity of 9.0×10^{-4} over all templates searched. The larger number of templates increased the statistical confidence threshold thus resulting in larger estimates compared to the targeted search [10].

This search is significant for beginning to constrain the astrophysical properties of the neutron star through gravitational wave observations. Further understanding of the neutron star astrophysics, such as the magnetic field or the composition of the neutron star, would lead to more constrained results.

2.6.2 Vela pulsar upper limit from Virgo data

In 2011 upper limits on the gravitational wave emission from the Vela pulsar, PSR J0835-4510, were estimated using data from Virgo's second science run, which ran from July 2009 to January 2010. Three independent targeting search algorithms were used which assumed the spindown was directly correlated with the radio emission.

The Virgo detector was specifically used in this case due to its operational sensitivity at low frequencies and the Vela pulsar having a frequency of $f_{\mathrm{rot}} = 11.19\,\mathrm{Hz}$. This

is too far below the sensitivity curve for the LIGO detectors.

The three pipelines used for this were the targeted complex heterodyned search with Bayesian analysis and resulting posterior distributions described above, a time-domain matched filter method using the $\mathcal{F}$-statistic with a new extension called the $\mathcal{G}$-statistic developed by Jaranowski and Królak [48] referred to as the POLGRAW search and a matched filter method from a group in Rome which is applied to the Fourier components of the signal's five main frequencies where the signal is spread due to sidereal modulation [17].

No signal was detected in all of the available data from the second science run in Virgo. Upper limits were placed using all three of these methods [3]. The complex heterodyning method produced posteriors with two upper limits based on different prior distributions, in the same manner that was described for the Crab Pulsar. These are $h_0^{95\%} = 2.4 \times 10^{-24}$ and 2.1×10^{-24} respectively [3].

The $\mathcal{F}$ and $\mathcal{G}$-statistics methods produced false alarm probabilities of 22% and 35% respectively, stating that there is a 22% (or 35%) chance that a signal could be detected which does not actually exist. This is far above the set 1% false alarm threshold. However, using monte carlo techniques, 95% upper limits of $h_0^{95\%} = 2.4 \times 10^{-24}$ and 2.2×10^{-24} respectively [3].

The Fourier component search used two methods with 4 and 2 degrees of freedom. For these, false alarm probabilities of 46% and 40%, respectively, were calculated. Again far above the false alarm detection threshold of 1%. The calculated 95% upper limits for these two methods are $h_0^{95\%} = 2.2 \times 10^{-24}$ and 1.9×10^{-24} respectively [3].

Due to the difference in methodology (time-domain versus frequency-domain, Bayesian versus Frequentist), these results can best be compared by understanding how the different searches relate to one another. To get a thorough understanding of this, a Mock Data Challenge with high statistics, such as the one described in Chapters 6

and 7.

2.6.3 Upper limits for the Cassiopeia A remnant in S5

Continuous gravitational waves from the neutron star in the supernova remnant in Cassiopeia A (CasA) were searched for using data from a 12-day interval in the fifth science run of LIGO. There is little known about the compact object at the centre of CasA, so this searched looked at the interval $100 < f_{\mathrm{gw}} < 300\,\mathrm{Hz}$ and a range of first and second spindown frequencies which are related to the known age [1].

This search used the multi-template $\mathcal{F}$-statistic method and made no gravitational wave detection. A 95% amplitude upper limit of $h_0^{95\%} = 0.7{-}1.2{\times}10^{-24}$ is calculated. Additionally, an ellipticity upper limit of $0.4 - 4 \times 10^{-4}$ and an upper limit on the amplitude of the r-mode oscillations is given as 0.005-0.14 [1].

These upper limits of the amplitude beat previous indirect limits and is the first time an upper limit of r-mode oscillations are given [1].

2.6.4 Upper limits from the all-sky searches PowerFlux and Einstein@Home

The PowerFlux algorithm searched two years of data collected during LIGO's fifth science run in the band 50-800 Hz and a spindown range of 0 to $-6 \times 10^{-9}\,\mathrm{Hz\ s^{-1}}$. This is the most sensitive all-sky run to date with an optimal upper limit of 10^{-24} near the 150 Hz frequency band [4].

In this frequency range, the search is sensitive to neutron star ellipticities down to 3.3×10^{-6} and distances out to 425 pc for an unfavourable spin orientation. Assuming the 10^5 active neutron stars in our galaxy discussed in Section 2.2 with a uniform distribution, this corresponds to approximately 35 possible sources within

this distance. If the spin orientation is optimally aligned to the line-of-sight, the ellipticities can be estimated down to 1.2×10^{-6}. No actual continuous wave signals were detected in this data set [4].

Einstein@Home ran a similar all-sky search on LIGO data from S5. It searched 66 days of data in the frequency range 50-1500 Hz with a frequency spindown range of $-f/\tau < \dot{f} < 0.1f/\tau$ with a minimum age of $\tau_{\min} = 1000$ years for $f < 400$ Hz and $\tau_{\min} = 8000$ years for $f > 400$ Hz. This setup is explored further in Chapter 4. Approximately 10^5 volunteer computers were used for this search which allowed a coherent integration time of 30 hrs with a large parameter space. No signals were detected in this data set, and in the frequency range 125-225 Hz, 90% of sources with an amplitude larger than 3×10^{-24} would have been detected [12].

2.7 Current detection criteria

The continuous wave (CW) working group for the LIGO-Virgo Scientific Collaboration has developed a list of detection criteria for a continuous gravitational wave signal. These details are laid out in an internal white paper established in 2009 and can be found in full in [73]. As [73] describes, the continuous wave working group has one of the easiest tasks of all the LVC working groups in establishing detection confidence in the sense that additional observations will yield a higher signal-to-noise (SNR). As is clearly stated in [73], this criteria is laid out to establish detection confidence in various areas and *not* to define what a "discovery" or "confident detection" is.

This criteria were established primarily for detection confidence from one type of analysis, at the most using more than one pipeline (i.e. time-domain and frequency-domain targeted searches) to exclude bugs, as mentioned in Section 2.7.3. This thesis presents a hierarchical method for analysis and tests which can study these

criteria and see if they should be refined to prepare for an era of detection (see Chapter 6).

2.7.1 Signal detection

The signal-to-noise ratio (SNR) from a waveform $h(t)$ in data with a noise spectral density S_h is given by [49] as

$$\rho \equiv \sqrt{h|h}. \tag{2.28}$$

where we define

$$(x|y) \equiv 4\mathfrak{R} \int_0^\infty \frac{\tilde{x}(f)\tilde{y}^*(f)}{S_h(f)} df \tag{2.29}$$

where $\tilde{}$ is the Fourier transform, * is the complex conjugate and $\mathfrak{R}$ denotes the real component [49].

For models that include both a signal at f_0 and $2f_0$ such as free precession [27] the signals defined by Equations 2.21 - 2.24 for $h_1(t)$ and $h_2(t)$ the SNR can be rewritten to a high accuracy as

$$\rho \cong \sqrt{\rho_1^2 + \rho_2^2}, \tag{2.30}$$

where ρ_1 and ρ_2 are representative SNRs for the two frequency components of the signal. These are given by

$$\rho_1 \equiv \sqrt{(h_1|h_1)} \cong \left\{ \frac{2}{S_h(f_0)} \int_{-T_0/2}^{T_0/2} [h_1(t)]^2 dt \right\}^{1/2}, \tag{2.31}$$

$$\rho_2 \equiv \sqrt{(h_2|h_2)} \cong \left\{ \frac{2}{S_h(2f_0)} \int_{-T_0/2}^{T_0/2} [h_2(t)]^2 dt \right\}^{1/2}. \tag{2.32}$$

The value T_0 represents the observation time and for times longer than a few days, T_0 dominates the SNR values by $\sim \sqrt{T_0}$ [49]. For shorter timescales, the noise is not averaged out and so dominates the SNR, decreasing the value.

Since the parameters in $h(t)$ average over large observing times compared to the

frequency of the signal, the SNR can be simplified to resemble the classic radiometer equation, given in [38],

$$\rho = \sqrt{h|h} \propto \frac{h_0}{\sqrt{S_n}}\sqrt{T_{\text{obs}}\mathcal{N}} \tag{2.33}$$

where $\mathcal{N}$ is the number of detectors. Equation 2.33 clearly shows that the SNR can be improved by increasing the number of detectors, the observation time or reducing the noise. This will be further analysed in Chapter 3.

2.7.2 Excluding environmental and instrumentation noise as false signals

Equation 2.33 also shows that the SNR can be improved by reducing the noise in the data. This noise comes from the sources mentioned previously in Section 1.2. This noise can also potentially yield false signals. As described in the paper shown in [73], the group established the criterion that no instrumental artifact should significantly contribute to the calculated SNR. Environmental backgrounds are a rich potential source of sinusoidal backgrounds, including violin modes in the suspensions and harmonics of mains electricity coupled either through motor vibrations or RF interference. These background sinusoids may be mistaken for signals or interfere with continuous wave searches in certain bands, such as the 380Hz violin mode forest of the LIGO interferometers. Reduction of the contribution of these backgrounds to the strain signal is the job of the LIGO laboratory commissioning and operating the instruments, with tools to establish the contribution of these environmental backgrounds including seismometers, accelerometers, magnetometers, field coils and auxilliary channels of the interferometers themselves [73].

This initial check is the primary way to discard a potential candidate, but to fully exclude the likelihood of a fake signal, further investigation to the specific electronics is necessary. Due to the frequency evolution of a non-glitching neutron star, over a

long period of time this artifact would likely disappear.

A multi-tier hierarchical search would not be able to significantly improve this issue, as the artifact shows up in the original data.

2.7.3 Using multiple pipelines to exclude unexpected bugs

To address possible, unexpected spurious signals which could affect the SNR of a real signal or create a spurious signal, multiple pipelines can be used. This would help to eliminate or improve the bug. In the past, the continuous wave group used both the multiple template, frequency–domain algorithm described in Section 2.5.2 and the targeted time-domain algorithm from Section 2.5.3 ran independent searches to verify results on the search for signals from the Crab pulsar [10].

Using multiple types of algorithms to search for and possibly detect a signal is crucial to verifying a possible detection. To improve this, the hierarchical method described in this thesis which uses a series of refining searches can naturally eliminate these spurious events. This improvement to the criteria will be investigated thoroughly by using the software injection challenge discussed in Chapter 7.

2.7.4 Self consistency

With many possible models and templates for continuous gravitational wave signals, consistency and self-verification of the signal is required. This can be determined by analysing the existence of the signal in different detectors individually as well as combined. In [73], the CW group outlines specific requirements with regards to self-consistency:

- The combined SNR of interferometers should be higher than for any single interferometer for the most likely parameters. For potential signals, software

injections will be made of the signal amplitude of a similar noise. This SNR increase must be higher than expected for the lowest 5% of software injections.

- The 95% confidence bands for the frequency and first frequency derivative as well as right ascension and declination must overlap for interferometers with a SNR > 3.
- The SNR time dependency must be *reasonably* consistent with the signal model among the interferometers.
- The combined-interferometer time dependency of the SNR should be consistent with the signal model.

While it would be ideal for a signal to appear in all operating interferometers, it is possible only one detector will detect the signal. In this case, a high detection confidence may still be established, as long as the signal model is compatible with the known sensitivities of all the detectors. The hierarchical search method can also be used to increase the confidence of a signal if it is only detected in one interferometer.

Additionally, if there is a candidate flagged in one science run, there is a possibility for further confirmation in future science runs with better statistical precision due to the continuous nature of these signals. Conversely, if a signal is detected and seems to be confirmed, but then disappears in subsequent searches, this is a reason to distrust it as a continuous gravitational wave. This behaviour is a benefit to searching for continuous signals as opposed to single, short-duration events.

Finally, the signal should be astrophysically self-consistent, with observed $\dot{f}_{\mathrm{gw}}$ being as least as large as implied from f_{gw} and h where a source distance is known from electromagnetic observations. In addition, if the distance is not known, one must check that the signal strength inferred from the event in the data is astrophysically likely with the observed f_{gw}, $\dot{f}_{\mathrm{gw}}$ and h. This should not be the only criterion to

disregard a strong non-terrestrial signal as our understanding of neutron star sources is incomplete. In addition, we should not rule out the possibility of the existence of unknown classes of continuous wave sources.

The hierarchical method described in Section 2.5.4 can improve detection confidence by naturally using different types of search methods (all-sky, targeted, frequency-domain, time-domain, etc). The ability to confirm candidates as detections will be increased with this method. The mock-data challenge in Chapters 6 and 7 will help measure the accuracy of the various existing continuous wave pipelines in determining event parameters.

3

Exploring sensitivity dependence on location of detectors

When moving into an era where detections of gravitational waves are likely, improving the performance of the detector network is crucial. As the collaboration prepares for Advanced LIGO (aLIGO), additional detectors for the LIGO network are considered. This section investigates the impact of a detector in a new, spacially separated site on sensitivity of continuous wave searches.

Initially, the new LIGO detector was proposed to be in Australia. This detector was initially referred to as "LIGO South", but due to funding issues, that has been changed to a new site in India, called IndIGO.[1] The proposed IndIGO detector will replace the secondary American detector at Hanford. It will utilise the same technology as the American Advanced LIGO detectors and be a Michelson interferometer with 4 km arm lengths. Having a detector significantly spacially separated increases the baseline of the network, known to improve the sensitivity and sky location of coalescing binaries. While a final site location has not been decided, a seismically quiet site such as the Deccan Plateau in central India is likely [46]. The location of

[1] `http://www.gw-indigo.org`

the IndIGO detector is also needed for the simulation, but since this is currently unknown, an estimated position of 16.0° N, 78.0° E was used, approximately the middle of the Deccan Plateau. The current proposed timeline for introducing IndIGO to the Advanced Detector network has individual science runs beginning in 2019 with full inclusion in the network to begin approximately in 2020 [46].

This investigation utilises the targeted search described in Section 2.4 to analyse the parameter sensitivity difference between the American aLIGO network (two Hanford detectors and one Livingston detector) and a detector network which replaces the second Hanford detector with IndIGO. In this chapter, the American aLIGO network will be referred to as HHL and the IndIGO network is referred to as HLI. To analyse the difference between the networks we compare the widths of the posterior parameter curves, which indicates the level of sensitivity. We will not be looking at the effect of detector location on reconstructed sky location parameters as the mechanisms to do this are still being developed by the continuous wave group. This chapter looks solely at the dependence of recovering the gravitational wave parameters on detector location.

This analysis begins with a simulated waveform whose parameters are randomly chosen as shown in Table 3.1. the parameters are fed in with an estimate of the noise as initial data for the Markov Chain analysis, which is run on the data containing the injected waveform, to test whether the maximum likelihood procedure yields posterior estimates on the parameters matching the injection values. The difference in the search (as each detector network MCMC begins with the same initial data) is in the calculation of the antenna patterns having an effect on the sensitivity and likelihood of parameter recovery.

The purpose of this search is to analyse the width of these posterior parameter curves as that is an indicator of the level of certainty in the recovery. The width of the four posterior distributions (one for each h_0, $\cos\iota$, ϕ_0 and Ψ) are compared

by taking the ratio on each detector network. This method is performed 100 times and the ratios are examined to determine if one detector network is favoured over another.

Parameters	Distribution
ϕ_0	$[0, 2\pi)$ random, uniform
Ψ	$[-\pi/4, \pi/4)$ random, uniform
$\cos\iota$	0
h_0	Calculated using parameters
$f_{\rm gw}$	150 Hz
SNR	100
α and δ	Random, uniform
$T_{\rm obs}$	365 days

Table 3.1 – The sample space of gravitational wave parameters from which the distribution of pulsars was chosen for IndIGO network analysis.

Having $\cos\iota = 0$ means the signal is linearly polarised, which provides a worst-case scenario for sensitivity as the arms must be optimally aligned. Since the orientation, γ, of the IndIGO detector is unknown and the signals are linearly polarised we will use two values for γ which are $\pi/8$ radians apart. In the simulation, these values are chosen as $\gamma = 116.5°$ and $\gamma = 139.0°$. For the simulation, the two orientations for the detectors will be called I1 and I2, respectively. Therefore, the three networks used in this chapter are referred to as HHL, HLI1 and HLI2.

If the detector networks have comparable sensitivity, the ratio of the widths of the posterior curves should be approximately 1. Before we compare the networks, we want to run some checks to make sure that this method gives reasonable results. The best way to do this is to run the MCMC parameter code twice on the same detector network and take the resulting ratio. If we run this 100 times and look at the distribution of ratios of the posterior curve widths, they should all be tightly centred on 1. The results from this test are given in Section 3.1.

Once we confirm that this is a valid method for comparing sensitivity using the targeted search posterior distributions, we will compare the performance of HHL to HLI1 and HLI2. If the resulting distribution of ratios are greater than one, this

means that the HLI detectors have better sensitivity and vice versa.

3.1 Testing the validity of the simulation

The first step is to confirm that performing the simulation is robust on the same detector system by taking the ratio of results on the same detector network. We will calculate 100 ratios of recovered parameters on the same network.

For the advanced detector network solely in the United States, the mean and standard deviation ratios of 100 MCMC runs are shown in Table 3.2 and the histograms of the results are shown in Figure 3.1.

Parameter	Mean (μ_{HHL})	Standard Deviation (σ_{HHL})
h_0	1.014	0.094
ϕ_0	0.996	0.069
$\cos\iota$	1.010	0.078
Ψ	1.006	0.058

Table 3.2 – This table shows the mean and standard deviation of the MCMC with the aLIGO North detector network

As can be seen from the results, there is a tight distribution around the value of 1 for all parameters. This shows that the MCMC system is robust and is a valid way of comparing the performance of networks.

3.2 Comparing detector network locations on the sensitivity of continuous wave targeted searches

First we look at the detector network HLI1. The widths of the parameter posterior distributions from HHL are divided by the widths from HLI1 to get the ratio. These results are shown in Figure 3.2 and the statistics are given in Table **??**.

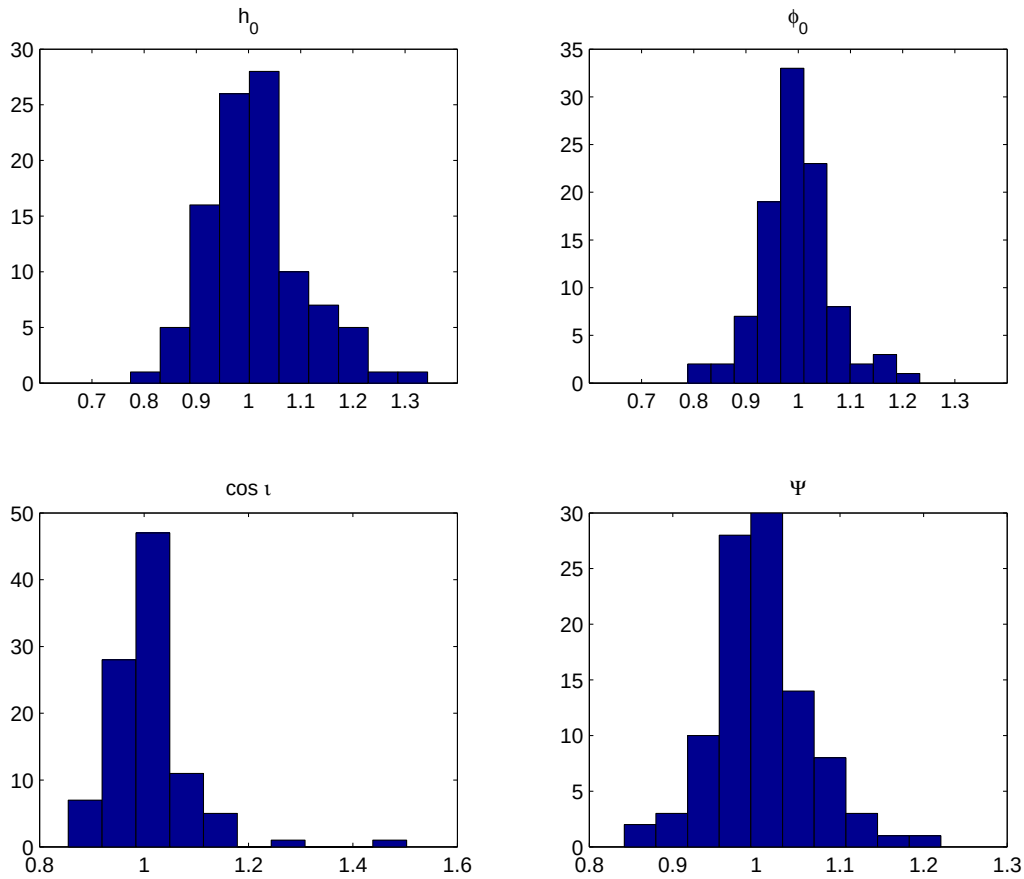

Figure 3.1 – The performance of the MCMC tests over 100 comparisons in the detector network HHL. These are the ratios of the posterior widths for each parameter on the same detector network. As expected, these ratios are tightly centred around 1.

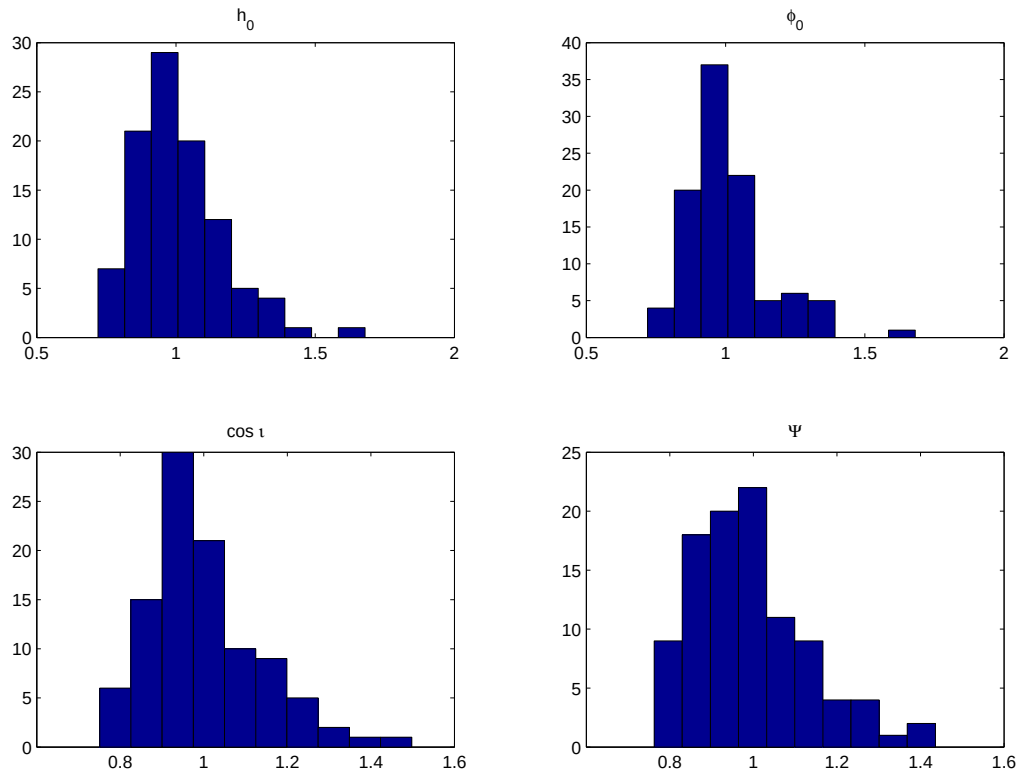

Figure 3.2 – The distribution of 100 posterior width ratios for each parameter from HHL to HLI1. The HLI1 orientation is $\gamma = 116.5°$.

Parameter	Mean (μ_1)	Standard Deviation (σ_1)
h_0	1.01	0.16
ϕ_0	1.01	0.14
$\cos\iota$	0.998	0.139
Ψ	0.992	0.139

Table 3.3 – This table shows the mean and standard deviation of the MCMC ratio between HHL and HLI1.

Next, we examine the next possible orientation for HLI2 where $\gamma = 139.0$ and compare HHL to this detector network. These results are shown in Figure 3.3 and the statistics are shown in Table **??**.

Parameter	Mean (μ_1)	Standard Deviation (σ_2)
h_0	1.005	0.153
ϕ_0	0.999	0.145
$\cos\iota$	0.998	0.145
Ψ	0.984	0.148

Table 3.4 – This table shows the mean and standard deviation of the MCMC ratio between HHL and HLI2.

Both of these distributions are still centred on 1 to a high sensitivity, but with a greater width in the distribution. This shows that the addition of a spacially separated detector to the aLIGO network does not have a significant impact on the ability to recover gravitational wave parameters from continuous wave sources using the MCMC method.

3.3 The results of sensitivity analysis

As is seen in Section 3.2, when we compare the simulation results from different detector networks, the spread is slightly wider than the self-consistent checks, showing that the position of the detectors does make a difference on the results. However, these ratios of posterior widths with different detector networks still centre on 1, showing that there is no preference either way for a detector network more widely distributed on the Earth.

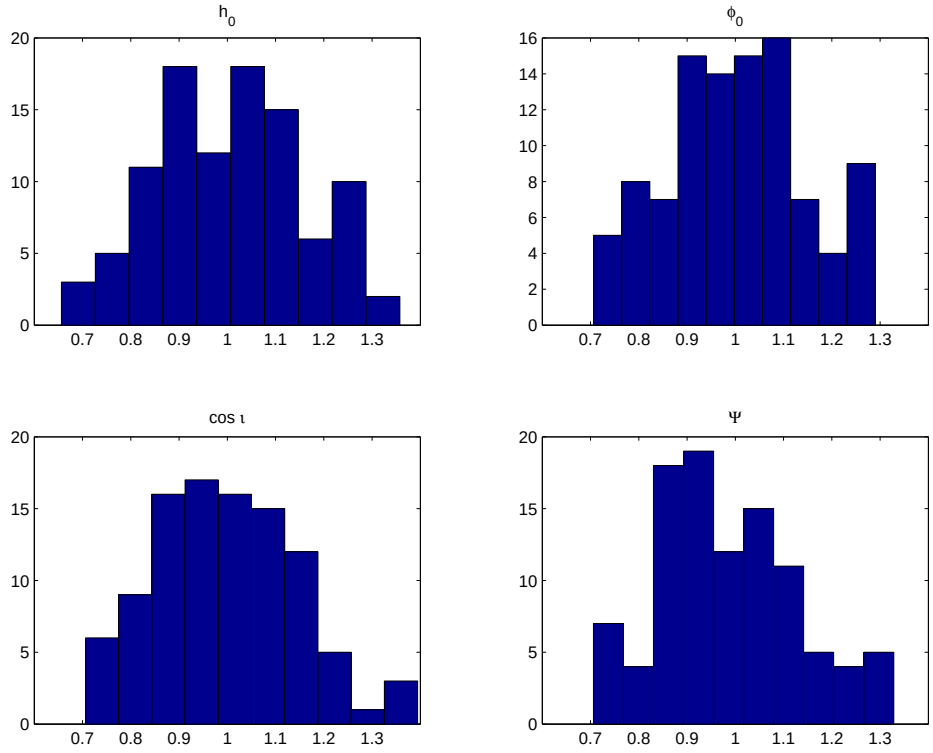

Figure 3.3 – The distribution of 100 ratios of each posterior width of HHL to HLI2. The HLI2 network has an orientation of $\gamma = 139.0°$.

This result is unsurprising for gravitational wave parameters. There may be an effect in the future for reconstructed sky location, but this has not been developed as of writing this. However, it is of scientific value to verify that this is true because of the nonlinearity and complexity of the Markov Chain procedure. Now that the effect of the location of detector networks for Advanced LIGO is addressed, this thesis will investigate the specific searches of the continuous wave group and each step of the hierarchical method described in Section 2.5.4.

4

The effects of time variation in the source to detector distance on all-sky searches

Understanding the distribution of neutron stars in the Galaxy is essential when approaching an era of advanced detectors, especially for developing mock data to test algorithms. With an accurate model of the population, we are able to tune our searches to optimise the likelihood of detection. the convergence of parameter reconstruction algorithms such as template searches and Markov chains on the underlying physical parameters can be affected by drift in these parameters with time.

The all-sky searches (such as Einstein@Home[1]) run a *blind* method of searching, where there is no prior knowledge about neutron star position or frequencies. To run this type of search, it is too computationally expensive to explore the full possible parameter space. A way to maintain sensitivity and keep computing costs to a reasonable level, a hierarchical method can be used. This is the system that is implemented by the Einstein@Home search and will be discussed here.

[1] `http://einstein.phys.uwm.edu`

This hierarchical method starts with an initial wide-parameter search with a short observation time (the highest computing cost factor) which makes a low parameter space resolution [69]. A low threshold is used to identify potential signals. However, lowering the threshold means that there is a higher number of candidates, so the next step takes all these candidates with longer observation times and a longer threshold to narrow the candidates. This process continues until there is a strong confidence in the remaining candidates.

This system means that the number of iterations, the observing length of each one as well as the threshold for each iteration are all free parameters. These all need to be optimised to obtain the best sensitivity per computing cost [69].

In this chapter, I will focus on the effects that neutron star motions have on the blind all-sky search, Einstein@Home (E@H) which is a public-distributed computing project. They utilise the distributed computing platform BOINC [2] which was developed for SETI@Home. This platform allows signed-up users to offer their computing time to each analyse a small parameter space $\Delta\boldsymbol{\lambda}$ where $\boldsymbol{\lambda}$ are the position and spin parameters. Once this is processed, the result is sent back to the central server and another work unit is requested. This process will ultimately yield an extremely sensitive search for unknown neutron stars.

4.1 Frequency shifts due to parallax and proper motion

One important factor to take into account for all of the continuous gravitational wave searches is the apparent motion of neutron stars on the sky, either due to their own motion (proper motion) or the movement of the Earth around the Sun (parallax). The all-sky search, Einstein@Home, searches the parameter space of gravitational

[2] `http://boinc.berkeley.edu`

wave frequency $f_{\rm gw}$ and $\dot{f}_{\rm gw}$. Einstein@Home is a template search which works by dividing the parameter space into boxes of some small dimension. If motion of either the source or the detector causes the signal parameters to move between boxes over the course of the search, sensitivity assigned to the signal is reduced.

This space is broken up into two sections by Einstein@Home of less than and greater than 400 Hz. For the most recent search in S5 [12], the ranges searched are shown in Figure 4.1. The break at 400 Hz is due to the increasing computational cost as the frequency increases. There is also a small amount of parameter space which corresponds to the small population of neutron stars with a positive $\dot{f}_{\rm gw}$.

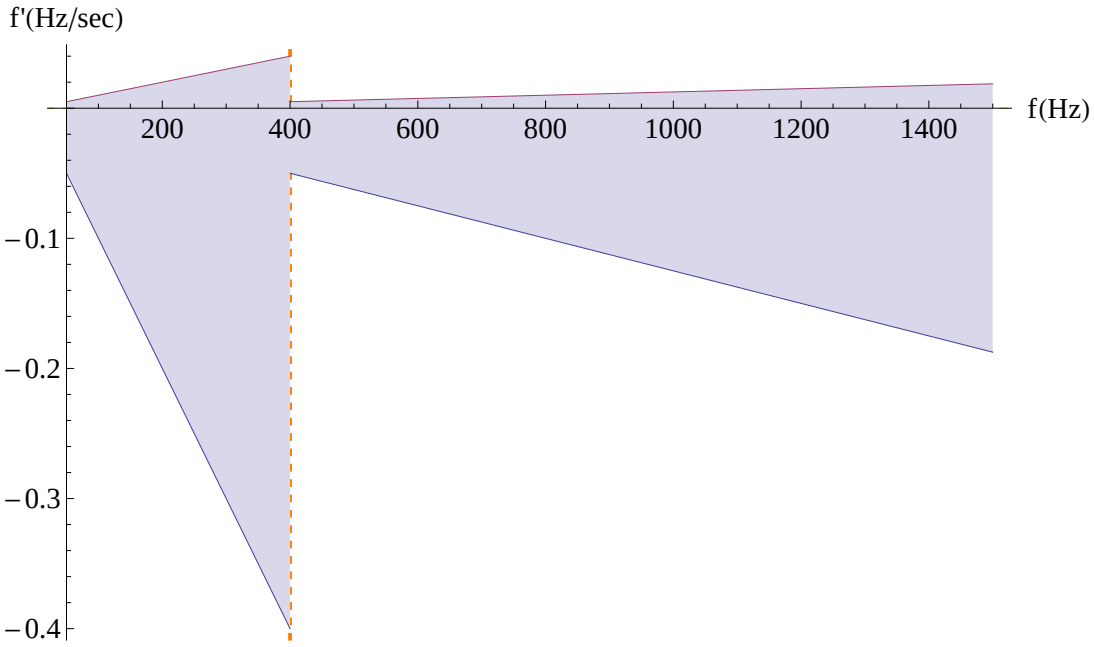

Figure 4.1 – The search limits of Einstein@Home as given in [12]. The shaded region designates the search parameters. The break at 400 Hz is to primarily account for the increasing computing time at high frequencies.

Einstein@Home breaks up the parameter space into blocks of f and $\dot{f}$. For f below 400 Hz, the blocks are the size $\Delta f = 1.78\,\text{mHz}$ and $\Delta\dot{f} = 3.18 \times 10^{-10}\,\text{Hz s}^{-1}$. For f greater than 400 Hz, $\Delta f = 2.9\,\text{mHz}$ and $\Delta\dot{f} = 5.19 \times 10^{-10}\,\text{Hz s}^{-1}$ [12]. These limits are given in Table 4.1.

Again, these are chosen based on the a trade-off for a computational cost versus detection. These blocks are distributed amongst the Einstein@Home users to search

	$f < 400\,\mathrm{Hz}$	$f > 400\,\mathrm{Hz}$
Δf	1.78 Hz	2.9 Hz
$\Delta \dot{f}$	$3.18 \times 10^{-10}\,\mathrm{Hz\ s^{-1}}$	$5.19 \times 10^{-10}\,\mathrm{Hz\ s^{-1}}$

Table 4.1 – Frequency bins for the S5 Einstein@Home search as given in [12].

for a signal. If a signal is divided between multiple blocks due to a frequency shift, the sensitivity will go down for each user and will not pass as a viable candidate. In this chapter we study two modulations in the length of the line of sight between source and detector, the first due to orbital motion of the Earth about the sun, and the second due to physical motion of the source with respect to fixed, non-comoving coordinates.

4.1.1 Frequency shift due to parallax angle

The Einstein@Home search accounts for a Doppler shift in frequency due to the Earth's annular orbit (parallax), but it assumes that the gravitational wave "rays" arrive at Earth in parallel, whereas they actually arrive at a slight angle. This section explores the affect this assumption has on the search and if accounting for it would affect the ability to make a detection. The different assumptions are shown in Figure 4.2 where the red line, $d(t)$, depicts the path that Einstein@Home assumes (note that it does take account of the shift in distance over time due to Earth's motion) and the blue line, $a(t)$, is where we account for the small angle θ. We also account for the line of sight angle with respect to the orientation of the solar system, γ.

The goal of this investigation is to determine if assuming the gravitational waves arrive in parallel has an effect on the frequency calculation. Essentially, we need to calculate the difference in arrival frequency to see if the signal shifts out of the Einstein@Home frequency "bins".

We need to calculate the equation for $a(t)$ using trigonometric identities and rules

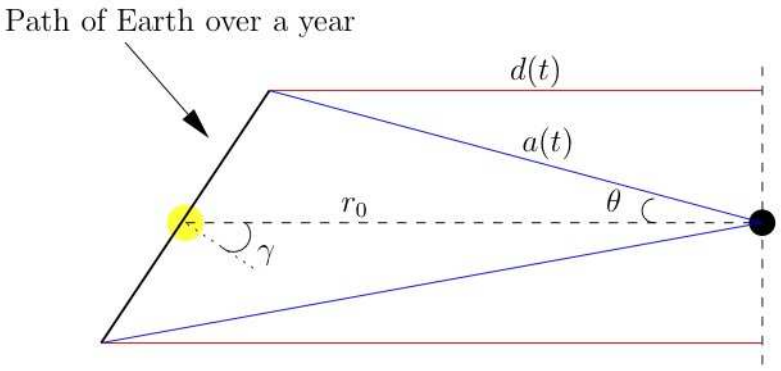

Figure 4.2 – This represents the assumptions made by Einstein@Home, $d(t)$, and the calculation in this section, $a(t)$, where the small angle θ is accounted for.

and assume that the Earth orbits the Sun at an angular frequency of ω. This gives the equation

$$a(t,\gamma) = \sqrt{r_0^2 + 2\,r\,r_0\,\sin\gamma\,\sin t\omega + r^2\,\sin^2 t\omega} \tag{4.1}$$

which does not use θ. We then translate this to frequency by first calculating the phase of the gravitational wave signal,

$$\phi_a(t,\gamma) = 2\pi\,f_0\left(t - \frac{a(t,\gamma)}{c}\right) \tag{4.2}$$

where f_0 is the initial gravitational wave frequency and c is the speed of light. For this practical demonstration, we will use $f_0 = 1500\,\mathrm{Hz}$ as the higher frequencies are shifted more and have a greater chance of shifting out of the Einstein@Home parameter bins.

The apparent frequency can be derived from $\phi(t,\gamma)$ using the equation

$$f_a(t,\gamma) = \frac{\dot{\phi_a}(t,\gamma)}{2\pi} \tag{4.3}$$

where $\dot{\phi_a}(t,\gamma)$ is the derivative with respect to time.

We then repeat this process for the distance that Einstein@Home uses, $d(t,\gamma)$, to

calculate $f_d(t, \gamma)$ and see if there is a significant difference with $f_a(t, \gamma)$.

As the resulting calculation depends on the inclination, γ and on the starting distance, r_0, we performed sample calculations to get an idea of the possible effects. We fixed $\gamma = Pi/4$ radians and varied r_0 to see at what distance we would be concerned about a search's sensitivity. This representative value is about $r_0 = 7 \times 10^{-5}$ pc, which is approximately 15 AU, well within our Solar System and would not occur given our current understanding of neutron star populations. This sample calculation is illustrated in Figures 4.3 and 4.4.

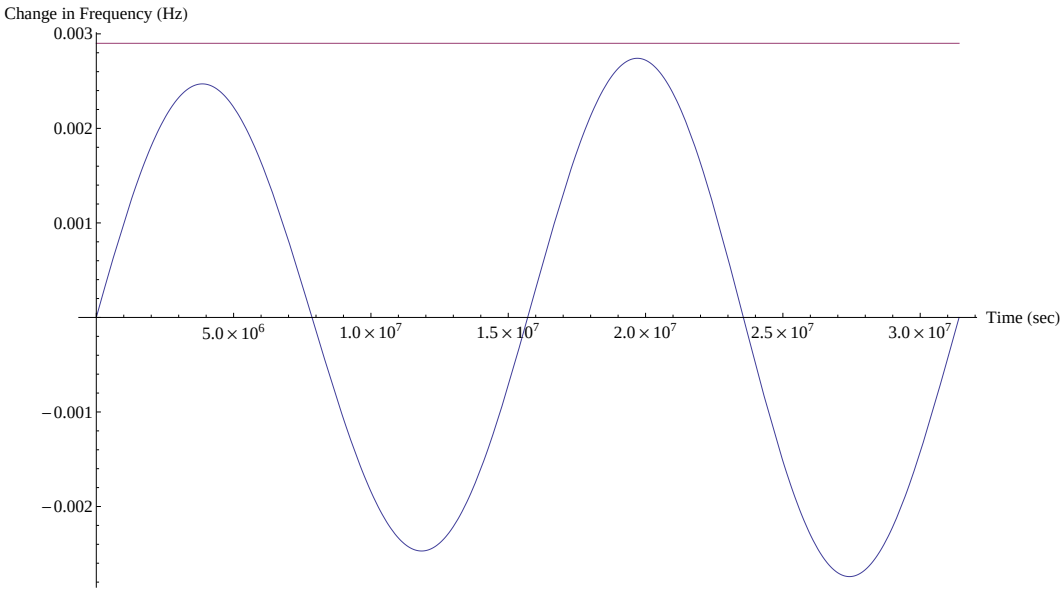

Figure 4.3 – The difference in frequency calculation between assuming the gravitational waves arrive parallel to the Earth versus accounting for the small angle of approach. The source is at an inclination angle of $\gamma = \pi/4$ and the distance is 7×10^{-5} pc. The horizontal line is the barrier where the Einstein@Home search would be affected.

4.1.2 Doppler shift due to neutron star velocities

Proper motion refers to the real (rather than apparent) transverse movement of stars relative to the centre of the solar system as they travel through the galaxy. Typically it is measured in units of milliarcseconds per years (mas/yr) and can be quantified for most of the nearby pulsars. Figure 4.5 shows the distribution of proper motions

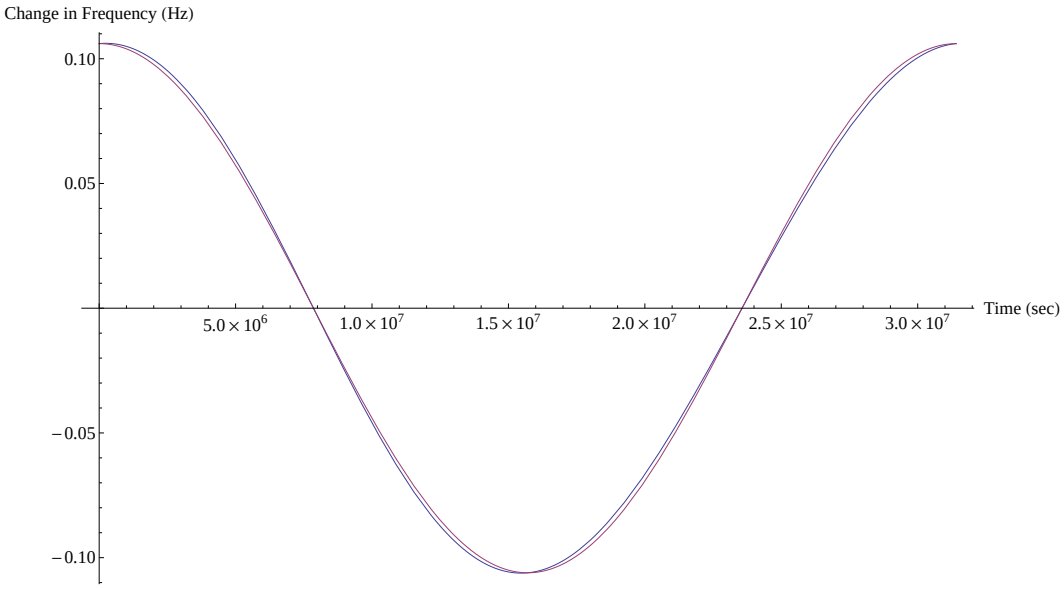

Figure 4.4 – The change in frequency due to parallax. The red line is the parallax calculated for Einstein@Home and the blue line is when you account for the small angle shift. This is calculated at a distance of 7×10^{-5} pc where there starts to be a significant difference.

as given in the ATNF database [58].

The proper motion of neutron stars will have an effect on all-sky gravitational wave searches, in a similar manner as described in Section 4.1.1, except this time it is a real motion and not an apparent one. If the neutron star is sufficiently close to Earth, or is moving with a high velocity, it is possible that the $\dot{f}$ parameter will be shifted due to transverse doppler shift out of the all-sky search windows. As mentioned in Section 4.1.1, the Einstein@Home search window in S5 is $\Delta\dot{f} = 3 \times 10^{-10}\,\mathrm{Hz\,s^{-1}}$. This section analyses the possibility of this effect occurring due to current understanding of neutron star populations.

Hobbs *et al.* presented a study of 233 known pulsars and their proper motion, the largest observable proper motion is for pulsar PSR B2011+38 with a velocity of 1284 $\mathrm{km\,s^{-1}}$ in the right ascension and 996 $\mathrm{km\,s^{-1}}$ in declination [43]. A recent paper by Tomsick *et. al*, 2012 estimates a transverse velocity of the object IGR J11014-6103 to be about 2 400 - 2 900 $\mathrm{m\,s^{-1}}$ [79]. A representative upper limit value of 1 000 $\mathrm{km\,s^{-1}}$ was used in the simulations for the velocity to represent an extreme,

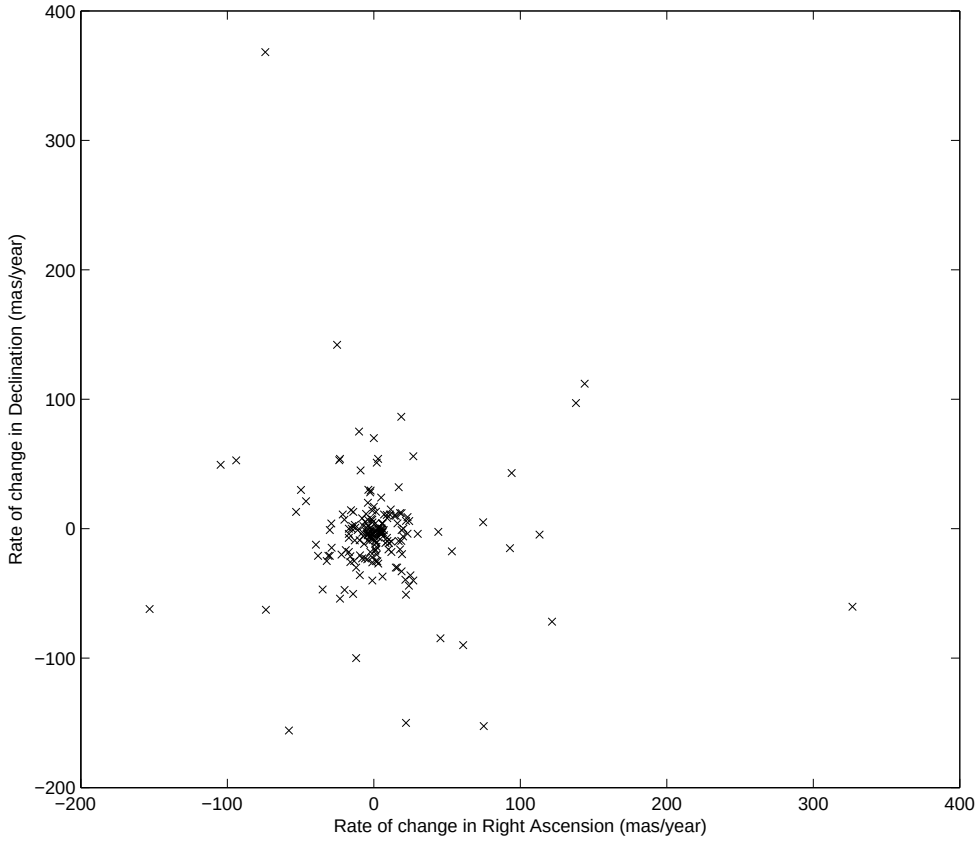

Figure 4.5 – Known proper motion distributions of pulsars as given in the ATNF database.

yet realistic situation.

Following a similar process used for Section 4.1.1, we can calculate $\Delta\dot{f}$ over an extended period of time to determine at which point the parameters become so extreme they move out of a single Einstein@Home parameter template during an observation. This study was done by both varying the initial distance as well as varying the velocity of the neutron star to the most extreme value.

Though the equations for calculating the effect of proper motion are similar to those for parallax, there are more variables to analyse, such as varying the sky position, distance and velocity. To explore this, it is useful to picture the scenario of proper motion as seen in Figure 4.6. For this analysis, we are assuming that the velocity

of the star remains constant and we are neglecting the effects of the Earth's orbit around the Sun.

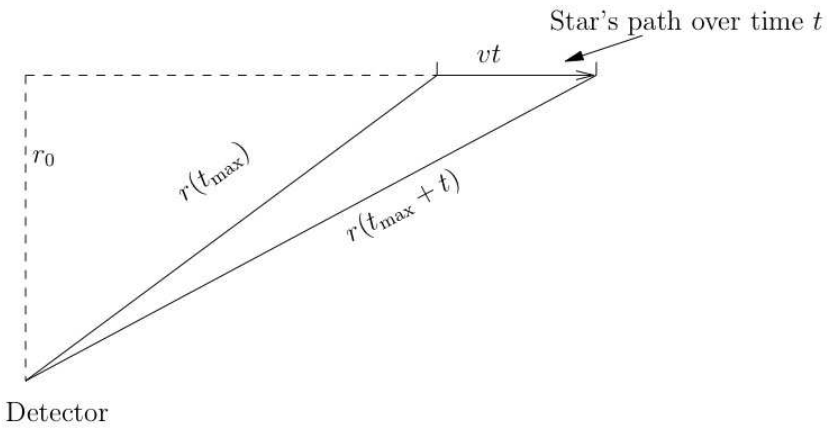

Figure 4.6 – This diagram shows the vectors necessary for proper motion calculations with consideration given to a point at $t_{\max}$ where $\ddot{f}$ is at a maximum

If the pulsar is observed over a period of time, there will be a distance, $r(t_{\max})$ where the change in r is at a maximum. One approach is to calculate the maximum $\Delta\dot{f}(t)$ at a r_0 of 1 pc. To calculate $\Delta\dot{f}(t)$ we start with

$$r(t) = \sqrt{r_0^2 + v^2(t_{\max}+t)^2} - \sqrt{r_0^2 + v^2 t_{\max}^2}. \tag{4.4}$$

from Figure 4.6 and derive $f(t)$ using Equations **??** - **??**. We then calculate

$$\Delta\dot{f} = \frac{f_0 v^2}{c}\left[\frac{1}{r_0} + \frac{t^2 v^4}{(r_0^2 + t^2 v^2)^{3/2}} - \frac{1}{\sqrt{r_0^2 + t^2 v^2}}\right]. \tag{4.5}$$

This equation is plotted in 4.7 for the closest approach $r_0 = 1$ pc and a velocity of $v = 1000$ km s^{-1}. At the closest approach and a year observation, $\Delta\dot{f} = 1.5 \times 10^{-13}$ Hz s^{-1} which is well within the bounds of the Einstein@Home parameter bins. Starting with $r_0 = 1$ pc, the maximum $\Delta\dot{f}$ occurs at 1.5×10^{10} s.

Another exploration of proper motion is to study extreme velocities of neutron stars Equation 4.5 is highly dependent on velocity. As previously mentioned, the largest known proper motion is 1000 km s^{-1}.

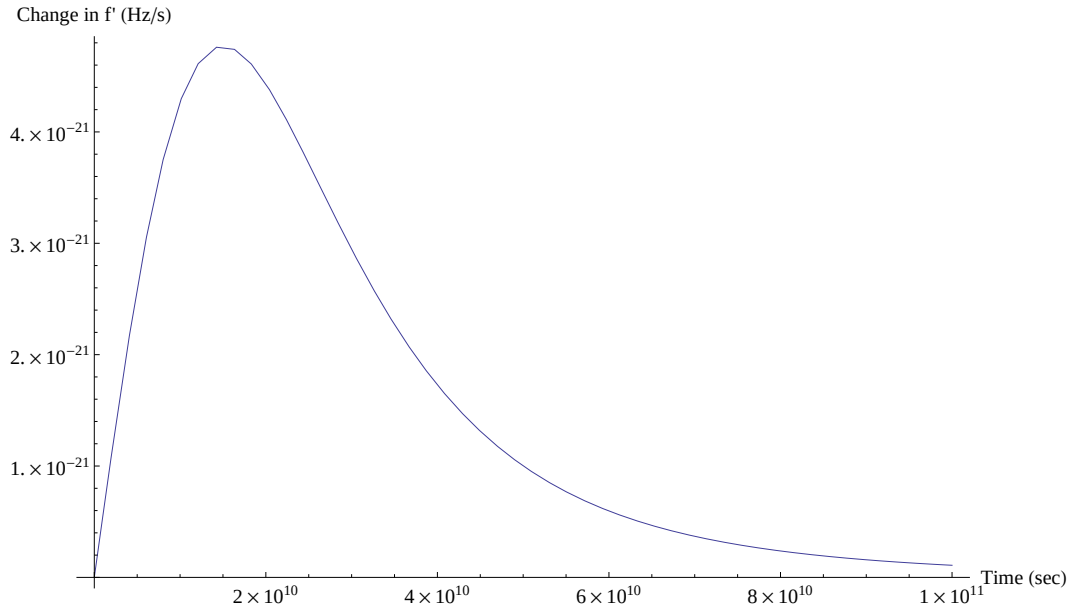

Figure 4.7 – The second derivative of frequency over time of a pulsar traveling at 1000 km s^{-1} from a distance of 1 pc

The plot showing $\Delta\dot{f}$ with respect to velocity is shown in Figure 4.8 with the Einstein@Home bin size of 5.9×10^{-10} shown as the red dashed line. This plot assumes a closest approach of $r_0 = 1\,\mathrm{pc}$ and an observation time of $T_{\mathrm{obs}} = 1\,\mathrm{yr}$. The intersection, where the velocity would force the signal out of the Einstein@Home parameter bin occurs when the neutron star is moving at $v \approx 3.83 \times 10^7$ m s^{-1}.

The value of $3.83 \times 10^7\,\mathrm{m\ s^{-1}}$ corresponds to an angular velocity of $1.91^\circ\,\mathrm{yr}^{-1}$ at a distance of 1 pc. At the distance of the closest known neutron star of about 150 pc [50] this velocity would be a proper motion of $45.8\,\mathrm{arcsec\,yr}^{-1}$ which at our current understanding of population distributions is infeasible with Barnard's star having the highest proper motion of $10.3\,\mathrm{as\,yr}^{-1}$ at a distance of only 6 light years away [19] [20].

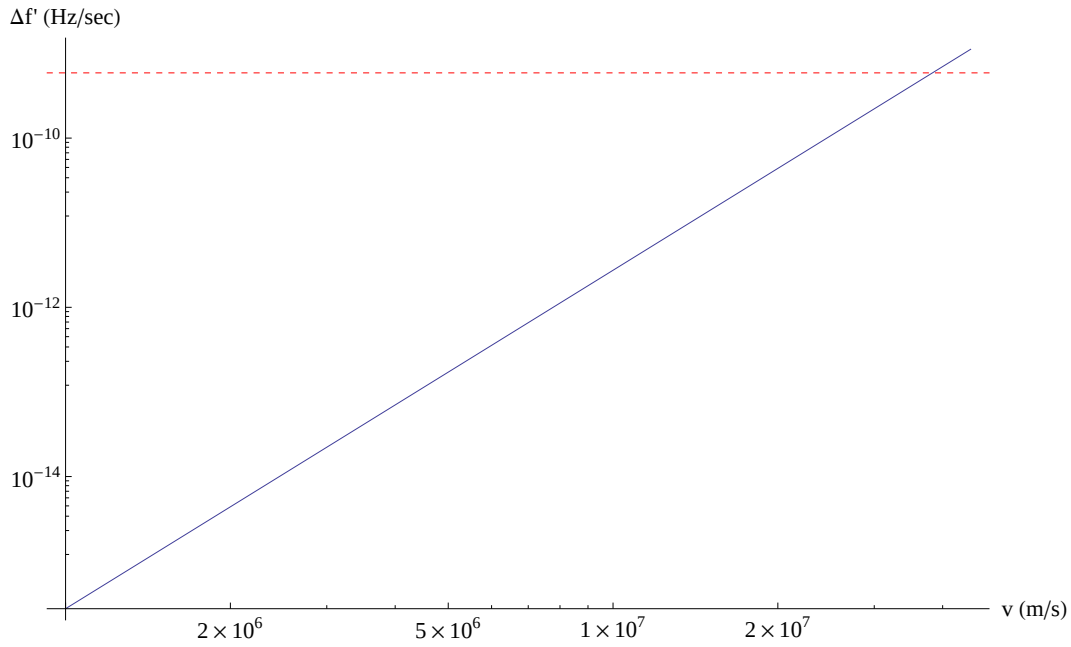

Figure 4.8 – The change in $\dot{f}$ over a year observation dependent on velocity. The red dashed line shows the Einstein@Home limit

4.2 Analysis of the effects of distances and velocities of neutron stars on all-sky searches

In this section, I analysed the effect that motion of neutron stars has on the sensitivity of the all-sky search, Einstein@Home and the likelihood of making a detection. A blind all-sky search is most likely to detect a non-axisymmetric neutron star close to Earth, which means it is most likely to have a high proper motion and parallax. This could potentially move the signal out of the parameter bin during the observation time.

For the effect that parallax (apparent motion) has on blind gravitational wave searches, I discovered that in order to go outside of the Einstein@Home bins, a neutron star would need to be at 7×10^{-5} pc. This is within our Solar System and given our current understanding of distributions of neutron stars, it is completely non-astrophysical. This demonstrates that it is unlikely that the small angle when calculating parallax is something we need to account for in the present Ein-

stein@Home search.

The most important consideration for the Einstein@Home blind search is the possibility of high transverse velocities which result in a high doppler shift. This search aimed to find out the extreme motion on the sky which would cause an unknown neutron star to shift out of the search bins. This study showed that at 1 pc and an approximate extreme, but known, value for velocity of 1000 km s^{-1} and observation time of 1 year, the change in $\dot{f}$ is $\Delta\dot{f} = 1.5 \times 10^{-13}\,\mathrm{Hz\,s^{-1}}$ which is approximately 3 orders of magnitude within the limits for Einstein@Home.

I also investigated the extreme velocity necessary to exceed the Einstein@Home limits. I found that this velocity is approximately $v \approx 3.83 \times 10^{7}\,\mathrm{m\,s^{-1}}$. For the closest known neutron star of $r_0 \sim 100\,\mathrm{pc}$, this corresponds to a proper motion of 45.8 arcsec yr^{-1}. This value is about 4-5 times higher than the highest proper motion observed of 10.3 as yr^{-1} from Barnard's Star which is only ~ 2 pc, a factor of 50 closer than the closest known neutron star.

This investigation shows that it is astrophysically impossible to have an object close enough for parallax or proper motion to make an impact on a reasonable Einstein@Home search. In addition, it provides a useful constraint on the scope of simulated signals we need to generate to test the CW searches. Specifically, we do not need to simulate the contributions of parallax and proper motion to our simulated signals generated in Chapter 6.

5

Refining signal detections with multiple templates: the narrow-band search

This chapter describes the middle step in the hierarchical detection method, both the theory and results from two example, stand-alone searches. This method was previously referred to as the "wide-parameter" search in previous continuous wave (CW) search literature. The recent gravitational wave emission upper limit from the Crab Pulsar used this search method in parallel with a targeted, Bayesian search [10].

This search is a small-area, directed search where the location and frequencies are approximately known. It examines multiple templates containing the possible parameters for a likely signal. The search uses a frequentist method of maximum likelihoods to determine candidates and parameters, as described in Section 5.1. By varying the parameters around a small region, we can account for unknown values in the gravitational wave emission from the neutron star. In this chapter, I apply the narrow-band technique to the Crab Pulsar parameters again for the recent science

run, S6, as well as applying the search to a continuous wave hardware injection in S6 data.

5.1 Frequentist search and the $\mathcal{F}$-Statistic

The frequentist approach in statistics interprets the probability $P(X)$ of an event, X, occurring as the fraction, or frequency, of events in an infinite number of trials with statistically identical conditions. For detecting gravitational wave signals in a set of data using this method, we need to define a statistic and hypotheses necessary for declaring a detection. In CW searches, the $\mathcal{F}$-statistic was derived to optimise searches in the work done by Jaranowski, Królak and Schutz [49]. We will also define probability thresholds based on the recent work by Karl Wette [86]. The hypotheses necessary for this search are the null hypothesis, H_0, where there is no signal in the data and the alternative hypothesis H_1 where there exists a signal, h, in the data. Here, we define a test statistic and assess it's performance.

In general, to statistically determine which hypothesis is correct for a set of data, $x(t)$, we need to set a threshold, Λ^*, from a scalar detection statistic, $\Lambda(x)$ (in this case, the $\mathcal{F}$-statistic as defined later). The value Λ^* is defined in such a way that if $\Lambda(x) < \Lambda^*$ we will accept the null hypothesis H_0 and if $\Lambda(x) > \Lambda^*$ then the alternative hypothesis, H_1 is accepted. The probability of these events is defined as $P(\Lambda(x)|H_0)$ and $P(\Lambda(x)|H_1)$ where the notation $P(x|y)$ is read as "The probability of obtaining x given y is correct."

In reality, however, it is possible to mistakenly claim the incorrect hypothesis. These are referred to as *false alarms* and *false dismissals*. Here, we will use the notation seen in Prix, 2009 [69]. The false alarm probability, where $\Lambda > \Lambda^*$ (from here, I will

use Λ to mean $\Lambda(x)$) despite the fact that H_0 is true is defined as

$$f_{\mathrm{A}}(\Lambda^*) \equiv \int_{\Lambda^*}^{\infty} P(\Lambda|H_0)d\Lambda, \tag{5.1}$$

where the probability distribution function for H_0 is integrated to find the probability that $\Lambda > \Lambda^*$.

Similarly, the false dismissal probability, where we calculate $\Lambda < \Lambda^*$ despite the fact that H_1 is true and there is a signal h in the data is given as

$$f_{\mathrm{D}}(\Lambda^*, h) \equiv \int_{-\infty}^{\Lambda^*} P(\Lambda|H_1)d\Lambda. \tag{5.2}$$

In order to calculate the overall probability of detecting a signal which is present in the data, we define the complement of f_{D} as $\eta \equiv 1 - f_{\mathrm{D}}$ which gives the equation

$$\eta \equiv \int_{\Lambda^*}^{\infty} P(\Lambda|H_1)d\Lambda, \tag{5.3}$$

or simply the integral of the probability distribution function for a signal being present above Λ^*.

Next, we want to maximize η to find the optimal Λ for a given false alarm rate, or probability, usually 1%. The Neyman-Pearson lemma gives the likelihood ratio test as

$$\Lambda(x; h) \equiv \frac{P(x|H_1)}{P(x|H_0)}. \tag{5.4}$$

Continuous wave analysis

In continuous gravitational wave data analysis, the log likelihood function for a signal x in a set of data h is defined as follows:

$$\ln \Lambda(x; h) = (x||h) - \frac{1}{2}(h||h) \tag{5.5}$$

which is an expression for the matched-filtering amplitude where

$$(x||y) \equiv 4\mathfrak{R}\int_0^\infty \frac{\tilde{x}(f)\tilde{y}^*(f)}{S_h(f)}df, \tag{5.6}$$

and $\tilde{x}(f)$ is the Fourier transform of the signal, $\tilde{y}^*(f)$ is the Fourier transform of the complex conjugate of the data and $\mathfrak{R}$ is the real part of the complex number.

$$\tilde{x}(f) = \int_{-\infty}^{\infty} e^{2\pi i f t} x(t) dt. \tag{5.7}$$

The value S_h is the *one-sided* spectral density of the detector's noise at a specific frequency [49].

In our searches, not all the gravitational wave parameters of h are known so we maximise Equation 5.5 to define the maximum likelihood values. In this thesis, and in frequentist continuous wave searches, the maximum likelihood value is the $\mathcal{F}$-Statistic [49].

5.1.1 The $\mathcal{F}$-Statistic

The first derivation of the $\mathcal{F}$-Statistic is given in Jaranowski, Królak and Schutz [49]. Updated calculations include situations with multiple detectors and multiple sources are given in Cutler and Schutz [28]. This $\mathcal{F}$-statistic is not to be confused with the standard F-statistic or the F-distribution found in traditional statistics literature.

With the data, x, we assume the Doppler parameters $\boldsymbol{\lambda}$: sky position (α and δ) and frequencies (f, $\dot{f}$ ...), are unknown for the purposes of the narrow-band search. The four amplitude parameters $\mathcal{A}$ of the gravitational wave are also unknown. From this and using Equation 5.5, we calculate [49]

$$\ln \Lambda(x; \mathcal{A}, \boldsymbol{\lambda}) = \mathcal{A}^\mu x_\mu - \frac{1}{2}\mathcal{A}^\mu \mathcal{A}^\nu \mathcal{M}_{\mu\nu}, \tag{5.8}$$

with summation over $\mu, \nu \in [1, 4]$ and we define

$$x_\mu(\boldsymbol{\lambda}) \equiv (x||h_\mu) \quad \text{and} \quad \mathcal{M}_{\mu\nu}(\boldsymbol{\lambda}) \equiv (h_\mu||h_\nu), \tag{5.9}$$

using the scalar product defined in Equation 5.6.

We can maximise the log-likelihood factor over the gravitational wave amplitude parameters to obtain the maximum likelihood estimators $\mathcal{A}^\mu_{\mathrm{ML}}$. We then substitute these values into Equation 5.8 to give our statistic [49],

$$2\mathcal{F}(x; \boldsymbol{\lambda}) = x_\mu \mathcal{M}^{\mu\nu} x_\nu. \tag{5.10}$$

The $2\mathcal{F}$-statistic in Equation 5.10 depends only on the Doppler parameters, which are generally known for a neutron star. We use this value as the $\mathcal{F}$-statistic in frequentist searches [49].

If no signal is present, the $\mathcal{F}$-Statistic is a random variable which follows a central χ^2-distribution with 4 degrees of freedom. The probability density function of this distribution is given as

$$p_0(2\mathcal{F}; 4, 0) = \frac{\mathcal{F}}{2} e^{-\mathcal{F}}. \tag{5.11}$$

If there is a signal present in the data, the distribution of the $2\mathcal{F}$-statistic follows a non-central χ^2-distribution with 4 degrees of freedom and ρ^2 is the non-centrality parameter, where ρ is the SNR from equation 2.33. The probability distribution function of the $\mathcal{F}$-statistic with a signal present is

$$p_1(2\mathcal{F}; 4, \rho^2) = \frac{1}{2} e^{(-2\mathcal{F}+\rho^2)/2} \sqrt{\frac{2\mathcal{F}}{\rho^2}}\, I_1(\sqrt{2\mathcal{F}\,\rho^2}) \tag{5.12}$$

where $I_1(\sqrt{2\mathcal{F}\,\rho^2})$ is the first kind, first-order Bessel function, expressed as

$$I_1(x) = \frac{x}{2}\sum_{j=0}^{\infty}\frac{(x^2/4)^j}{j!\;\Gamma(j+2)}. \tag{5.13}$$

If the parameters defined in the search are perfectly matched to the signal present in the data, $\boldsymbol{\lambda}_s = \boldsymbol{\lambda}$, then the expectation value of the $\mathcal{F}$-statistic is [69]

$$\mathrm{E}[2\mathcal{F}] = 4 + \rho^2. \tag{5.14}$$

As mentioned at the beginning of the chapter, we need to set a detection threshold of $2\mathcal{F}^*$. Using this value, we can easily integrate 5.1 and get the false alarm probability

$$p_{\mathrm{fa}}(2\mathcal{F}^*) = (1 + \mathcal{F}^*)e^{-\mathcal{F}^*}. \tag{5.15}$$

If we set this probability to $p_{\mathrm{fa}} = 1\%$, then $2\mathcal{F}^* \approx 13.3$. We can then use this value to solve 5.2 numerically to find the required ρ for a false dismissal rate. If we set $p_{\mathrm{fd}} = 10\%$, then $\rho \approx 4.5$ [69].

Finally, it is important to define the *upper limit* of the gravitational wave amplitude, where we limit the gravitational wave emission from the neutron star. We will call this limit, h_0^C where C is the frequentist confidence, the frequency with which the interval $[0, h_0^C]$ contains the true value of h_0 in repeated experiments,

$$C = \int_{2\mathcal{F}_0}^{\infty} F(2\mathcal{F}|h_0^C)\, d2\mathcal{F}, \tag{5.16}$$

where $2\mathcal{F}_0$ is the value of the loudest candidate [69].

Next, I will introduce the *narrow-band search* which will iterate searches over various Doppler parameters $\boldsymbol{\lambda}$ in a small window and calculate the $\mathcal{F}$-statistic for each scenario and find the resulting distribution.

5.2 The narrow-band search

As described in Section 5.1.1, the $\mathcal{F}$-statistic is a maximum likelihood statistic calculated for different possible parameters of $h(t)$. We define a signal $h(t; \mathcal{A}, \boldsymbol{\lambda})$ where $\mathcal{A}$ is the set of amplitude parameters, h_0, $\cos\iota$, Ψ, ϕ_0. The vector $\boldsymbol{\lambda}$ is the Doppler parameters, the position n of the source as well as the frequency and frequency derivatives.

In continuous wave searches, the amplitude parameters $\mathcal{A}$ from Table 2.2, are generally unknown and the Doppler parameters, $\boldsymbol{\lambda}$ described in Table 2.1, are estimated for position, α, δ, frequency, f and frequency derivatives. For the narrow-band search, these Doppler values, $\boldsymbol{\lambda}$, are also treated as unknowns over a small parameter space. This allows for the possibility that frequency may not be at precisely twice the spin-frequency as well as the position may not be as well-defined. Therefore this search is considered a "directed" search where templates are created for values within $\boldsymbol{\lambda} \pm \delta\boldsymbol{\lambda}$ where $\boldsymbol{\delta}$ is a small window in the parameters for α, δ, f and $\dot{f}$.

By defining the spacing of the templates, I get a number of templates, N_t. Each template N_i returns a $2\mathcal{F}$ value for the specific values of $\boldsymbol{\lambda}_i$. As described in section 5.1.1, the distribution of these values is a χ^2-distribution with a non-centrality parameter of ρ^2 if a signal is present which converges to 0 if there is no signal.

It is unlikely that a template with parameters $\boldsymbol{\lambda}_i$ will perfectly match the signal parameters, $\boldsymbol{\lambda}_s$. The offset $d\boldsymbol{\lambda} = \boldsymbol{\lambda}_i - \boldsymbol{\lambda}_s$ will cause a loss of the $\mathcal{F}$-statistic. This loss is referred to as the *mismatch* and is defined as

$$m(\boldsymbol{\lambda}_s, d\boldsymbol{\lambda}) = \frac{\mathrm{E}[\mathcal{F}(\boldsymbol{\lambda}_s)] - \mathrm{E}[\mathcal{F}(\boldsymbol{\lambda})]}{\mathrm{E}[\mathcal{F}(\boldsymbol{\lambda}_s)]}, \tag{5.17}$$

where $\mathrm{E}[\mathcal{F}(\boldsymbol{\lambda}_s)]$ is the local maximum of $\mathcal{F}$ if there is a signal in the parameters $\boldsymbol{\lambda}_s$ [69]. This mismatch is used to define the template overlapping in the narrow-band

search.

The local metric g_{ij} which arises from m can be approximated as

$$g_{ij} \sim \langle \partial_i \phi \partial_j \phi \rangle - \langle \partial_i \phi \rangle \langle \partial_j \phi \rangle, \tag{5.18}$$

as shown in [68] and [24] where $\phi(t)$ is the phase of the signal, $\partial_i = \partial / \partial \boldsymbol{\lambda}^i$ and $\langle ... \rangle$ is the average over the observation time, T_{obs} [69].

These $\mathcal{F}$-statistic values are computed using the code `ComputeFStatistic_v2` found in the LSC Algorithm Library (LAL) code routines [26]. The $2\mathcal{F}$ value is calculated for each data template N_i and sums the results. This resulting distribution is then compared to the expected probability distribution.

We use Short-Fourier Transforms (SFTs) of 30 hr durations to move the data into frequency space. These SFTs are then combined to form Power Spectral Densities (PSDs) at individual frequencies where the detector data can then be analysed.

5.3 Applying a multi-template search for a signal from the Crab pulsar in S6 data

First, I test the narrow-band method by searching for signals from the Crab Pulsar (PSR B0531+21) in the sixth science run (S6) of LIGO data and the 3rd science run of the Virgo detector. Previous searches for the Crab Pulsar included a 30 m interferometer search by Levine and Stebbins in 1972 [55] and bar detector searches from Hirakawa et al (1978) [42] and Suzuki in 1995 [77]. All of these searches resulted in a gravitational wave upper limit which was above the spin-down limit of the Crab.

The first result from the LIGO detectors was from the second science run (S2), which gave a 95% upper limit of $h_0^{95\%} = 4.1 \times 10^{-23}$ [7]. Combined data from the

third and fourth science runs gave an upper limit of $h_0^{95\%} = 3.1 \times 10^{-24}$, only 2.2 times higher than the spin-down limit [8].

When the fifth science run (S5) data was analysed, both the narrow-band search (previously referred to as the wide-parameter search) and a targeted pipeline [10] were used to set upper limits as discussed in Section 2.6.1. This section will perform a new analysis on the subsequent detector science run using only the narrow-band search.

S6 multi-template analysis

For this search, I used a relatively short observation time of $\mathrm{T_{obs}} = 28$ days from S6 in the GPS time range 932000000 - 934419200. I searched 566 SFTs for H1, 719 SFTs for L1 and 1181 SFTs for Virgo. This is because although the previous search in [10] used S5 data from $\sim$ November 2005 through August 2006, the computing cost of the narrow-band search is proportional to $C_c \propto T_{\mathrm{obs}}^6$ [69] and the SNR only improves as $\rho \propto T_{\mathrm{obs}}^{-1/2}$. Given a limited computing time, with little improvement on ρ, it was not worth increasing T_{obs} to more than 28 days. Yet, this is still an opportunity to test the S6 data and understand the narrow-band search for the future Advanced Detector searches.

First, I set the central parameters and a window over which the narrow-band algorithm will search. This determines the number of templates and computing time the search takes. The 4 Doppler parameters I started with as well as their windows are shown for this search in Table 5.1.

To calculate the expected distribution, I assumed a Gaussian distribution of $2\mathcal{F}$ values to get the equation

$$p(N_i|2\mathcal{F}_i) = \frac{1}{\sqrt{2\pi\langle N\rangle}} e^{\frac{-(N-\langle N\rangle)^2}{2\langle N\rangle}} \tag{5.19}$$

$\boldsymbol{\lambda}_i$	Central value	Window
α	1.45967	0.005
δ	0.384224	0.005
f_0	59.55577	10^{-3}
f_1	-7.4588×10^{-10}	5×10^{-10}
PEPOCH	813369613	

Table 5.1 – Parameters given for the S6 narrow-band search for the Crab pulsar where f_1 is the first time derivative of f

where $\langle N \rangle$ is the expected number of $2\mathcal{F}$-values given no detection and is calculated from the central χ^2-distribution to be

$$\langle N \rangle = \frac{N_{\text{tot}}}{2} \mathcal{F}_i e^{-\mathcal{F}_i} \Delta\mathcal{F}_i. \tag{5.20}$$

The total number of templates searched are $N_{\text{tot}} \approx 4.5 \times 10^7$. The distribution of the resulting $2\mathcal{F}$ values calculated from each template are shown in Figure 5.1. The expected line is from Equation 5.19. It is clear that the $2\mathcal{F}$ values from the search follow this distribution. The discrepancy at the peak of the curve is due to known implementation details of `ComputeFStatistic_v2` as described in Section IV B of Wette, 2012 [86].

If we want to calculate the cutoff value of $2\mathcal{F}^*$, where the probability P that all templates are below $2\mathcal{F}^*$ then take $1 - P$ and set it equal to 1%. If we integrate Equation 5.11 from 0 to $2\mathcal{F}^*$ to get (for a single template)

$$P_{\text{single}}(2\mathcal{F}^*) = \frac{1}{2}(1 - (1 + \mathcal{F}^*)e^{-\mathcal{F}^*}), \tag{5.21}$$

which is the probability of one template being below the threshold $\mathcal{F}^*$. Each search is independent, so we simply need to multiply the probability by N_{tot} to get P, take $1 - P$ and set it equal to 1% to numerically solve for $\mathcal{F}^*$ which gives a value of ~ 49.

This search resulted in a maximum $2\mathcal{F}_{\text{max}} = 41$ which is less than the $2\mathcal{F}^*$ threshold,

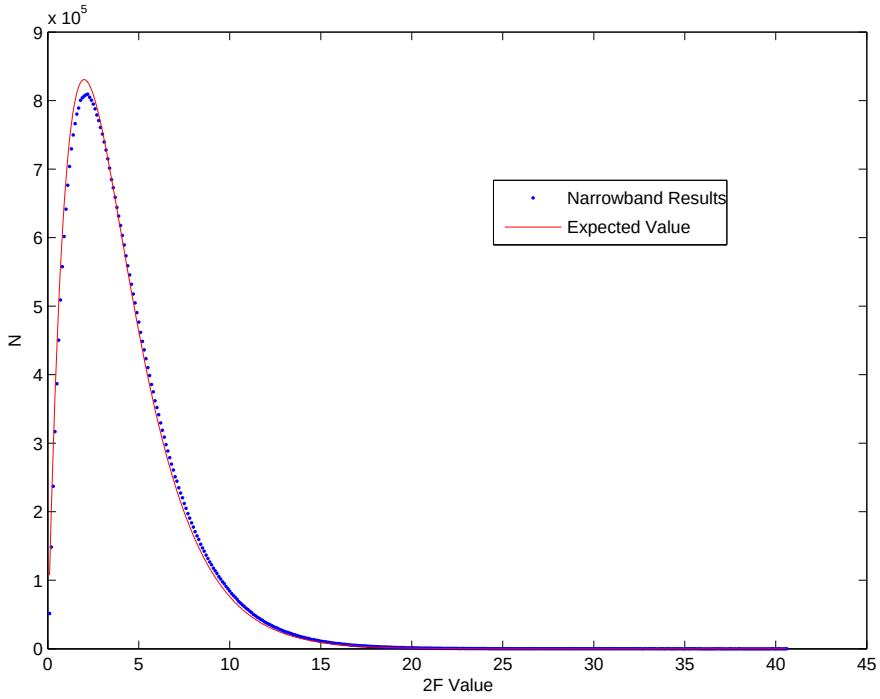

Figure 5.1 – Results of the 28 day narrow-band search of the Crab pulsar. The gap at the peak between the expected value and the results are due to implementation details of the $\mathcal{F}$-statistic code [86].

which means this is consistent with a no-signal distribution.

5.4 Recovery of a hardware injected signal in recent data

In the Initial LIGO runs, the head committee conducted blind hardware injections, unknown to the individual data analysis groups. The purpose of these is to fully test the methodology for declaring a known detection and testing the science which can be done with the searches, such as extracting the parameters. In the sixth science run (S6), two blind injections were made, a coalescing binary signal and a continuous wave signal. The coalescing binary signal was flagged as the "Big Dog" signal and the recovery is described in Abadie *et. al* [5]. During the discussion for the Big Dog event, the CW signal was revealed to have been injected in September 2009. This

section recovers this signal using the narrow-band search with the parameters given to the group post-injection. By recovering this injection, we can confirm the validity of this method of injecting blind signals.

The CW signal was injected for 28 days of S6 between 969837280 and 971622272. I searched 542 SFTs for H1, 462 SFTs for L1 and 747 SFTs for Virgo. The parameters of the injection are given in Table 5.2.

$\boldsymbol{\lambda}_i$	Central value	Window
α (rads)	2.454	0.005
δ (rads)	0.465	0.005
f_0 (Hz)	643.352	10^{-3}
f_1 (Hz s^{-1})	-8.84e-11	5×10^{-11}
PEPOCH (sec)	751680013	

Table 5.2 – The values that were injected into the S6 data with the windows used in the narrow-band search.

This search included $N_{\rm tot} \approx 1.7 \times 10^7$ templates and the results of the narrow-band search are given in Figure 5.2

The highest $2\mathcal{F}$ value from this search has a value of 2010. The false alarm probability of obtaining this $2\mathcal{F}$ value when there is not actually a signal in the data is effectively zero, which states definitively that this is a strong injection.

The parameters recovered are shown in Table 5.3. The time-derivative of the frequency has the highest error, but in a short $T_{\rm obs}$, this is difficult to recover well.

$\boldsymbol{\lambda}_i$	Recovered Value	Error
α	2.4543579	0.02%
δ	0.4654563	4.5×10^{-6}%
f_0	643.3325	1.34×10^{-5} %
f_1	-9.47120$\times10^{-11}$	7.1 %

Table 5.3 – These are the recovered parameters from the narrow-band search for the continuous wave hardware injection in S6.

The recovered amplitude parameters are shown in Table 5.4. The uncertainty in

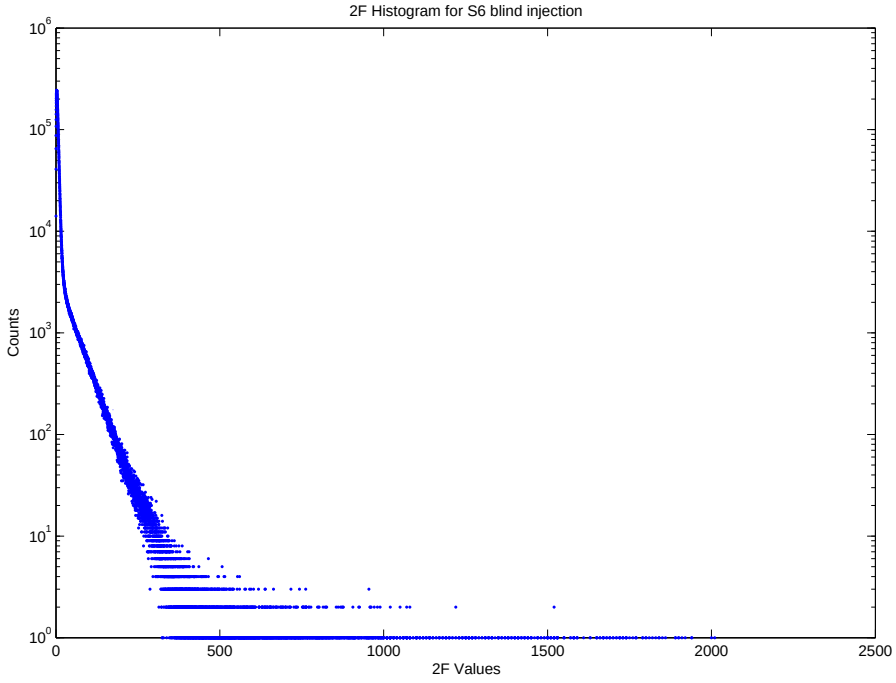

Figure 5.2 – Results of the 28 day narrow-band search of the S6 continuous wave hardware injection. The dots represent the number of $2\mathcal{F}$ values achieved for each template. No signal present would result in a sharp distribution concentrated at lower $2\mathcal{F}$ values.

these values is high, but it is difficult to recover these values as they are completely unknown with no priors.

$\mathcal{A}_i$	Recovered Value	Uncertainty
h_0	3.15355×10^{-24}	17.3%
$\cos\iota$	0.723358	20.1%
ϕ_0	2.65094	23.2%
Ψ	0.172732	177.1%

Table 5.4 – Recovered amplitude parameters from the narrow-band search for the S6 hardware injection

This narrow-band search was able to detect the S6 continuous wave injection. Though the amplitude of the signal was well above the sensitivity of S6, this shows that the narrow-band search is an effective method for detecting a signal when it is possible.

5.5 Discussion of search and the implication of the results

For this chapter, I explored two different perspectives for utilising the narrow-band search in continuous wave data analysis. In the Advanced Detector era, this search will be able to perform both independently (as demonstrated in this chapter) as well as a middle step between the blind and targeted searches as discussed in Chapter 2.

First, I ran a parameter search for the Crab Pulsar in the S6 data allowing us to place an upper limit on the gravitational wave emission from the Crab pulsar at frequencies and frequency derivatives in a region around the values predicted by radio observations. In an observation time of $T_{\text{obs}} = 28\,\text{days}$ I was unable to place a better upper limit compared to the S5 result. This is due to the fact that although the S6 data is more sensitive than S5, T_{obs} is much less. Though T_{obs} was much

smaller, it was still worth running this search over a separate science run as there is a possibility that pulsars may have variable emission as discussed in Lyne *et. al*, 2010 [56].

Next, I ran a search on a blind hardware-injected signal in the S6 data. This signal had a high amplitude so it was easily recovered by the narrow-band search and demonstrates effectively what signal detection will be like with higher sensitivity in the Advanced Detector era. I was able to confidently detect this signal and recover the correct parameters. This shows that the narrow-band search is a valid and effective way of running a directed search for signals where estimated Doppler parameters are known. Additionally, it verifies the blind injection process where people who are not directly involved in continuous wave analysis successfully injected a recoverable signal.

6

Development of a data set for the continuous wave mock data challenge

Part of the process of preparing for regular detections of gravitational wave signals with advanced detectors involves testing the algorithms on simulated signals within realistic data. Throughout the initial LIGO Science Runs (S1-S6), signals were artificially injected into the data through the hardware. This means an end mirror in the detector was moved in a way that caused the output to resemble a gravitational wave signal. For short-duration events, such as signals from supernovae or coalescing compact objects, this is acceptable as it only affects a short stretch of the data. For long-duration signals, like continuous waves from neutron stars, it is not feasible to generate many signals in this manner because they will contaminate the actual data output and interfere with other types of searches, particularly the stochastic search.

To appropriately test search techniques, it is ideal to have simulated signals which imitate actual signal detection processes, hence the use of hardware injections. Real-

istically, continuous wave signals would be always present in data, but as explained above that is not an option from a hardware perspective for many signals. The alternative is to use software to generate a full set of data with continuous wave signals present throughout.

An alternative method of introducing a signal into the data involves superimposing the signal onto the detector output at the processing stage. Software injections of signals have been used in the past for individual testing of algorithms. A simulated signal can be generated using the code `Makefakedata_v4` found in the LSC Algorithm Library which reads in user-defined parameters such as position, spin, etc. about the neutron star, the gravitational wave parameters and information such as type of output and duration of signal [26]. The types of output are generally Short Fourier Transforms (SFTs) or the raw detector frame output.

Despite the existence of software injection codes and the current use of software injections for testing the CW group algorithms, no large-scale methods to effectively generate a full set of data with multiple signals present existed. To develop this, it was necessary to develop code which could generate simulated neutron star population data, including neutron star position, orientation and spin parameters, generate a signal for each of these and add them all to existing frame files over an entire science run.

This chapter will describe the development of this code as well as the final dataset currently being used in the CW group. This dataset uses the strain data from the sixth LIGO Science Run (S6) and contains artificial signals from all known pulsars as well as 3000 additional simulated signals. These software injections are of particular use to compare blind-all sky searches as there are many signals present over a wide range of strengths, which allows us to exercise the algorithms over a wide range of conditions. Additionally, while each individual all-sky search has ran their own tests, this is the first large-scale, comprehensive method for testing performance.

6.1 Signal parameters

The first step in developing this dataset is to determine the parameters of the simulated neutron stars and write them out in such a manner that they can be automatically read in. This allows us to automatically generate as many signals as necessary. The simplest method is to have a directory which houses a set of files, each describing the necessary parameters for an injection simulating a single neutron star. The Australia Telescope National Facility (ATNF)[1] pulsar database utilises the timing package Tempo2 [44] which dictates a standard pulsar parameter format. By using this file format, we can maintain consistency between the pulsar and gravitational wave communities.

In order to effectively test the algorithms, it is useful to have a large set of neutron star signals over the entire gravitational wave frequency range with signal strengths having a variety of signal–to–noise ratios (SNRs). The CW group has searches which vary greatly in sensitivity, from the targeted search with the highest sensitivity, to blind, all-sky searches with low sensitivity. The approximate difference between these extremes is a factor of 20-30, so we need a range of SNRs in order for this to be an effective method for testing all of the CW algorithms.

As mentioned above, this project is particularly important to test the multiple all-sky searches, so the SNR range will be catered to their sensitivity. The strengths of the software injections will have a spread over the sensitivity curve seen in Figure 1.4.

To avoid the signals interfering with each other in the searches, due to the fact that the algorithms are not designed for multiple signals at the same frequency, the gravitational wave reference frequencies will be uniformly distributed and be spaced at $\Delta f_{\mathrm{gw}} = 0.5\,\mathrm{Hz}$ intervals. The other neutron star parameters will all be chosen from random, uniform distributions.

[1] `http://www.atnf.csiro.au/`

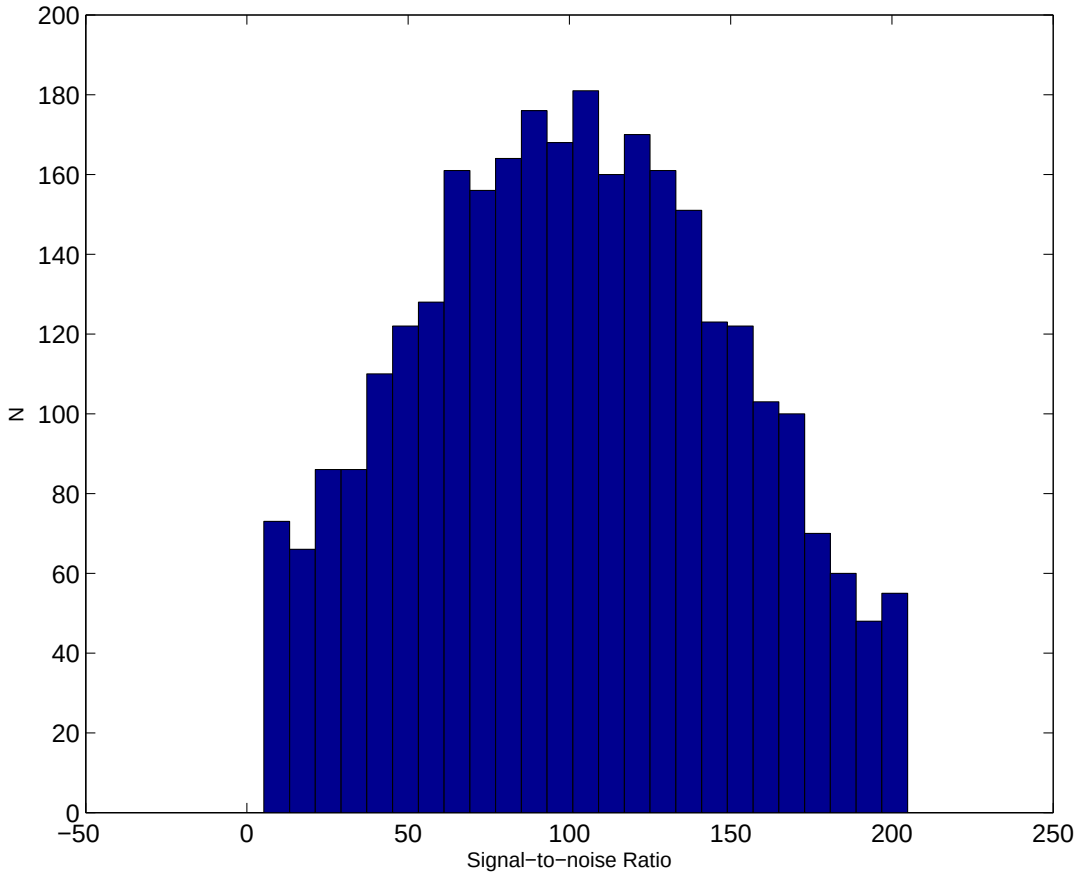

Figure 6.1 – The SNR distribution of the software injected signals corresponding to a targeted signal search. The mean is 100, the standard deviation is 60 with upper and lower cutoffs of 5 and 205, respectively.

To determine the parameters of each individual neutron star, we start by choosing a SNR from a Gaussian distribution with a mean of 100, a standard deviation of 60, and limited to SNR $\in [5, 205]$. We will use calculations from the targeted search to determine the h_0 value, which would then give a range of SNR for the all-sky searches centered on ~ 10. The lower cutoff of 5 is to limit the SNRs from being negative and the upper limit of 205 is to maintain symmetry. The choice of a Gaussian distribution for SNR is to give the targeted search a few signals with a low SNR to test the limits. As well, there are a few at a high SNR to make sure that the all-sky searches will detect at least those. There are a lot in the middle that may challenge the various searches. The distribution of the SNRs are shown in Figure 6.1.

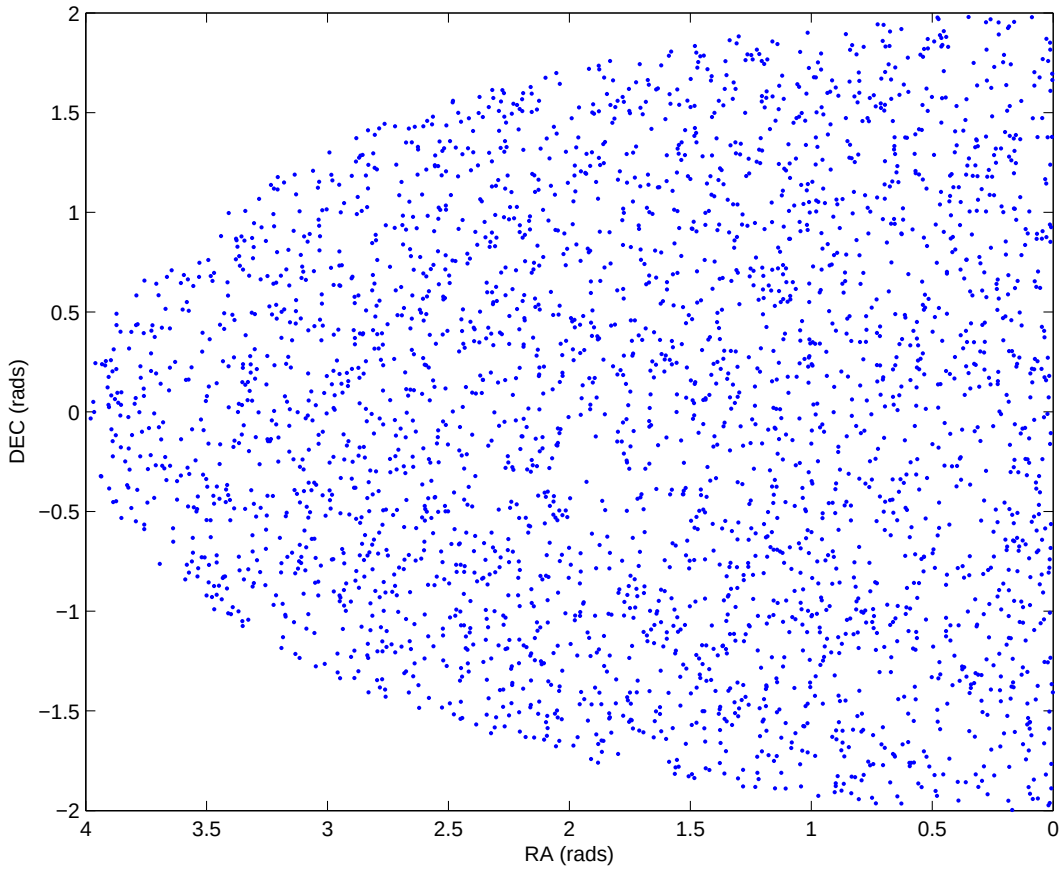

Figure 6.2 – Right ascension and declination of the uniform distribution of neutron stars.

Once a fixed SNR, ρ, and frequency, f_{gw}, are chosen, the position in the sky is randomly chosen from a uniform distribution and are shown in Figure 6.2. The distribution of the orientation of the neutron star is uniform in $\cos\iota$, as well as the polarisation, Ψ as seen in Figure 6.3. The phase of the signal is also randomly chosen from the interval $\phi_0 \in [0, 2\pi)$.

The last neutron star parameter distribution which needs to be defined is the spin-down value, $\dot{f}_{\mathrm{gw}}$. Uniform distributions were appropriate for the other parameters, but for $\dot{f}_{\mathrm{gw}}$, a uniform distribution is inappropriate. This is especially important because the all-sky searches are designed based on a realistic distribution of f_{gw}-$\dot{f}_{\mathrm{gw}}$ (examples in [12]). Currently, approximately 5% of known neutron stars have a

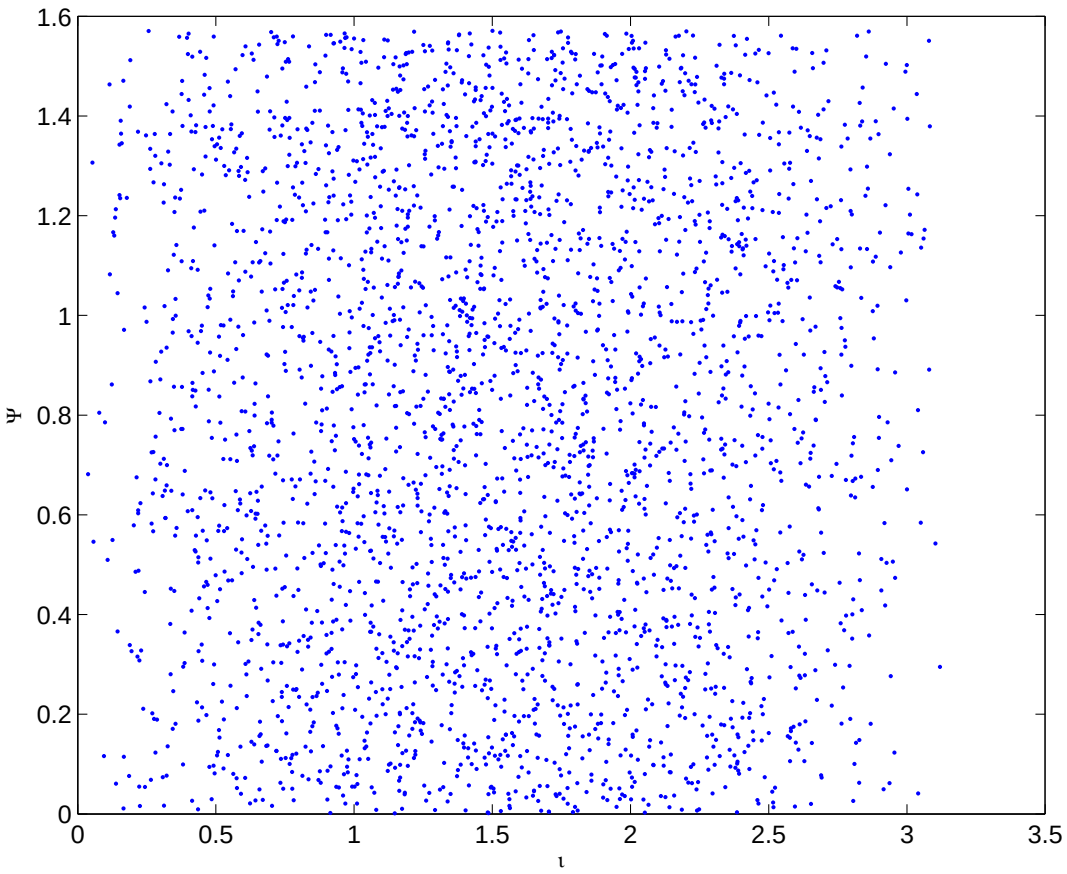

Figure 6.3 – Distribution of the orientation of the pulsars (ι and Ψ).

positive $\dot{f}_{\rm gw}$ value (spin-up) mostly due to the acceleration of sources toward Earth, so this will be applied to these software injections. The $\dot{f}_{\rm gw}$ values for the injections are randomly chosen from the limited log distribution,

$$\log\left(\frac{|\dot{f}_{\rm gw}|}{\rm Hz\ s^{-1}}\right) \in \left\{ \begin{array}{ll} -9, -18 & \text{for} \quad \dot{f}_{\rm gw} < 0 \\ -18, -13 & \text{for} \quad \dot{f}_{\rm gw} > 0 \end{array} \right\} \tag{6.1}$$

where only 5% are chosen from the latter set of positive spinup values, $[10^{-18}, 10^{-13}]$ Hz s^{-1}. The distribution of $\dot{f}_{\rm gw}$ is shown in Figure 6.4. A summary of all of these neutron star distributions are shown in Table 6.1.

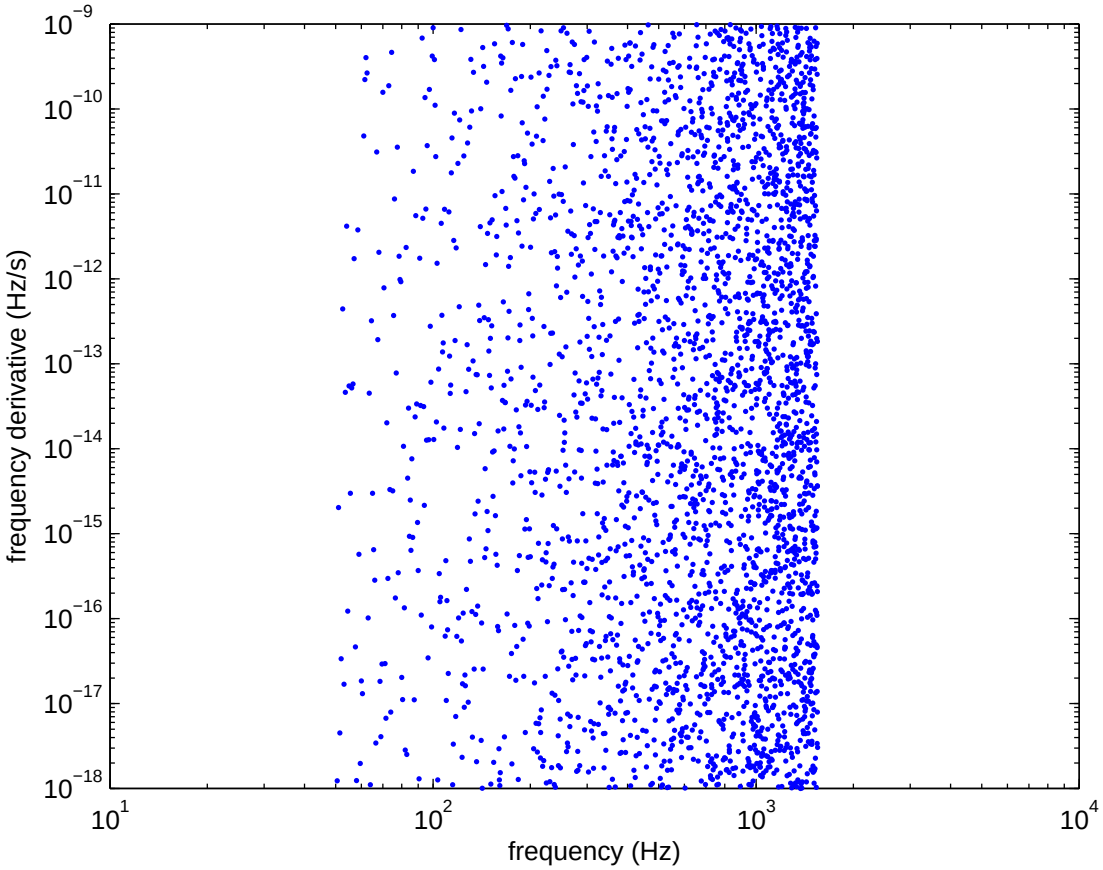

Figure 6.4 – Frequency versus $|\dot{f}|$ of the software injection parameters.

As discussed in Chapter 4, proper motion is unlikely to affect the all-sky searches. However, it was included in this data set before the results of Chapter 4 were com-

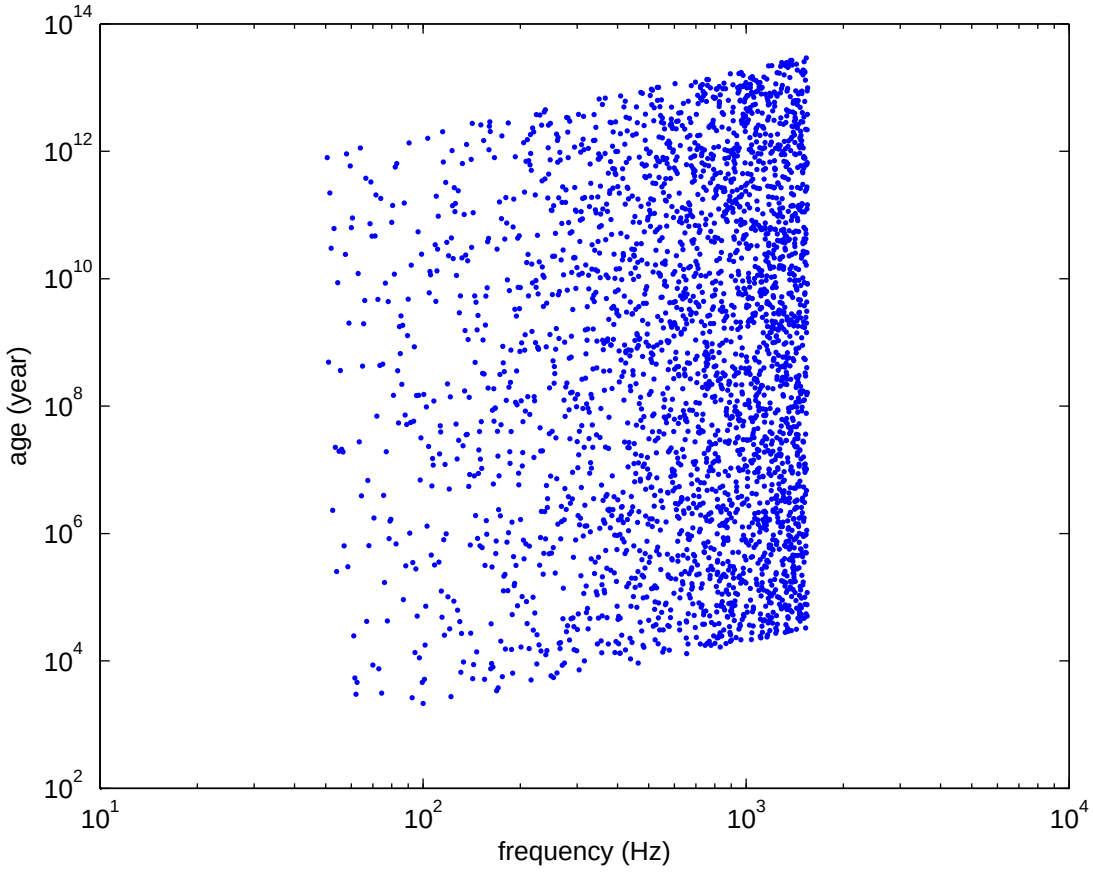

Figure 6.5 – Plot of f versus age (years).

Parameter	Distribution
SNR	Gaussian distribution: $\mu = 100$, $\sigma = 60$, $\mathrm{SNR}_{\mathrm{min}} = 5$, $\mathrm{SNR}_{\mathrm{max}} = 205$
f_{gw}	Range from 50.25 Hz to 1550 Hz at 0.5 Hz intervals
f_{gw}	Random and uniform distribution in $\log(\dot{f}_{\mathrm{gw}})$ from -10^{-9} to $+10^{-13}$ (eliminating spin-downs between -10^{-18} to $+10^{-18}$) and fewer than 5 percent spin-up (positive range)
Location	Random and uniform distribution in sky
Ψ	Random and uniform ranging from $-\pi/4$ to $\pi/4$
ϕ_0	Random and uniform ranging from 0 to 2π
$\cos\,\iota$	Random and uniform from -1 to 1
h_0	Calculated from assigned SNR, f from above distributions and H1 S6 sensitivity curve

Table 6.1 – The distribution of the parameters of the pulsars from which the software injections are calculated

.

pleted. From the ATNF database of actual observed neutron stars [58] (as seen in Figure 4.5), we can approximate a distribution of proper motions as two separate Gaussian distributions in the RA and DEC directions. For the right ascension, the distribution has a mean of 3 mas yr^{-1} and a standard deviation of 36. In declination, the distribution has a mean of -3 mas yr^{-1}. Due to a few outliers in the data, a Gaussian fit was not appropriate, so these values were estimated by setting the mean and standard deviation to match that of the ATNF data.

We also need to include the frequency epoch which is the time were f_{gw} is equal to the reference frequency. This value is necessary in order to adjust the frequency and position based on the spindown and proper motion values. For these software injections, we used a single reference epoch of GPS time 946339215.

The values for h_0 are calculated by manipulating Equation (2.33) to

$$h_0 = \rho \frac{\sqrt{S_n}}{\sqrt{T_{\mathrm{obs}}}} \left[\frac{1}{2}(1 + \cos^2 \iota) F_+^2 + \cos^2 \iota F_\times^2 \right]^{-1} \tag{6.2}$$

where ρ is the chosen SNR, S_n is the detector noise corresponding to f_{gw} for the

neutron star and T_{obs} is the observation time which for this case, $T_{\mathrm{obs}} = 1\,\mathrm{yr}$ [64]. The values in $[\cdots]$ are time-averaged over a day and represent the antenna pattern (as discussed in Section 2.4) for the specific detector H1. These calculated values are shown in Figure 6.6. As mentioned before, this calculation is based on a targeted search, approximately 10-15 times more sensitive than the all-sky searches. This accounts for all of the sources being a factor of 10 or so stronger than the sensitivity curve. If an all-sky search were to attempt to find these sources, the mean value would approximately lie on the curve.

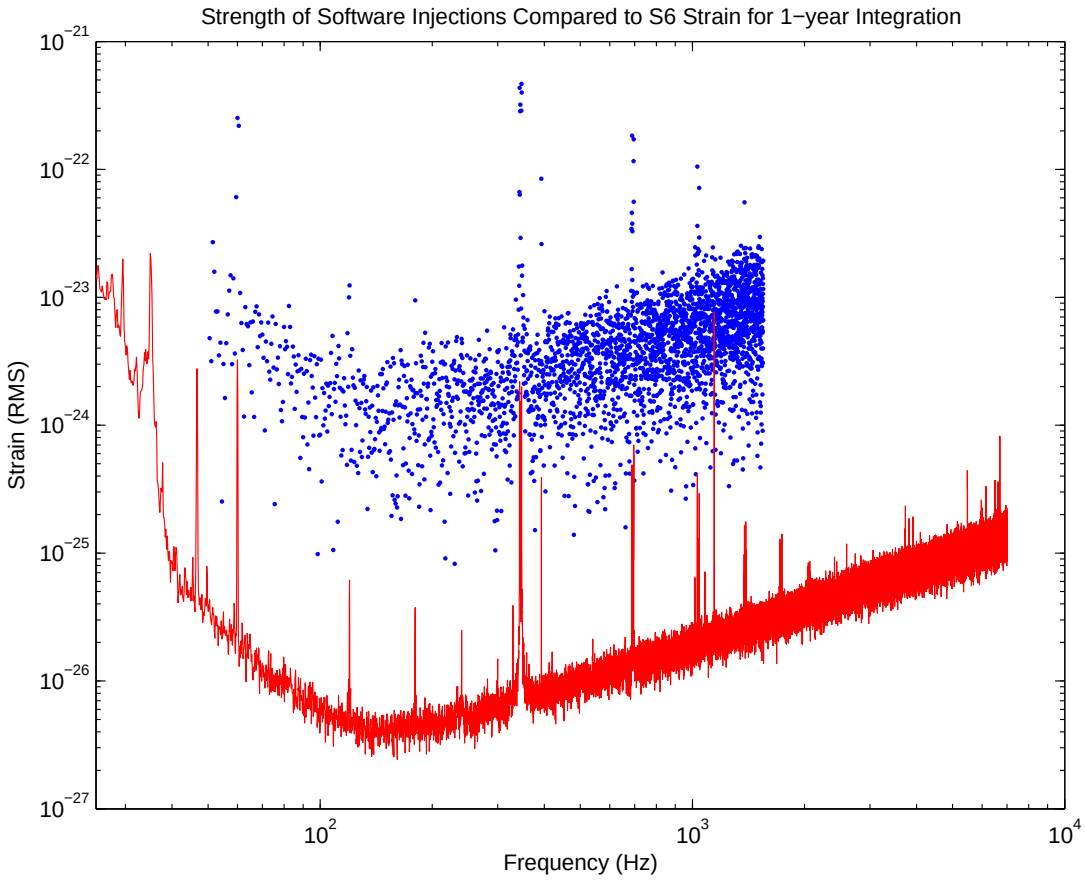

Figure 6.6 – Distribution of h_0 values for each injected pulsar compared to H1 strain for one-year integration on a targeted search.

Once h_0 has been determined, the parameters are written out to a text file, in the format of the Tempo2 parameter files, but with the gravitational wave parameters, h_0, $\cos\iota$, Ψ and ϕ_0 included. The code written to generate these writes out one

file for each neutron star and stores it in a directory, to be used for the software injection code.

6.2 Description of software injection code

The objective of this code is to rewrite the entire data set for the sixth LIGO science run (S6). This presents many logistical difficulties such as computation time and automation of the code. This code utilises many existing codes in the LSC Algorithm Library Suite (LALSuite), written and managed by members of the LVC.[2]

6.2.1 Considerations and difficulties

The first consideration when writing this code is the extremely large volume of data which needed to be read in and copied. The sixth science run was from July 2009 to October 2010 and the raw data was sampled at 16384 Hz. This resulted in approximately 10 TB of data which needed to be read in, replicated across sites and stored. It is imperative to make sure that this amount of data can be generated in a reasonable amount of time with a limited impact on the computational clusters.

Another issue to consider is how much control the group has on the strength of the signals. There was discussion in the group on whether or not they can individually modify the signal to cater towards testing their own algorithms. However, the original reason for developing these software injections was mainly to comprehensively test the blind, all-sky algorithms and this is best done when the sources are unknown.

Current LIGO data frame files follow a specific format and it is necessary to maintain this when generating a new set of frames. The collaboration uses a system called

[2] `https://www.lsc-group.phys.uwm.edu/daswg/projects/lalsuite.html`

the LIGO Data Analysis Software (LDAS) formatting.[3] The format specifications include the structure of the file frame names, which include the detector (H1, L1, H2 ...), the type of frame channel, the start time of the data in GPS seconds and the duration of the data appended with the file extension ".gwf". Each frame file contains a set of channels which represent various aspects of the data. By maintaining the standards of LDAS, this allows the data to be included in the LIGO frame database for future reference.

The final important consideration in this development is to decide on the type of data to distribute to the group for analysis. Many of the algorithms read in Short Fourier Transforms (SFTs) of the data which are generated separately from detector frames. Because the SFTs are so commonly used, generating them as part of the software injection project before distributing to the group for individual analysis was an option. However, the best method for truly testing the algorithms is to replicate the analysis process as identically as possible. Therefore once the software injection frames are generated, they are handed directly to the group in raw form and then the standard process done by any individual groups is conducted as would be with any original detector data.

6.2.2 Code overview

First, the code needs to read in the neutron star parameter files described in Section 6.1 and store the values in order to calculate the injection in an appropriate data format. To make the code computationally efficient and minimize memory usage, the parameters are read in first and stored in arrays which are called later in the code, instead of reading in the parameters separately for every detector frame file.

Then the original data frame files are read in one at a time and the data is extracted and checked. As mentioned above, the start time and duration of the frame data

[3] `http://www.ldas-sw.ligo.caltech.edu/`

are given in the file name of the original frames. This information is read in directly from the file name and then used to generate the injections. Typically, each frame is 128 s worth of data and is always sampled at 16384 Hz which results in a file of approximately 30 MB. The start time of the frame is given in GPS seconds.

The signals from each neutron star are generated and added together as one vector. This vector is then added to the output frame file as one channel which just contains the pure set of signals, with no noise included. This then gives the group the ability to access the pure signals and extract them to modify them as necessary for their own tests.

The vector of signals is then added to the raw data extracted from the detector frame file to generate a vector which contains both the signals and the noise. This comprises a second channel in the output frame file which the group will then use to analyse for the overall algorithm comparison.

The code then writes out a new file which contains two channels, one with just the signals and one with the original gravitational wave data and the signals included. Then the code loops through the next raw data file and repeats the process.

Command line arguments for this code are simply the detector from which the data is taken, the directories which house the neutron star parameter files, the directory which holds the original gravitational wave frame files, the output directory and the year and directory for ephemeris files which are used to calculate the exact position of the Sun and Earth which affect the waveforms. A log file is written for each raw frame file directory, detailing all parameters used for future reference if necessary. The code flow can be found in Figure 6.7.

The workload computing management system Condor[4] was used to run this code. This effectively schedules and runs computing jobs on the computing clusters. Condor codes were written to manage the command line arguments in order to cycle

[4] `http://research.cs.wisc.edu/condor/`

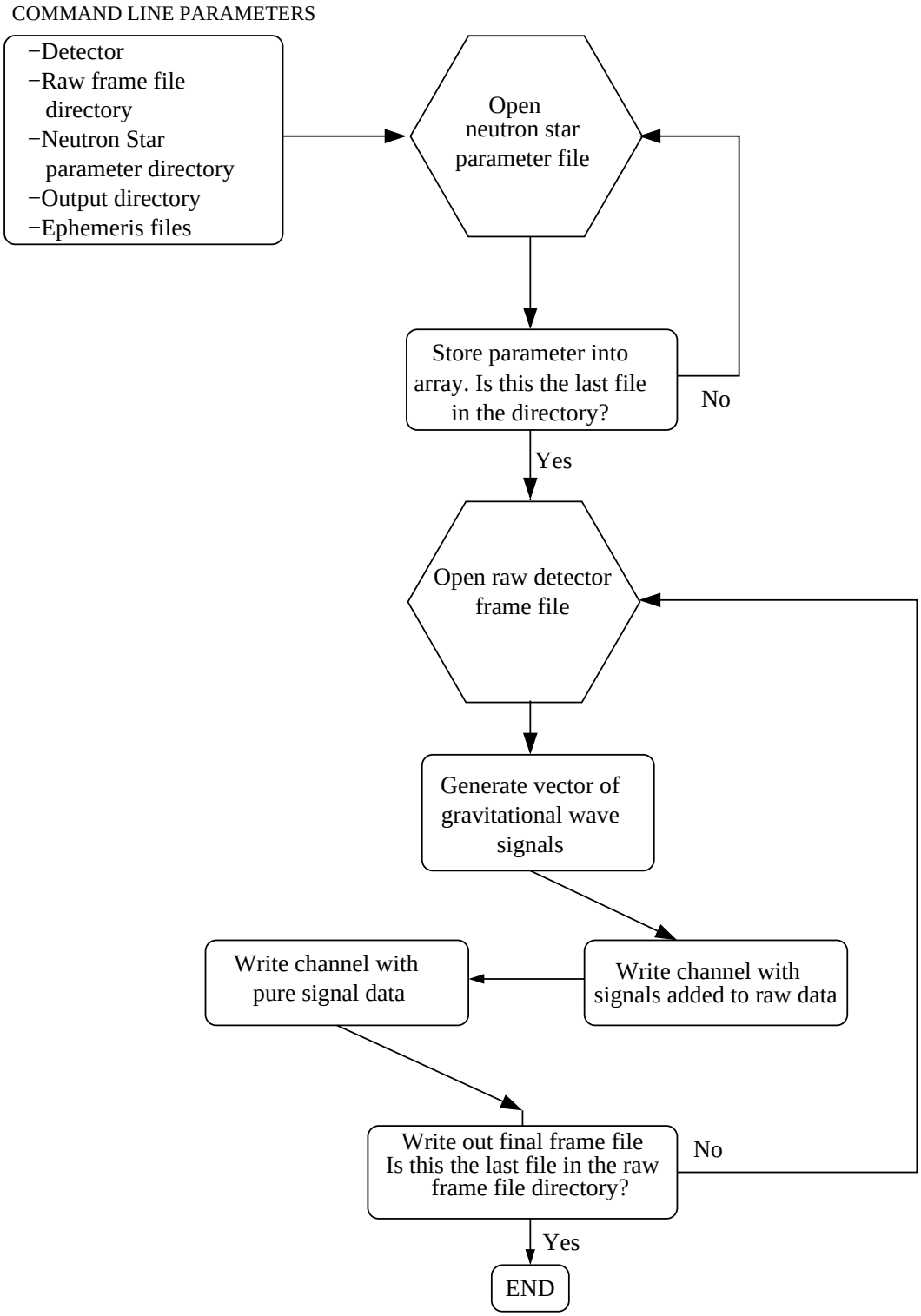

Figure 6.7 – Flow chart detailing the software signal injection code, starting with the command line parameters.

through directories of raw frame files.

These software injections were generated on the ATLAS computing cluster housed at the Max Planck Institute for Gravitational Physics.[5] It took approximately 1000 computing jobs, each job taking approximately 33 hours, and the total space of the generated frames came to 10 TB. Once generated, the new software frame files are moved to a permanent node and then transferred to the LDAS grid where they can be accessed by anyone in the collaboration for personal analysis.

Currently, the frames have finished generating on ATLAS and 99% have been transferred to the California Institute of Technology computing cluster to generally distribute to the LIGO Collaboration. The failed transfers were due to erroneous frames with zero content which occurred when cluster nodes crashed. These have been fixed and have yet to be transferred to Caltech. All of the frames which are at Caltech have been converted to SFTs as discussed in the following section. The all-sky search, PowerFlux, and the Bayesian time-based targeted search have done a primary analysis on this mock data. This is further discussed in Chapter 7.

6.3 Additional Processing

6.3.1 Generation of Short Fourier Transforms

Traditionally, Short Fourier Transforms (SFTs) are made from the raw detector frame data and used by a few of the search algorithms (see, for example, Chapter 5). These SFTs are generated from 30 min of raw data and transformed into frequency space.

Since these software injection frames are meant to mimic the entire method for data processing, these SFTs are currently being generated in the same manner at the

[5] `https://wiki.atlas.aei.uni-hannover.de/foswiki/bin/view/ATLAS/WebHome`

California Institute of Technology computing cluster.

Once the SFT generation is complete, the various algorithms in the continuous wave group who traditionally use these will process the data as they would normally.

6.3.2 Including binary neutron star signals

So far in this project, only isolated neutron stars are considered. The continuous wave group also has the infrastructure to search for continuous gravitational waves from binary neutron stars. According to current understanding of neutron star populations, approximately 25% are in binary systems [58].

Binary neutron star systems have much larger shifts in frequencies than isolated neutron stars. Mock signals from binary systems were not included in this initial set of software injections. This is due to the fact that binary systems vary widely in frequency over time and would affect the tests of isolated neutron stars. Due to the prevalence of binary neutron star systems, it is important to perform a similar test to compare current algorithms designed specifically for these systems.

6.3.3 Continuous wave mock data challenge

Now that the software injection frames are complete, it is necessary to design a comprehensive and effective method for comparing the algorithms in the continuous wave group. As explained above, some of the algorithms require further data processing of the raw data frames and will go through this process accordingly. This is because there might be a clear discrepancy in performance between two algorithms which seem to perform similar analyses but process the raw data differently, and we want to make sure this is caught.

Because this data processing can take extended computing time and space, full analysis of the software injections from all of the isolated neutron star algorithms

will take some time to be completed. The initial test of these injections frames can be performed by the targeted time-domain search, which uses the raw frame files directly and targets the search specifically on a single source. Additionally, as discussed in this chapter, the SNR for targeted searches is much higher than it would be for the other searches, making the recovery much simpler.

The algorithms in the continuous wave group require varied amounts of computing time, so an effective way to test the performances is to develop a challenge which accommodates all projects and still results in an improved understanding of performance. A tiered challenge system allows for limited available time while still comparing detection capabilities. This challenge was initially tested with the assistance of Colin Gill at the University of Glasgow using the time-domain targeted search as well as Vladimir Dergachev at California Institute of Technology using the all-sky search named PowerFlux. Initial tests were positive and will be described in detail in the following chapter, Chapter 7.

7

Mock data challenge and initial results

7.1 Details of the mock data challenge

The purpose of the software injections detailed in the previous chapter is to compare current CW search algorithm performance against a large data set of known signals. As discussed in Section 2.4, the CW group runs searches ranging from targeted searches which can achieve a high sensitivity to blind searches which have the capability to find previously unknown sources of gravitational wave radiation. To develop a mock data challenge which can account for the variety of searches, the injected data set is broken in half by position in the sky, with half of the signal parameters considered to be "known" for the targeted and directed searches and half of the parameters considered to be "unknown" to test the blind, all-sky searches. Currently, two searches have tested the ability to recover injections in a small frequency space and the results will be discussed here. The next step is to assign the same small frequency space to the entire group for initial testing and a more thorough comparison. The small frequency space is intended to cut down on the computing

time as well as the number of possible signals to recover for quick examination. Once this has been completed, a series of tests which will slowly expand the frequency space searched to include the full set of data.

The first challenge for the CW algorithms to analyse runs through $125 < f_{\mathrm{gw}} < 175\,\mathrm{Hz}$ and contains 49 injected signals. This frequency range was chosen because it has the best sensitivity and would additionally not require a high computational cost for the all-sky searches. This challenge is shown in Figure 7.1 with the red dots highlighting the CW signals in the given frequency. This frequency was chosen for the initial challenge because the all-sky searches' computing time is highly dependent on frequency. A lower frequency would allow for less computing time and quicker results.

The CW group utilises both time-domain and frequency-domain searches for signals. In this thesis, only the frequency-domain $\mathcal{F}$-statistic has been discussed, but there also exists a time-domain based targeted search which is used below to detect the known software injected signals. This chapter will also describe results from a blind, all-sky algorithm called *PowerFlux*, which searches in the frequency-domain.

7.1.1 Initial results from the blind, all-sky algorithm PowerFlux

The PowerFlux search is a continuous wave, blind, all-sky search. It searches within the frequency-domain using short Fourier transforms (SFTs). These SFTs are generated from 1800 seconds of data, are Hann-windowed ([85]) and 50% overlapping [9]. PowerFlux searches a five-dimensional parameter space of $\lambda = \{\hat{f}_0, \dot{f}, \alpha, \delta, \Psi\}$ where $\hat{f}_0$ is the initial gravitational wave frequency and Ψ is the polarisation angle, from the parameters described in Tables 2.1 and 2.2. PowerFlux is the only all-sky search which searches explicitly for the polarisation angle [9].

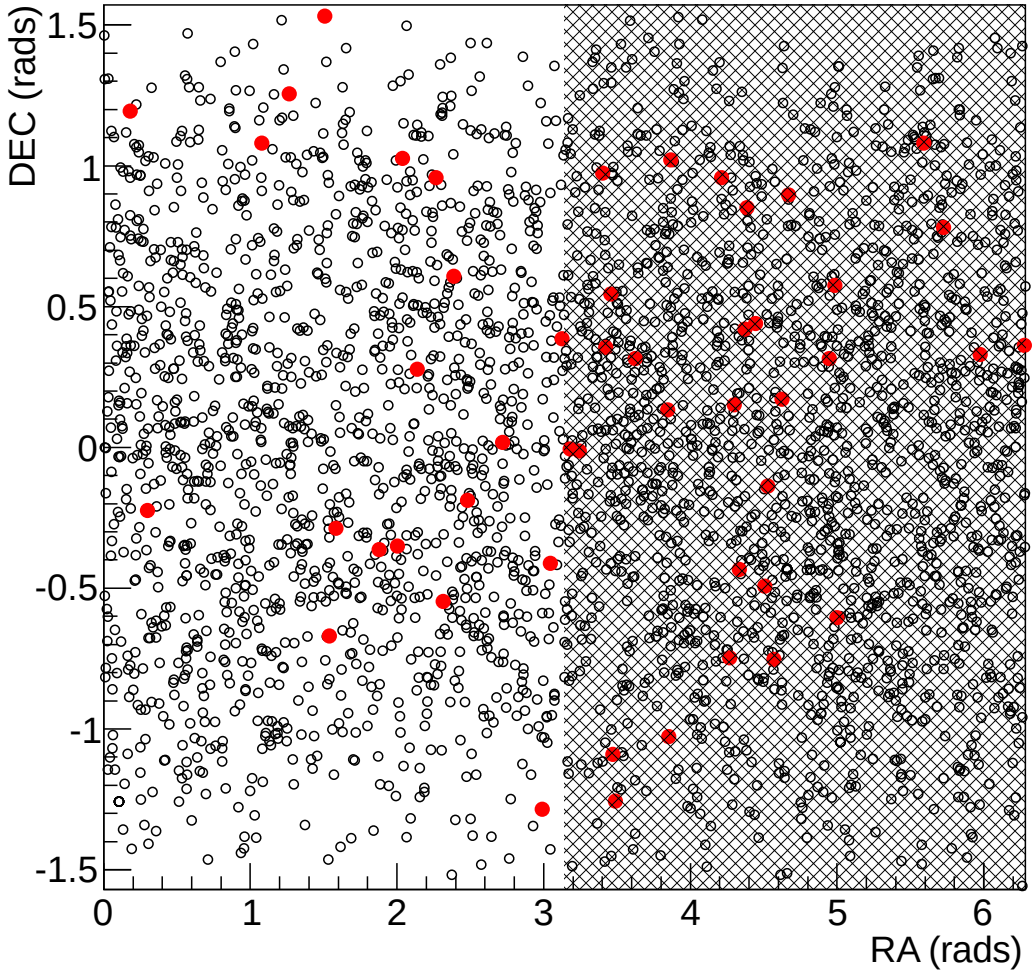

Figure 7.1 – The initial challenge signals are shown highlighted in red with the full set of 3000 signals in black. Half of the sky's parameters (the non-shaded region) are widely known to the CW group, and are used for the targeted, known signal searches. The parameters of the signals in the shaded region are not available to the CW group until follow-up on blind searches is necessary.

PowerFlux calculates the power coming from a particular region of the sky by considering

$$P[k, f_t, a_t] = \frac{\sum_{t\in \mathrm{SFT}} |a_t|^2 |z_{t,k+f_t}|^2 / w_t^4}{\sum_{t\in \mathrm{SFT}} a_t^4 / w_t^4} \tag{7.1}$$

where a_t is the series of amplitude response coefficients for sky position and polarisation, while f_t is the series of frequency bin shifts due to Doppler effects and spindown. The value $|z_{t,f_t}|^2$ is the power in the bin f_t, calculated at time t and from k which refers to the bin number of the resulting power sum [30]. The weight w_t is independent of the gravitational wave parameters and depends on the noise in each individual SFT as $w_t = 1/\sigma_t^2$ where σ_t^2 is the variance of the noise at time t [29].

PowerFlux then computes the power for 501 contiguous frequency bins at a fixed time, sky position, spindown and polarisation. The 501 values are used to compute signal-to-noise ratios, upper limits and other various statistics [29]. The size of these frequency bins is computed as $1/T_{\mathrm{coh}}$ where T_{coh} is the coherence time for the SFTs, usually 1800 seconds. Therefore the frequency bins are $1/1800\,\mathrm{Hz}$ separation [29]. The number of frequency bins is chosen because it is large enough for reasonable statistics and at the same time small enough that most of the frequency bands will avoid 1 Hz harmonics which arise as instrumental artifacts [4]. Upper limits from the weighted power sums (7.1) are calculated using the Feldman-Cousins method [37] with an assumption that the detector noise is Gaussian and there are few spikes in power [29].

Vladimir Dergachev performed an initial all-sky, blind PowerFlux run in the first frequency range of $125 < f_{\mathrm{GW}} < 175\,\mathrm{Hz}$. A spindown of 0 was assumed and there was a nominal spindown tolerance of $10^{-10}\,\mathrm{Hz\,s^{-1}}$. Of the 49 sources in this frequency range, 4 had a spindown larger than this value and could not be detected. Upper limits were calculated for all the sources and the results are shown in Figure 7.2. The upper limits are all above the actual injection and the upper limits do not seem

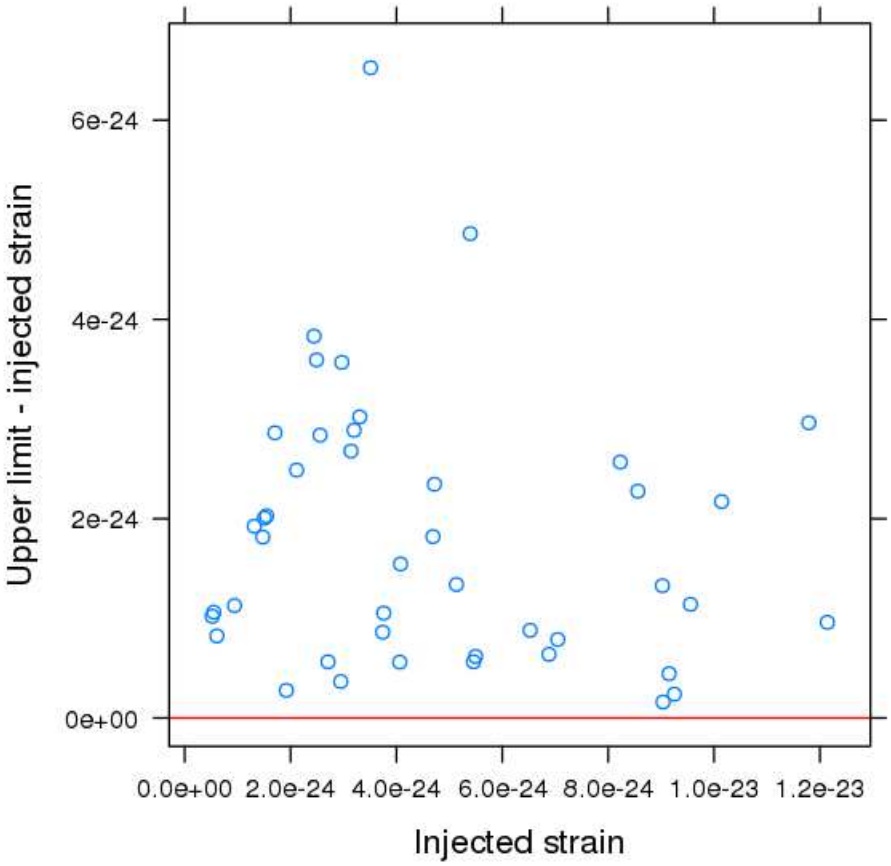

Figure 7.2 – Calculated upper limits of each injection in $125 < f_{\mathrm{GW}} < 175\,\mathrm{Hz}$ minus injected strain. Only the injections with spindown less than the nominal value are shown.

to be dependent on the strength of the injection.

Next, the signal-to-noise ratios are calculated for each injection (below the nominal spindown value of 10^{-10} Hz s^{-1}). With a list of the actual injection values, the outliers produced by PowerFlux were examined and any points within 0.6 mHz of the injected frequency were recorded. If more than one outlier was within this range, the highest SNR value was used. Out of the 49 injections, 13 signals were not detected: 9 which were missed by the code and 4 of which were higher than the nominal spindown value [31]. These SNR values are shown in Figure 7.3. There is an expected trend of decreasing SNR for weaker injected strains.

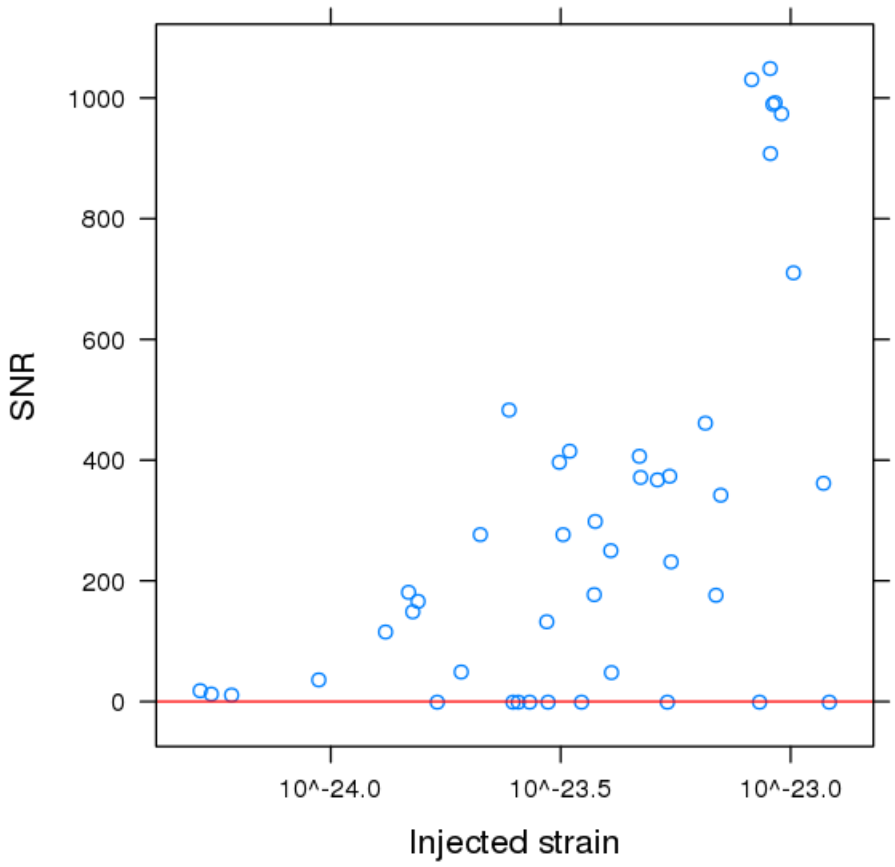

Figure 7.3 – Signal-to-noise ratios for the 49 injected signals, minus the 4 injections with too high of a spindown. Signals missed by PowerFlux are given an SNR of -1.

The 9 injected signals which were missed do not display any specific trend with

respect to the strength of the signal. Further analysis needs to be done to determine specifically why these signals were not able to be detected, despite their high strain values. The difference between the recovered sky position and the injected position is shown in Figure 7.4. The only possible trend in this data is that the stronger injected strain results in higher error from the recovered sky position.

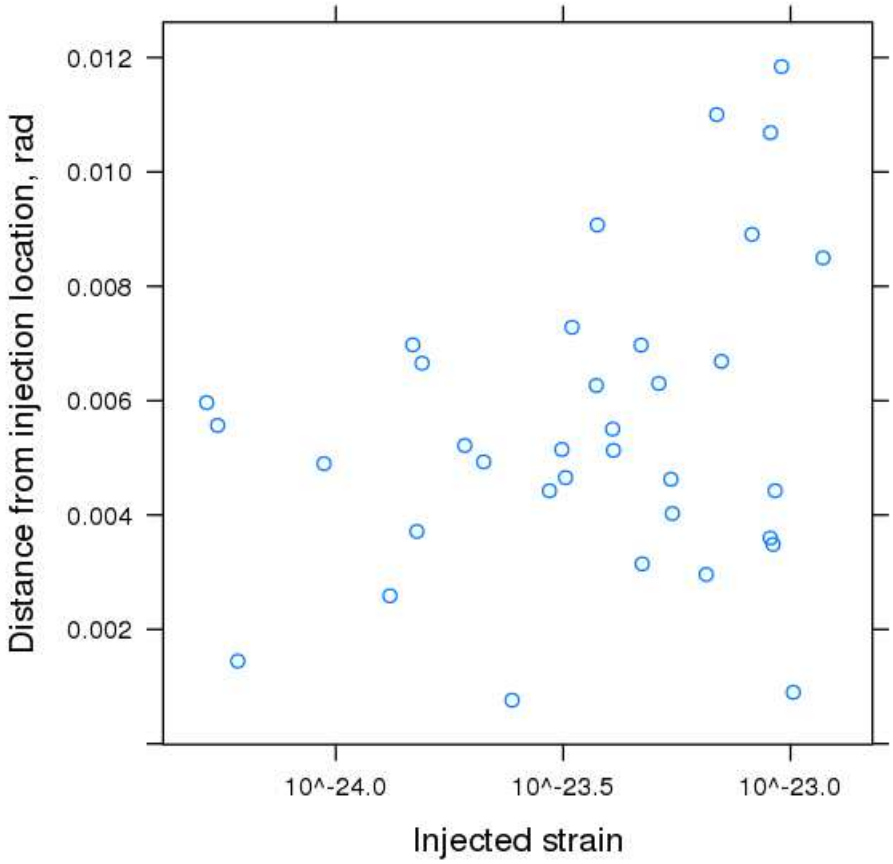

Figure 7.4 – Difference between recovered position and injected sky position for each detected signal. The missed injections are excluded from this plot.

This initial run of PowerFlux on the mock data set is an encouraging result for the full challenge of all-sky searches. It demonstrated that the injections could be detected with a blind search, but not too strong, as not all the signals were flagged as candidates.

7.1.2 Results from the Bayesian time-domain search

The CW targeted search is a time-domain Markov Chain Monte Carlo search which utilises Bayesian probability and presents results as posterior probability distributions which display a degree-of-belief in the resulting parameter values. This time-domain algorithm involves steps of heterodyning, noise and parameter estimation to extract an expected signal from the detector data. The first step involves heterodyning the data close to the expected frequency of the signal, low-pass filtered and rebinned to reduce the sample rate from 16384 Hz to 4 Hz [6].

The second step involves *fine-heterodyning* the data to take into account time-varying Doppler shift and pulsar spindown as well as instrumental calibration artifacts. This step further rebins the data to one sample per minute, during which it is assumed the data is stationary. From this, the variance and co-variance of the data in each bin can be calculated and used in the subsequent likelihood calculation [6].

The noise in the one minute data samples, $\{B_k\}$ is taken as Gaussian with respect to a parameter model, $y(t_k; \mathbf{a})$ where $\mathbf{a}$ is the parameter space vector with the gravitational wave parameters $(h_0, \cos\iota, \phi_0, \Psi)$ and t_k is the time stamp of the k-th sample. If the detector strain is described as

$$h(t) = F_+(t, \Psi)h_0\frac{1+\cos^2\iota}{2}\cos\Phi(t) + F_\times(t, \Psi)h_0\cos\iota\sin\Phi(t), \tag{7.2}$$

where $\Phi(t)$ is the phase evolution of the signal and $F_{+,\times}$ are the strain antenna patterns of the detector with plus and cross polarisation as previously described in Chapter 1. The complex heterodyne of (7.2) is given as [34],

$$y(t_k; \mathbf{a}) = \frac{1}{4}F_+(t_k; \Psi)\, h_0(1+\cos^2\iota)e^{i2\phi_0} - \frac{i}{2}F_\times(t_k; \Psi)\, h_0\cos\iota e^{i2\phi_0}. \tag{7.3}$$

The next step is to determine the prior distributions on the parameters, $\mathbf{a}$ that will be used to calculate posteriors. The parameters ϕ_0, Ψ and $\cos\iota$ all have uniform prior distributions: $\phi_0 \in [0, 2\pi]$, $\Psi \in [-\pi/4, \pi/4]$ and $\cos\iota \in [-1, 1]$. The prior for h_0 is chosen to be constant for $h_0 \geq 0$ and zero for $h_0 < 0$ [6]. The joint posterior probability distribution function (pdf) for these parameters is

$$p(\mathbf{a}|\{B_k\}) \propto p(\mathbf{a}) \exp\left[-\sum_k \frac{\Re\{B_k - y(t_k;\mathbf{a})\}^2}{2\sigma^2_{\Re\{B_k\}}}\right] \times \exp\left[-\sum_k \frac{\Im\{B_k - y(t_k;\mathbf{a})\}^2}{2\sigma^2_{\Im\{B_k\}}}\right], \tag{7.4}$$

where $\sigma^2_{\Re(\Im)\{B_k\}}$ is the variance of the real (imaginary) parts for each data sample B_k [6].

Finally, the posterior pdf (7.4) is integrated over ϕ_0, Ψ and ι to obtain a marginalised posterior for h_0,

$$p(h_0|\{B_k\}) \propto \int\int\int p(\mathbf{a}|\{B_k\})\; d\iota\, d\phi_0\, d\Psi, \tag{7.5}$$

normalised so $\int_0^\infty p(h_0|\{B_k\})\,\mathrm{d}h_0 = 1$ [6]. This targeted search places a 95% upper limit on the amplitude of the gravitational wave signal, $h_0^{95\%}$, such that

$$0.95 = \int_0^{h_0^{95\%}} p(h_0|\{B_k\})\, dh_0, \tag{7.6}$$

which defines the 95% Bayesian upper limit on a signal [6].

Colin Gill (University of Glasgow) performed the time-domain targeted search on the 19 "known" pulsars in the gravitational frequency range $125 < f_{\mathrm{GW}} < 175\,\mathrm{Hz}$ and was able to recover the parameters. The full results are shown in Table 7.1 which presents the injected parameters, $\mathcal{A}_{\mathrm{inj}}$, the recovered parameter, $\hat{\mathcal{A}}$ and the error ϵ defined as

$$\epsilon = \frac{|\mathcal{A}_{\mathrm{inj}} - \hat{\mathcal{A}}|}{\sigma}, \tag{7.7}$$

where σ is the standard deviation of the posterior distribution.

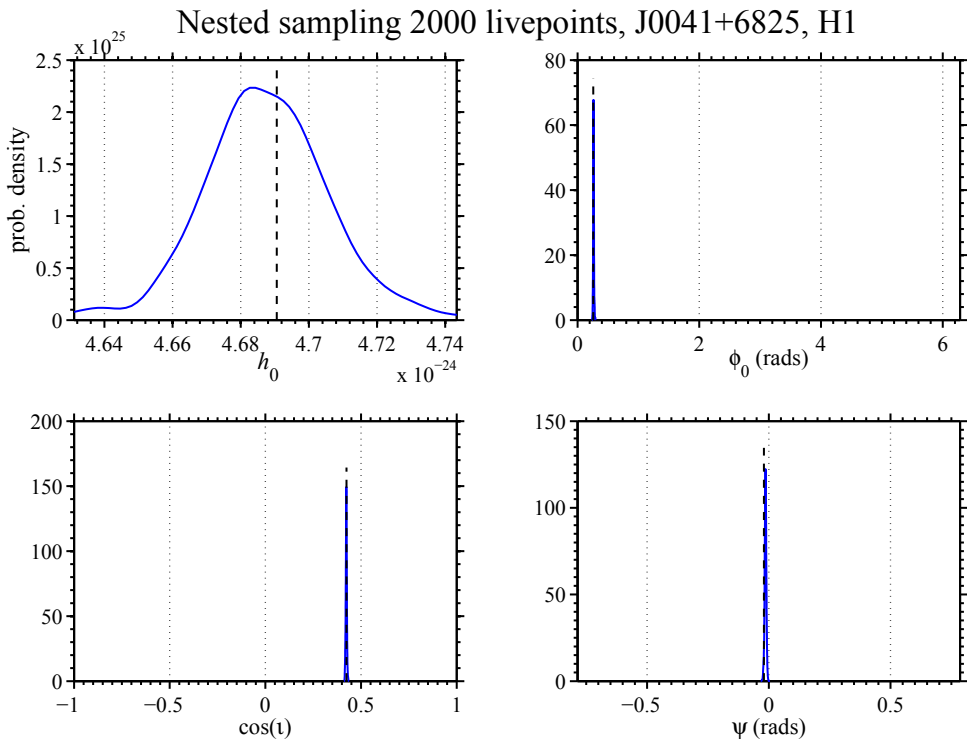

Figure 7.5 – Extraction of gravitational wave parameters for injected pulsar J0041+6825 on the H1 detector. The injected values are shown as vertical dashed lines.

Two posterior distributions for the 4 gravitational wave parameters of two injected pulsars are shown in Figures 7.5 and 7.6. These figures show the parameters ϕ_0, Ψ and $\cos\iota$ were easily recovered, with a narrow posterior distribution. The distributions for h_0 are wider but still are recovered.

	h_0	ϕ_0	Ψ	$\cos\iota$
J0041+6825 $\mathcal{A}_{\rm inj}$	4.69e-24	0.26	-0.02	0.42
$\hat{\mathcal{A}}$	4.69e-24	0.26	-0.01	0.42
ϵ	0.05	0.64	2.28	0.27
J0108-1251 $\mathcal{A}_{\rm inj}$	4.72e-24	4.34	0.33	0.45
$\hat{\mathcal{A}}$	4.67e-24	4.36	0.34	0.45
ϵ	1.60	1.85	2.38	0.61
J0407+6153 $\mathcal{A}_{\rm inj}$	3.20e-24	1.05	0.51	0.69
$\hat{\mathcal{A}}$	3.13e-24	1.06	0.49	0.71

ϵ	2.06	0.30	1.24	1.90
J0450+7153 $\mathcal{A}_{\rm inj}$	2.95e-24	4.32	-0.49	0.13
$\hat{\mathcal{A}}$	2.95e-24	4.31	-0.50	0.14
ϵ	0.16	2.00	1.68	3.53
J0545+8742 $\mathcal{A}_{\rm inj}$	3.76e-24	5.30	-0.50	0.43
$\hat{\mathcal{A}}$	3.74e-24	5.30	-0.50	0.43
ϵ	1.16	0.52	1.79	0.88
J0552-3823 $\mathcal{A}_{\rm inj}$	3.31e-24	2.39	-0.75	-0.74
$\hat{\mathcal{A}}$	3.35e-24	8.69	-0.77	-0.73
ϵ	1.29	6.98	0.03	1.18
J0602-1629 $\mathcal{A}_{\rm inj}$	7.05e-24	5.58	0.37	0.08
$\hat{\mathcal{A}}$	7.06e-24	5.58	0.36	0.08
ϵ	0.57	2.11	2.78	0.12
J0710-2048 $\mathcal{A}_{\rm inj}$	1.92e-24	0.21	-0.76	0.06
$\hat{\mathcal{A}}$	1.92e-24	6.47	-0.77	0.07
ϵ	0.27	20.43	0.05	2.11
*J0738-2002 $\mathcal{A}_{\rm inj}$	9.03e-24	2.12	0.76	-0.23
$\hat{\mathcal{A}}$	8.95e-24	2.17	0.76	-0.24
ϵ	4.87	22.74	1.15	2.64
J0746+5850 $\mathcal{A}_{\rm inj}$	5.20e-25	5.30	-0.35	-0.90
$\hat{\mathcal{A}}$	5.33e-25	6.93	0.53	-0.00
ϵ	0.29	0.74	1.94	12.32
J0810+1551 $\mathcal{A}_{\rm inj}$	5.50e-25	0.22	-0.38	0.70
$\hat{\mathcal{A}}$	6.53e-25	0.18	-0.35	0.56
ϵ	3.08	0.03	0.49	3.39
J0839+5450 $\mathcal{A}_{\rm inj}$	2.56e-24	0.10	0.41	-0.75
$\hat{\mathcal{A}}$	2.58e-24	0.26	0.50	-0.74
ϵ	0.61	2.50	2.69	0.53

*J0850-3119 $\mathcal{A}_{\rm inj}$	9.25e-24	4.65	0.14	-0.07
$\hat{\mathcal{A}}$	9.18e-24	4.63	0.14	-0.07
ϵ	4.66	13.54	2.66	2.98
J0907+3446 $\mathcal{A}_{\rm inj}$	8.23e-24	5.70	-0.05	0.38
$\hat{\mathcal{A}}$	8.22e-24	5.73	-0.06	0.37
ϵ	0.26	7.32	1.47	1.99
J0928-1046 $\mathcal{A}_{\rm inj}$	5.46e-24	4.28	0.41	0.03
$\hat{\mathcal{A}}$	5.45e-24	4.31	0.41	0.03
ϵ	0.22	9.18	3.12	3.29
*J1023+0059 $\mathcal{A}_{\rm inj}$	1.18e-23	1.40	-0.01	0.29
$\hat{\mathcal{A}}$	1.00e-23	1.39	-0.01	0.36
ϵ	2165.07	2.95	0.02	72.28
*J1125-7334 $\mathcal{A}_{\rm inj}$	9.04e-24	5.66	0.00	-0.02
$\hat{\mathcal{A}}$	8.98e-24	5.67	0.00	-0.02
ϵ	4.27	1.65	2.26	0.21
J1137-2335 $\mathcal{A}_{\rm inj}$	9.42e-25	4.37	0.22	-0.67
$\hat{\mathcal{A}}$	9.95e-25	4.40	0.24	-0.64
ϵ	1.67	0.36	0.38	1.46
J1156+2206 $\mathcal{A}_{\rm inj}$	1.70e-24	6.22	0.11	-0.89
$\hat{\mathcal{A}}$	1.73e-24	0.62	0.49	-0.00
ϵ	0.25	2.73	0.94	17.28

Table 7.1 – This table shows the recovery of the gravitational wave parameters using the targeted code on 19 pulsars in the range $125 < f_{\rm gw} < 175\,$Hz. The injected value $\mathcal{A}_{\rm inj}$, the recovered value $\hat{\mathcal{A}}$ and ϵ are all shown for each pulsar. Pulsars marked with a * are suspicious recoveries possibly due to a high amplitude (specifically J1023+0059) or being on the edge of the parameter space.

The difference between the injected and recovered gravitational wave parameters in

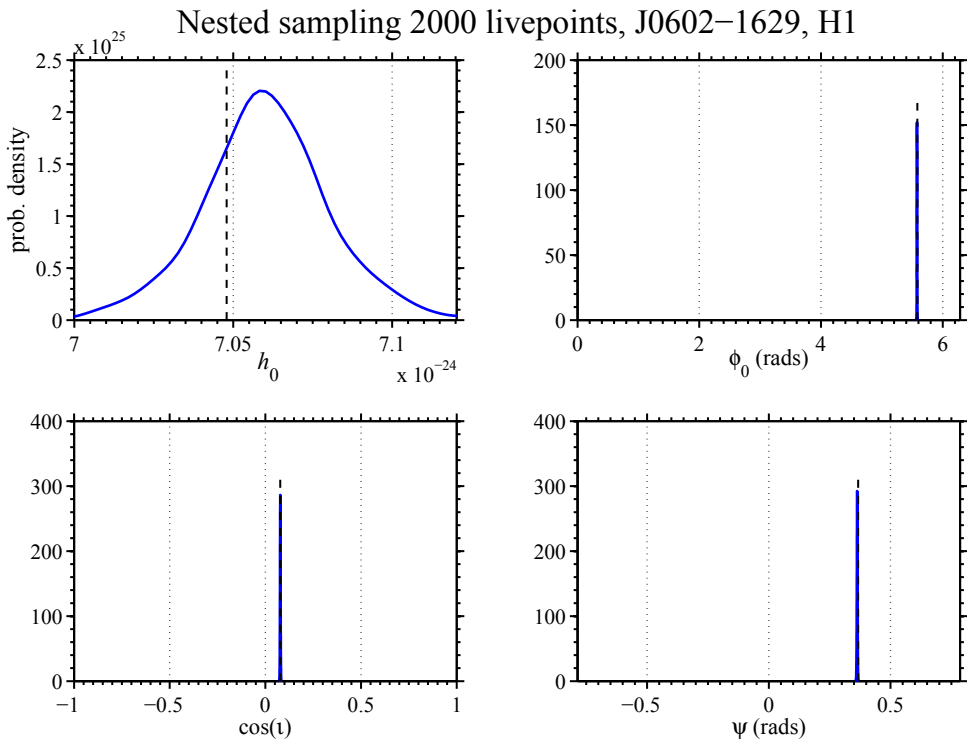

Figure 7.6 – Targeted results of gravitational wave parameters for injected pulsar J0602_1629 on the H1 detector. The injected values are shown as vertical dashed lines.

units of standard deviation are shown in Figure 7.7. While one can intuit that a higher amplitude would result in a smaller error, this effect is not seen, and it is not currently known why. Analysis of more signals may shed light on a possible trend or possible problem with the analysis code.

The primary purpose of running this targeted search on the mock data set was to make sure the signals were correctly injected and could be retrieved. Since the Glasgow targeted search works directly from time-domain raw data, there was little processing that needed to be done and results could be achieved quickly. Overall this test successfully recovered the injected signals and their parameters. This demonstrates that the mock data was generated accurately.

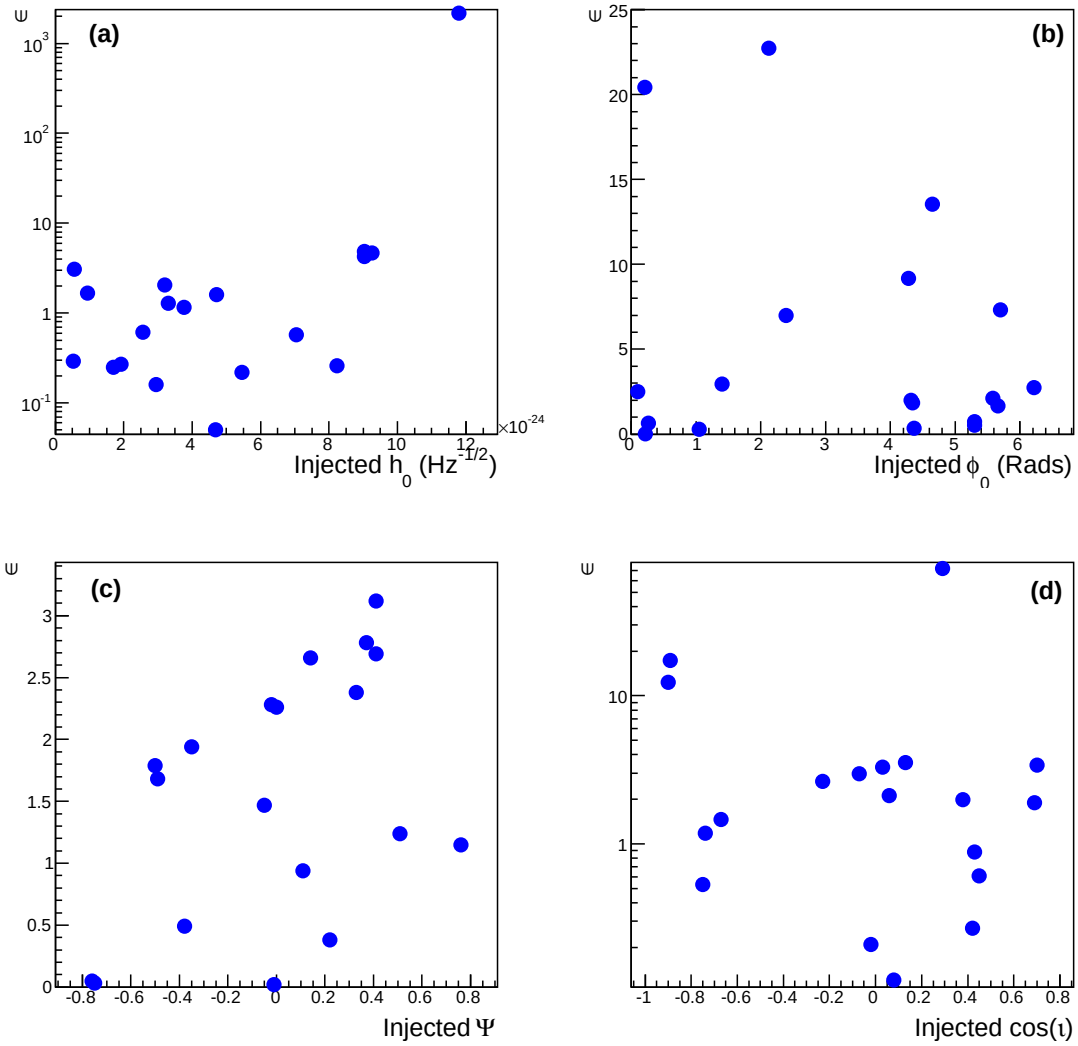

Figure 7.7 – These plots show the value ϵ, the difference between the recovered parameters and the injected values in units of standard deviation as described in Equation 7.7 for each recovered parameter. Plot (a) shows the difference in σ versus injected value for the gravitational wave strain, h_0. Plot (b) shows the difference versus injected value for the signal phase, ϕ_0. Plot (c) shows the difference from recovered to injection for polarisation angle Ψ and Plot (d) shows the difference between injected and recovered for the cosine of the inclination angle, $\cos\iota$. The discrepant recoveries discussed in Table 7.1 are still included in these plots.

7.2 Conclusion and Future Work

To date, only two of the CW search algorithms have analysed the software injected data. Over the next few years, as preparations for Advanced LIGO continue, all of the CW algorithms will perform these challenges to give us a concrete sense of relative performance. The tier system of the challenges is set up so an initial run may be done on a small, low frequency range of $125 < f_{\rm gw} < 175\,\mathrm{Hz}$ which requires smaller computing time. If the results of this challenge are not sufficient to compare algorithm performance, the next challenge, with more targets and a wider frequency range may be run. The existence of 3000 injected signals over all of S6 and across the gravitational wave detector frequency band allows any algorithm to run their own tests and analyse results. As described in Chapter 6, the data containing the software injections is available to the CW group as raw, detector frame files. This requires the group to run their entire tests from beginning to end, as they would with actual detector data.

This chapter described results from a time-domain, Bayesian targeted search on 19 pulsars in the range $125 < f_{\rm gw} < 175\,\mathrm{Hz}$ as well as results from PowerFlux, a blind, all-sky search in the same frequency range. The targeted search was able to recover all the parameters for each given pulsar with relative ease, at a high SNR. This is to be expected as the software injections were generated to have a high SNR for targeted searches, but is a check for completeness as well as a test of the targeted search's performance.

The PowerFlux blind, all-sky algorithm recovered 36 of the possible 45 signals in the same frequency range. There are 4 signals which cannot be recovered by PowerFlux as their spindown is higher than the nominal PowerFlux limit of $10^{-10}\,\mathrm{Hz\ s^{-1}}$. It is not yet clear why PowerFlux was unable to recover 9 of the signals as there was no discernible trend in strain strength which would cause them to not be detected.

The next step would be to apply the Narrow-band search described in Chapter 5

to these software injections. The Narrow-band search has been used in the past to follow-up possible detections from PowerFlux, so this same process can be applied to the software injection challenge results. There are three interesting investigations to which the narrow-band pipeline can be applied with regards to PowerFlux. PowerFlux resulted in a list of outliers in this initial frequency range, so first we would want to test if the narrow-band pipeline is able to further determine the validity of an injected signal which *has* been flagged by PowerFlux. The second test would be to run the narrow-band search on the 9 possible, but missed, signals from PowerFlux to see if the signals can be seen by a directed search, possibly shedding more light on why PowerFlux missed these signals in the first place. The third test is to run the narrow-band search on a few of the PowerFlux outliers which are known to *not* be one of the injected signals. This would give a better idea of how frequent false alarms would be with this method of a blind search followed up by a directed one. All three of these scenarios: an injected signal flagged by PowerFlux and followed up by a directed search, a signal which exists but is missed by PowerFlux and a false signal which could be flagged by PowerFlux and may or may not be falsely detected by a follow-up search are all important scenarios to consider for the Advanced Detector era, where there is a possibility of all of these occurring.

8

Conclusion

As we approach the advanced detector era, when the chances of LIGO detecting signals increase, it is important now more than ever to understand the analysis codes, both from the point of view of their efficiencies for detecting signals and for their ability to reconstruct parameters from noisy data. This thesis has considered several issues of importance for the continuous gravitational wave searches.

In Chapter 3, we explored the effect that an additional detector in the southern hemisphere would have on the sensitivity for continuous wave searches. This study concluded that there would be no significant advantage or disadvantage which is important to consider as gravitational wave networks continue to expand. While additional detectors would improve sensitivity, the location is not an issue for the targeted continuous wave algorithm.

Chapter 4 explored the issue of neutron star populations, studying extreme examples of distance and proper motion and the effect these have when generating a data set for the all-sky search Einstein@Home. After defining the values at which there begins to be an impact, we concluded that it was statistically highly unlikely such sources would exist. However, this conclusion is important for simulations and extreme testing of the algorithms.

The directed algorithm, the Narrow-band Search, was applied in Chapter 5 to data from LIGO's sixth science run (S6). Two searches were performed: one for the Crab Pulsar where no signal was definitively detected, and one for a blind hardware injection which was successfully recovered with a false alarm probability of $\sim 0\%$. The latter search was particularly useful in showing the ability for strong signals to be recovered with the correct parameters using a narrow-band, directed search with multiple templates.

Chapter 6 described the code development and production of software injected signals into S6 data. The purpose for generating these signals is to have a large data set of long-duration continuous wave signals against which various algorithms can be tested for performance in the runup to the advanced detector era. Preliminary tests from the single-template targeted time-domain search and the all-sky PowerFlux search are presented in Chapter 7.

To extend the work in this thesis, the primary objective is to explore the benefits of a hierarchical method for detecting signals from previously unknown sources. The mock data challenge presented in this thesis allows detailed comparison in performance and sensitivity whereas now they are effectively comparable. This is particularly necessary for the advanced detectors where more possible detections will require deeper understanding of the capabilities of the algorithms.

The software injections will also be used to robustly test the hierarchical method for confirming detections. That is, where a blind, all-sky search flags up a candidate, a narrow-band, directed search follows up using the uncertainties in the all-sky parameters to determine the parameters and the likelihood of detection. This method will be useful with advanced detectors at higher sensitivities which would allow the all-sky searches to detect signals from previously unknown sources and be confirmed with further algorithms. The software injections are particularly useful for testing and refining this method as there are a large amount of known sources. By deter-

mining the strengths and difficulties of such a method, the criteria for claiming a detection can be more secure and robust.

Continuous waves as presented in this thesis are promising candidates for initial direct detection of gravitational waves. As opposed to short-duration events, continuous waves are long-duration and can exist throughout detector data. As the sensitivity of the future gravitational wave detectors continue to increase by orders of magnitude, more known neutron stars (and potential gravitational wave sources) enter the range of detectability. Additionally, it is thought that only $10^{-4}\%$ of existing neutron stars have been detected through electromagnetic radiation. Gravitational wave emission presents a new opportunity for astrophysical research and the potential for detecting previously unknown continuous wave sources requires the community to refine algorithms and methods for detection to optimise their capability.

The author hopes that this work improves the understanding of the many and varied search algorithms applied to the continuous gravitational wave search problem in the LIGO Scientific Collaboration and Virgo Collaboration, and that through this improved understanding, the chances of us detecting continuous gravitational wave signals and understanding the properties of the source are improved in the upcoming advanced detector era.

Bibliography

[1] J. Abadie et al. First Search for Gravitational Waves from the Youngest Known Neutron Star. *ApJ*, 722:1504–1513, October 2010.

[2] J. Abadie et al. Beating the spin-down limit on gravitational-wave emission from the Vela Pulsar. *ApJ*, 737:93, August 2011.

[3] J. Abadie et al. Search for gravitational waves associated with the August 2006 timing glitch of the Vela pulsar. *Phys. Rev. D*, 83(4):042001, February 2011.

[4] J. Abadie et al. All-sky search for periodic gravitational waves in the full S5 LIGO data. *Phys. Rev. D*, 85(2):022001, January 2012.

[5] J. Abadie et al. Search for Gravitational Waves from Low Mass Compact Binary Coalescence in LIGO's Sixth Science Run and Virgo's Science Runs 2 and 3, 2012. LIGO Document P1100034-v18 `https://dcc.ligo.org/cgi-bin/DocDB/ShowDocument?docid=39633`.

[6] B. Abbott et al. Setting upper limits on the strength of periodic gravitational waves from PSR J1939+2134 using the first science data from the GEO 600 and LIGO detectors. *Phys. Rev. D*, 69(8):082004, April 2004.

[7] B. Abbott et al. Limits on gravitational-wave emission from selected pulsars using LIGO Data. *Phys. Rev. Lett*, 94(18):181103, May 2005.

[8] B. Abbott et al. Upper limits on gravitational wave emission from 78 radio pulsars. *Phys. Rev. D*, 76:042001, August 2007.

[9] B. Abbott et al. All-sky search for periodic gravitational waves in LIGO S4 data. *Phys. Rev. D*, 77(2):022001, January 2008.

[10] B. Abbott et al. Beating the spin-down limit on gravitational wave emission from the Crab Pulsar. *ApJ Lett*, 683:L45–L49, August 2008.

[11] B. Abbott et al. An upper limit on the stochastic gravitational-wave background of cosmological origin. *Nature*, 460:990–994, August 2009.

[12] B. Abbott et al. Einstein@Home search for periodic gravitational waves in early S5 LIGO data. *Phys. Rev. D*, 80:042003, August 2009.

[13] B. Abbott et al. Searches for gravitational waves from known pulsars with Science Run 5 LIGO data. *ApJ*, 713:671–685, April 2010.

[14] B. P. Abbott et al. LIGO: the Laser Interferometer Gravitational-Wave Observatory. *Reports of Progress in Physics*, 72(7):076901, July 2009.

[15] R. Abbott et al. Seismic isolation for advanced ligo. *Class. Quantum Grav.*, 19:1591–1597, 2002.

[16] K. A. Arnaud et al. An Overview of the Mock LISA Data Challenges. In S. M. Merkovitz and J. C. Livas, editors, *Laser Interferometer Space Antenna: 6th International LISA Symposium*, volume 873 of *American Institute of Physics Conference Series*, pages 619–624, November 2006.

[17] P. Astone, S. D'Antonio, S. Frasca, and C. Palomba. A method for detection of known sources of continuous gravitational wave signals in non-stationary data. *Class. and Quantum Grav*, 27(19):194016, October 2010.

[18] W. Baade and F. Zwicky. Remarks on super-novae and cosmic rays. *Phys. Rev*, 46:76–77, July 1934.

[19] E. E. Barnard. A small star with large proper-motion. *AJ*, 29:181–183, July 1916.

[20] E. E. Barnard. Observations of the small star with large proper-motion. *AJ*, 30:79–80, January 1917.

[21] G. Baym, C. Pethick, and D. Pines. Superfluidity in neutron stars. *Nature*, 224:673–674, November 1969.

[22] K. Belczynski et al. The effect of metallicity on the detection prospects for gravitational waves. *ApJ Lett.*, 715:L138–L141, June 2010.

[23] S. Braccini et al. Seismic vibrations mechanical filters for the gravitational waves detector virgo. *Rev. Sci. Instrum*, 67:2899–2902, 1996.

[24] P. R. Brady, T. Creighton, C. Cutler, and B. F. Schutz. Searching for periodic sources with LIGO. *Phys. Rev. D*, 57:2101–2116, February 1998.

[25] S. Chandrasekhar. The maximum mass of ideal white dwarfs. *ApJ*, 74:81, July 1931.

[26] LIGO Scientific Collaboration. Computer software lalsuite. `https://www.lsc-group.phys.uwm.edu/daswg/projects/lalsuite.html`.

[27] C. Cutler and D. I. Jones. Gravitational wave damping of neutron star wobble. *Phys. Rev. D*, 63(2):024002, January 2001.

[28] C. Cutler and B. F. Schutz. Generalized $\mathcal{F}$-statistic: Multiple detectors and multiple gravitational wave pulsars. *Phys. Rev. D*, 72(6):063006, September 2005.

[29] V. Dergachev. Description of powerflux algorithms and implementation, 2005. LIGO technical document, LIGO-T050186, available in `https://dcc.ligo.org`.

[30] V. Dergachev. Description of powerflux2 algorithms and implementation, 2011. LIGO technical document, LIGO-T1000272, available in `https://dcc.ligo.org`.

[31] V. Dergachev. Private Communication, 2012.

[32] R. DeSalvo et al. Second generation suspensions for LIGO. In J. Trân Than Vân, J. Dumarchez, S. Raynoud, C. Salomon, S. Thorsett, and J.-Y. Vinet, editors, *Gravitational Waves and Experimental Gravity*, Hanoi, 2000. World Publishers.

[33] S. V. Dhurandhar. Gravitational wave astronomy - astronomy of the 21st century. *Bulletin of the Astronomical Society of India*, 39:181–202, March 2011.

[34] R. J. Dupuis and G. Woan. Bayesian estimation of pulsar parameters from gravitational wave data. *Phys. Rev. D*, 72:102002, 2005.

[35] W.A. Edelstein, J. Hough, J.R. Pugh, and W. Martin. Limits to the measurement of displacement in an interferometric gravitational radiation detector. *J. Phys. E: Sci. Instrum*, 11(7):710–711, 1978.

[36] A. Einstein. The foundation of the general theory of relativity. *Annalen der Physik*, 49:769, 1916.

[37] G. J. Feldman and R. D. Cousins. Unified approach to the classical statistical analysis of small signals. *Phys. Rev. D*, 57:3873–3889, April 1998.

[38] J.W. Gibbs. *Elementary principles in statistical mechanics: developed with especial reference to the rational foundations of thermodynamics*. Yale bicentennial publications. C. Scribner's sons, 1902.

[39] P. Goldreich and W. H. Julian. Pulsar electrodynamics. *ApJ*, 157:869, August 1969.

[40] G. M. Harry and the LIGO Scientific Collaboration. Advanced LIGO: the next generation of gravitational wave detectors. *Class. and Quantum Grav.*, 27(8):084006, April 2010.

[41] A. Hewish et al. Observation of a rapidly pulsating radio source. *Nature*, 217:709–713, February 1968.

[42] H. Hirakawa, K. Tsubono, and M.-K. Fujimoto. Search for gravitational radiation from the Crab pulsar. *Phys. Rev. D*, 17:1919–1923, April 1978.

[43] G. Hobbs, D. R. Lorimer, A. G. Lyne, and M. Kramer. A statistical study of 233 pulsar proper motions. *MNRAS*, 360:974–992, July 2005.

[44] G. B. Hobbs, R. T. Edwards, and R. N. Manchester. TEMPO2, a new pulsar-timing package - I. An overview. *MNRAS*, 369:655–672, June 2006.

[45] J. Hough. Prospects for gravitational wave detection with laser interferometer detectors. In D.G. Blair and M.J. Buckingham, editors, *The Fifth Marcel Grossmann Meeting on recent developments in theoretical and experimental general relativity, gravitation and relativistic field theories, Part A*, pages 265–282, Singapore; River Edge, NJ, 1989. World Scientific.

[46] B. Iyer et al. LIGO-India, Proposal of the Consortium for Indian Initiative in Gravitational-wave Observations (IndIGO). `https://dcc.ligo.org/cgi-bin/DocDB/ShowDocument?docid=75988`, 2012. LIGO Document M1100296-v2.

[47] P. Jaranowski and A. Królak. *Analysis of gravitational-wave data*. Cambridge University Press, 2009.

[48] P. Jaranowski and A. Królak. Searching for gravitational waves from known pulsars using the $\mathcal{F}$- and $\mathcal{G}$-statistics. *Class. and Quantum Grav*, 27(19):194015, October 2010.

[49] P. Jaranowski, A. Królak, and B. F. Schutz. Data analysis of gravitational-wave signals from spinning neutron stars: The signal and its detection. *Phys. Rev. D*, 58(6):063001, September 1998.

[50] S. Johnston et al. Discovery of a very bright, nearby binary millisecond pulsar. *Nature*, 361:613–615, February 1993.

[51] L. Ju and D.G. Blair. Low resonant-frequency cantilever spring vibration isolator for gravitational-wave detectors. *Rev. Sci. Instrum*, 65:3482–3488, 1994.

[52] B. Knispel and B. Allen. Blandford's argument: The strongest continuous gravitational wave signal. *Phys. Rev. D*, 78:044031, Aug 2008.

[53] P.S. Laplace. *The system of the world*. Number v. 2 in The System of the World. Printed for R. Phillips, 1809.

[54] M. I. Large, A. E. Vaughan, and B. Y. Mills. A pulsar supernova association? *Nature*, 220:340, 1968.

[55] J. Levine and R. Stebbins. Upper limit on the gravitational flux reaching the Earth from the Crab Pulsar. *Phys. Rev. D*, 6:1465–1468, September 1972.

[56] A. Lyne et al. Switched Magnetospheric Regulation of Pulsar Spin-Down. *Science*, 329:408–, July 2010.

[57] T. T. Lyons, M. W. Regehr, and F. J. Raab. Shot noise in gravitational-wave detectors with fabry-perot arms. *Appl. Opt*, 39(36):6761–6770, Dec 2000.

[58] R. N. Manchester, G. B. Hobbs, A. Teoh, and M. Hobbs. The Australia Telescope National Facility Pulsar Catalogue. *AJ*, 129:1993–2006, 2005.

[59] I. Mandel, D. A. Brown, J. R. Gair, and M. C. Miller. Rates and Characteristics of Intermediate Mass Ratio Inspirals Detectable by Advanced LIGO. *ApJ*, 681:1431–1447, July 2008.

[60] H. Minkowski. Die Grundgleichungen für die elektromagnetischen Vorgänge in bewegten Körpern. *Nachrichten von der Gesellschaft der Wissenschaften zu Göttingen, Mathematisch-Physikalische Klasse*, pages 53–111, 1908.

[61] C. Misner, K. Thorne, and J. A. Wheeler. *Gravitation*. W. H. Freeman, 1973.

[62] S. Miyoki. Large scale cryogenic gravitational wave telescope. *Nucl. Phys. B (Proc. Suppl.)*, 138:439–442, 2005.

[63] LIGO/California Institute of Technology. LIGO Laboratory Home Page for Interferometer Sensitivities. `http://www.ligo.caltech.edu/~jzweizig/distribution/LSC_Data/`. (Accessed 22 February, 2012).

[64] M. Pitkin. The optimal signal-to-noise ratio for a continuous wave signal, 2011.

[65] M. Pitkin, S. Reid, S. Rowan, and J. Hough. Gravitational wave detection by interferometry (ground and space). *Living Rev. Relativity*, 14(5):10, 2011.

[66] M. Pitkin, S. Reid, S. Rowan, and J. Hough. Gravitational wave detection by interferometry (ground and space). *Living Rev. Relativity*, 14(5):11, 2011.

[67] M. Pitkin, S. Reid, S. Rowan, and J. Hough. Gravitational wave detection by interferometry (ground and space). *Living Rev. Relativity*, 14(5):13–20, 2011.

[68] R. Prix. Search for continuous gravitational waves: Metric of the multidetector F-statistic. *Phys. Rev. D*, 75(2):023004, January 2007.

[69] R. Prix. Gravitational waves from spinning neutron stars. In W. Becker, editor, *Astrophysics and Space Science Library*, volume 357 of *Astrophysics and Space Science Library*, page 651, 2009.

[70] R. Prix and B. Krishnan. Targeted search for continuous gravitational waves: Bayesian versus maximum-likelihood statistics. *Class. and Quantum Grav.*, 26(20):204013, October 2009.

[71] M. Punturo and M. et. al. Abernathy. The Einstein Telescope: a third-generation gravitational wave observatory. *Class. and Quantum Grav*, 27(19):194002, October 2010.

[72] M. Punturo and the LIGO Scientific Collaboration. The Einstein Telescope: a third-generation gravitational wave observatory. *Classical and Quantum Gravity*, 27(19):194002, October 2010.

[73] K. Riles, G. Mendell, G. Woan, and C. Palomba. Establishing detection confidence for a continuous wave signal. Technical note T0900228-v1, LIGO-Virgo Scientific Collaboration, 2009.

[74] B. S. Sathyaprakash and B. F. Schutz. Physics, astrophysics and cosmology with gravitational waves. *Living Rev. Relativity*, 12:2, 2009.

[75] Peter R. Saulson. Thermal noise in mechanical experiments. *Phys. Rev. D*, 42:2437–2445, Oct 1990.

[76] I. S. Shklovsky. On the nature of the source of X-Ray emission of SCO XR-1. *ApJ Lett*, 148:L1, April 1967.

[77] T. Suzuki. Search for continuous gravitational wave from pulsars with resonant detector. In E. Coccia, G. Pizzella, and F. Ronga, editors, *First Edoardo Amaldi Conference on Gravitational Wave Experiments*, page 115, 1995.

[78] NGO Science Working Team. NGO Revealing a hidden universe: opening a new chapter of discovery, 2011. Assessment study report `http://sci.esa.int/science-e/www/object/index.cfm?fobjectid=49839`.

[79] J. A. Tomsick et al. Is IGR J11014-6103 a Pulsar with the Highest Known Kick Velocity? *ApJ Lett*, 750:L39, May 2012.

[80] G. Ushomirsky, C. Cutler, and L. Bildsten. Deformations of accreting neutron star crusts and gravitational wave emission. *MNRAS*, 319:902–932, December 2000.

[81] A. L. Watts, B. Krishnan, L. Bildsten, and B. F. Schutz. Detecting gravitational wave emission from the known accreting neutron stars. *MNRAS*, 389:839–868,

2008.

[82] J. Weber. Detection and generation of gravitational waves. *Phys. Rev*, 117:306–313, Jan 1960.

[83] J. Weber. Evidence for discovery of gravitational radiation. *Phys. Rev Lett.*, 22:1320, 1969.

[84] J. M. Weisberg and J. H. Taylor. A new test of general relativity - Gravitational radiation and the binary pulsar PSR 1913+16. *ApJ*, 253:908, 1982.

[85] E. W. Weisstein. Hanning function. From MathWorld—A Wolfram Web Resource. `http://mathworld.wolfram.com/HanningFunction.html` Last visited on 19/5/2012.

[86] K. Wette. Estimating the sensitivity of wide-parameter-space searches for gravitational-wave pulsars. *Phys. Rev. D*, 85(4):042003, February 2012.

[87] K. Wette et al. Searching for gravitational waves from Cassiopeia A with LIGO. *Class. and Quantum Grav*, 25(23):235011, December 2008.

[88] N. L. Zakamska and S. Tremaine. Constraints on the Acceleration of the Solar System from High-Precision Timing. *AJ*, 130:1939–1950, October 2005.